FEDERAL UNIVERSITY OF SÃO CARLOS
CENTER FOR EXACT SCIENCES AND TECHNOLOGY
GRADUATE PROGRAM IN MATERIALS SCIENCE AND ENGINEERING

DESIGN OF Ti-Nb-Cr ALLOYS FOR HYDROGEN STORAGE: EXPLORING HYDRIDE DESTABILIZATION THROUGH Nb/Ti RATIO ADJUSTMENT

Gabriela Chimello Mayer Dias

São Carlos-SP
2024

FEDERAL UNIVERSITY OF SÃO CARLOS
CENTER FOR EXACT SCIENCES AND TECHNOLOGY
GRADUATE PROGRAM IN MATERIALS SCIENCE AND ENGINEERING

DESIGN OF Ti-Nb-Cr ALLOYS FOR HYDROGEN STORAGE: EXPLORING HYDRIDE DESTABILIZATION THROUGH Nb/Ti RATIO ADJUSTMENT

Gabriela Chimello Mayer Dias

Dissertation presented to Graduate Program in Materials Science and Engineering as partial requirement to obtain the MASTER DEGREE IN MATERIALS SCIENCE AND ENGINEERING.

Supervisor: Prof. Dr. Guilherme Zepon
Funding agencies: FAPESP (Process: 2022/06719-6), BEPE/FAPESP (Process: 2023/02732-0), and CAPES (Process: 88887.704446/2022-00).

São Carlos-SP
2024

DEDICATION

To my parents, Juliana and Fernando, and my sister Maria Fernanda, with all my love and gratitude.

CANDIDATE'S VITAE

BSc. in Materials Engineering at the Federal University of São Carlos.

UNIVERSIDADE FEDERAL DE SÃO CARLOS

Centro de Ciências Exatas e de Tecnologia
Programa de Pós-Graduação em Ciência e Engenharia de Materiais

Folha de Aprovação

Defesa de Dissertação de Mestrado da candidata Gabriela Chimello Mayer Dias, realizada em 23/07/2024.

Comissão Julgadora:

Prof. Dr. Guilherme Zepon (UFSCar)

Prof. Dr. Walter José Botta Filho (UFSCar)

Prof. Dr. Ricardo Floriano (UNICAMP)

O Relatório de Defesa assinado pelos membros da Comissão Julgadora encontra-se arquivado junto ao Programa de Pós-Graduação em Ciência e Engenharia de Materiais.

ACKNOWLEDGMENT

I am deeply grateful to my parents and my sister for their unwavering love and support. Words cannot express how crucial they have been in helping me reach this point, providing the strength and inspiration to pursue my dreams.

I would like to express my gratitude to my supervisor, Prof. Dr. Guilherme Zepon, for his essential support and constant dedication throughout this work. He has guided me through my fantastic journey in research from the very beginning and has undoubtedly been an inspiration to me.

I would like to thank Dr. Michael Felderhoff and the entire H_2 group at the Max-Planck-Institut für Kohlenforschung for the incredible 6 months I spent there. The experiences gained during this time have significantly enriched my work and created unforgettable memories.

Special thanks to the entire LH_2M group for their amazing companionship and assistance during this time. In particular, I want to express my deepest gratitude to Bruno for his invaluable support and love, which have made this journey much easier and filled it with warmth and happiness.

I am grateful to the Fundação de Amparo à Pesquisa do Estado de São Paulo (FAPESP) (process n° 2022/06719-6, and BEPE process n° 2023/02732-0) and to CAPES - Coordenação de Aperfeiçoamento de Pessoal de Nível Superior (process n° 88887.704446/2022-00), for their financial support.

This study was financed in part by the Coordenação de Aperfeiçoamento de Pessoal de Nível Superior – Brasil (CAPES) - Finance Code 001.

ABSTRACT

Hydrogen is emerging as a promising alternative to fossil fuels amidst concerns over depleting reserves and environmental impacts. However, efficient hydrogen storage remains a significant challenge for widespread application. Solid-state storage, especially using metal hydrides, presents a promising solution for efficient storage at moderate pressure conditions. Alloys with a body-centered cubic (BCC) structure, such as those in the Ti-V-Cr and Ti-V-Nb-Cr systems, have shown promising properties. Notably, studies specifically on hydrogen storage in Ti-Nb-Cr ternary system alloys are scarce, with results emphasizing high hydride stability. To enhance the efficiency of MH-based hydrogen storage systems, achieving hydrogen desorption at low temperatures is crucial. In this context, this study investigates the hydride destabilization in the Ti-Nb-Cr system by designing alloys with a reduced concentration of the stronger hydride-forming element, Ti, and an increased fraction of the weaker hydride-forming element, Nb. To favor a predominant body-centered cubic (BCC) phase, Cr content was maintained below 35 at.%. The impact of these compositional adjustments on key properties for solid-state hydrogen storage was thoroughly examined. Trends in the plateau pressures of the Pressure-Composition-Temperature (PCT) diagrams were predicted using a thermodynamic model. Four compositions were studied: $Ti_{1.0}Nb_{1.0}Cr_{1.0,}$ $Ti_{0.8}Nb_{1.4}Cr_{1.0}$, $Ti_{0.6}Nb_{1.8}Cr_{1.0}$, and $Ti_{0.4}Nb_{2.2}Cr_{1.0}$. These alloys were synthesized via arc melting and predominantly exhibited a BCC phase with a fraction of C15 Laves phase. All alloys showed rapid absorption kinetics and attained maximum hydrogen storage capacities of 2.79 wt.%, 2.30 wt.%, 2.23 wt.%, and 2.09 wt.%, as the Nb/Ti ratio increased. After 10 cycles, capacities decreased by 0.20 wt.%, 0.16 wt.%, 0.17 wt.%, and 0.26 wt.%, respectively. PCT diagrams indicated that increasing the Nb/Ti ratio resulted in higher plateau pressures, nearly reaching 1 bar in absorption for the $Ti_{0.4}Nb_{2.2}Cr_{1.0}$ alloy. Thermal analysis revealed that the enthalpy of desorption became lower with increasing the Nb/Ti ratio, indicating hydride destabilization.

Keywords: Hydrogen Storage; Metal Hydrides; Ti-Nb-Cr.

RESUMO

DESIGN DE LIGAS TI-Nb-Cr PARA ARMAZENAGEM DE HIDROGÊNIO: EXPLORANDO A DESESTABILIZAÇÃO DE HIDRETOS ATRAVÉS DO AJUSTE DA RAZÃO Nb/Ti.

O hidrogênio surge como uma alternativa promissora aos combustíveis fósseis, diante das preocupações com reservas finitas e impactos ambientais. No entanto, um dos desafios cruciais para sua aplicação é o armazenamento eficiente. O uso de hidretos metálicos para armazenagem de hidrogênio no estado sólido oferece uma solução promissora para o armazenamento eficiente em baixas pressões. Ligas com estrutura cúbica de corpo centrado (CCC), como nos sistemas Ti-V-Cr e Ti-V-Nb-Cr, têm mostrado propriedades promissoras. Entretanto, estudos sobre armazenamento de hidrogênio em ligas do sistema ternário Ti-Nb-Cr são escassos, com resultados que evidenciam uma alta estabilidade dos hidretos. Neste contexto, este estudo investigou a desestabilização de hidretos do sistema Ti-Nb-Cr por meio do design de ligas com menores concentrações do elemento formador de hidreto mais estável, Ti, e aumento da fração do elemento formador de hidreto menos estável, Nb. Para favorecer uma fase predominantemente CCC, o teor de Cr foi mantido abaixo de 35 %at. O impacto desses ajustes de composição nas propriedades-chave para armazenamento de hidrogênio em estado sólido foi examinado detalhadamente. Tendências nas pressões do platô nos diagramas Pressão-Composição-Temperatura (PCT) foram previstas por meio de um modelo termodinâmico. Quatro composições foram estudadas: $Ti_{1.0}Nb_{1.0}Cr_{1.0}$, $Ti_{0.8}Nb_{1.4}Cr_{1.0}$, $Ti_{0.6}Nb_{1.8}Cr_{1.0}$ e $Ti_{0.4}Nb_{2.2}Cr_{1.0}$, que exibiram fase CCC com uma fração de fase de Laves C15. Todas as ligas apresentaram cinética de absorção rápida e atingiram capacidades máximas de armazenamento de hidrogênio de 2,79 %p, 2,30 %p, 2,23 %p e 2,09 %p, respectivamente, à medida que a razão Nb/Ti foi aumentada. Diagramas PCT indicaram que o aumento da razão Nb/Ti resultou em maiores pressões de platô de absorção. Análises térmicas revelaram que a entalpia de dessorção diminuiu com o aumento da razão Nb/Ti, indicando a desestabilização de hidreto.

Palavras-chave: armazenagem de hidrogênio; hidretos metálicos; TiNbCr.

PUBLICATIONS

G. C. M. Dias, B. H. Silva, A. S. Martins, M. Felderhoff, W. J. Botta, G. Zepon, Hydride destabilization in the Ti-Nb-Cr system through Nb/Ti ratio adjustment, ACS Applied Energy Materials (2024), https://doi.org/10.1021/acsaem.4c01167.

INDEX

TABLE INDEX

FIGURE INDEX

1 INTRODUCTION

Approximately 90% of global energy consumption is currently obtained via fossil fuels[1]. However, their reserves are finite, and their use significantly contributes to environmental issues due to the emission of greenhouse gases. Given this scenario, hydrogen arises as a viable alternative to replace fossil fuel, since it has a gravimetric energy density three times higher than gasoline, and its oxidation generates only water as a byproduct. Unlike fossil fuels, hydrogen can be produced through various routes using different energy sources. Emphasis is placed on those methods that ensure zero or low-carbon emissions, such as water electrolysis powered by renewable energy sources. Brazil stands out as one of the best-positioned countries for large-scale production of low-carbon emission hydrogen. Multiple studies are currently underway to achieve cost parity between low-carbon emission hydrogen and other production methods based on fossil fuels [2].

Taking this approach as an example, a hydrogen cycle can be illustrated (see Figure 1.1). A renewable energy source, such as solar energy, is converted into electricity, which is then used for water electrolysis. In this process, oxygen is released, and hydrogen is obtained to be stored, transported, and distributed. When hydrogen is combusted, it releases heat and work, and water is returned to the atmosphere, thus closing the cycle [3].

However, hydrogen storage is a major challenge that must be overcome to enable its safe and efficient utilization. Due to its low volumetric, it is essential to increase hydrogen density for effective storage. In the gaseous state, high-pressure cylinders are required, which raises safety concerns. Meanwhile, in liquid state, cryogenic tanks at -252.88 °C and 1 atm of pressure are necessary, consuming a large amount of energy for this process. Finally, in the solid state, the aim is to increase the hydrogen density by reducing repulsion between hydrogen molecules, binding them to a material. Materials such as Metal-Organic Frameworks (MOFs) and nanostructured carbon can store hydrogen through physisorption, relying on weak Van der Waals forces. Conversely, storage via

chemisorption involves metal hydrides, where the H_2 molecules dissociate and H atoms diffuse through the metal lattice, finally occupying interstitial sites [4–7].

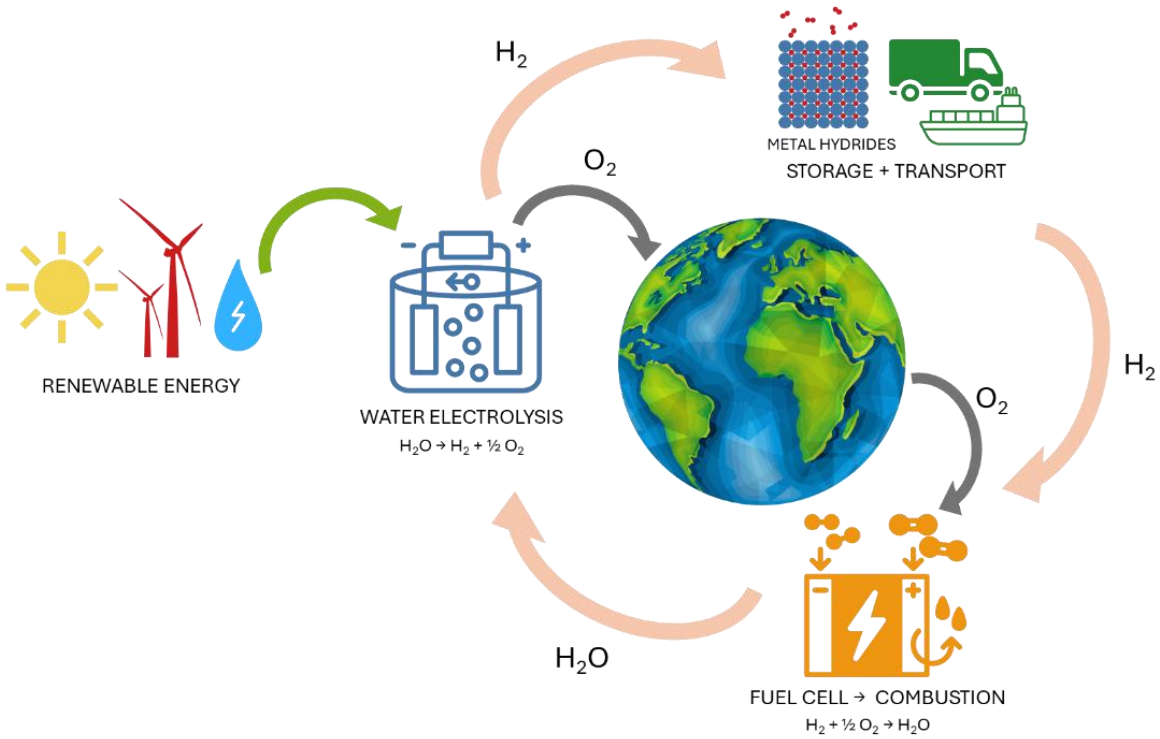

Figure 1.1: Schematic representation of the hydrogen cycle. Adapted from [3].

Various types of metal hydrides are being studied, including variants based on Mg, body-centered cubic (BCC) solid solutions, and intermetallic hydrides within the AB, A_2B, AB_2, and AB_5 families. Examples include TiFe, Mg_2Ni, ZrV_2, and $LaNi_5$, where A and B represent hydride-forming and non-hydride-forming elements, respectively [4,5]. BCC alloys are particularly promising due to their typically superior gravimetric storage capacity compared to intermetallic compounds. Numerous studies are focused on developing compositions of BCC alloys that offer increasingly enhanced hydrogen storage properties. Traditionally, these compositions lean on first-series transition metals like titanium, chromium, manganese, and iron to exploit their lower molar weight, achieving increased gravimetric capacity [8]. For example, the $Ti_{40}V_{32}Cr_{10}Mn_{18}$ alloy presents a high maximum storage capacity of 3.98 wt.% [9].

Incorporating second and third-series transition metals, like niobium, zirconium, and molybdenum, has emerged as a beneficial strategy for improving

the hydrogen storage properties of BCC solid solutions [8]. Silva et al. [10] conducted a comprehensive study into the multicomponent Ti-V-Nb-Cr system. Through composition adjustments, they developed the $Ti_{11}V_{30}Nb_{28}Cr_{31}$ alloy, showcasing a total hydrogen storage capacity of 2.45 wt.%. This alloy demonstrates reversible hydrogen absorption and desorption of approximately 1.7 wt.% at room temperature and moderate pressure.

While extensive research has been conducted on both the Ti-V-Cr and Ti-V-Nb-Cr systems [11–25], studies focusing on the Ti-Nb-Cr system are notably scarce. Sakaki et al. [26] explored the single-phase BCC $Nb_x(Ti_{0.7}Cr_{0.3})_{1-x}$ (x = 0.3, 0.4, 0.5, 0.6) alloys. The Pressure-Composition-Isotherm (PCI) curves at 150 °C revealed a plateau pressure in absorption of approximately 2 bar for the $Ti_{28}Nb_{60}Cr_{12}$ alloy. This finding implies that, at room temperature, the plateau pressure would significantly decrease below the atmospheric pressure. Such characteristic indicates high hydride stability, necessitating elevated temperatures for hydrogen desorption, which may not be ideal for numerous applications. For instance, the U.S. Department of Energy (DOE) has established ultimate targets for onboard hydrogen storage in light-duty fuel cell vehicles, specifying that delivery temperature should remain below 85 °C [27].

To increase the plateau pressure, adjustments in the composition of the Ti-Nb-Cr can be made. The stability of a hydride is dictated by its enthalpy of formation. The elements can be classified into hydride-forming (A), with negative values of the enthalpy of formation, and non-hydride-forming (B), with positive values of enthalpy of formation. The strategic blending of different elements in diverse compositions enables the fine-tuning of hydride stability. Less negative enthalpies of formation yield less stable hydrides, thereby leading to higher plateau pressures. Following this principle, increasing the content of Cr, a non-hydride-forming element, while reducing the Ti or Nb content, both hydride-forming elements, can elevate plateau pressures [27]. However, recent studies of Ti-V-Nb-Cr systems indicate that Cr contents exceeding 35 at.%. result in the formation of the C15-type Laves phase, which does not contribute to the alloy's hydrogen storage capacity [14]. Ternary diagrams of the Ti-Nb-Cr system suggest that a predominant BCC phase can be obtained only when the Cr content does

not surpass approximately 35 at.%. Consequently, in this work, the strategy to destabilize the hydrides involved reducing the concentration of the stronger hydride-forming element, Ti (ΔH_f^0= -67 kJ/mol of H [28]), while elevating the fraction of the weaker hydride-forming element, Nb (ΔH_f^0= -20 kJ/mol of H [29]), maintaining a Cr content below 35 at.%.

In summary, there's a significant gap in the understanding of alloys within the Ti-Nb-Cr system. Moreover, given Brazil's abundant reserves of Nb, exploring Nb-rich alloys is a strategic choice. Considering the properties reported by Sakaki et al. [26], this system holds potential for optimization through compositional adjustments, with a notable emphasis on decreasing its stability. These factors motivated the choice of the Ti-Nb-Cr system as the focus of study for this master's project, intending to conduct a comprehensive and in-depth investigation of its hydrogen storage properties and the destabilization of the hydrides through compositional tuning. In this work, the starting point was the equiatomic $Ti_{1.0}Nb_{1.0}Cr_{1.0}$ alloy and three other compositions were designed, with increasing Nb and decreasing Ti content in relation to Cr: $Ti_{0.8}Nb_{1.4}Cr_{1.0}$, $Ti_{0.6}Nb_{1.8}Cr_{1.0}$, and $Ti_{0.4}Nb_{2.2}Cr_{1.0}$.

2 OBJECTIVES

This dissertation aims to investigate the hydrogen storage properties of the Ti-Nb-Cr system and the destabilization of hydrides within this system by increasing the Nb/Ti ratio. The compositions selected for study are: $Ti_{1.0}Nb_{1.0}Cr_{1.0,}$ $Ti_{0.8}Nb_{1.4}Cr_{1.0}$, $Ti_{0.6}Nb_{1.8}Cr_{1.0}$, and $Ti_{0.4}Nb_{2.2}Cr_{1.0}$. These variations in composition will enable an understanding of how changes in the Nb/Ti ratio affect phase formation, microstructure, and hydrogen storage properties.

3 LITERATURE REVIEW

3.1 Fundamentals of Metal Hydride Formation

Metal hydrides are formed by the spontaneous, reversible, and exothermic reaction between the metal (M) and H_2, according to equation 1, under favorable conditions of pressure and temperature.

$$M_{(s)} + \frac{x}{2} H_{2\,(g)} \leftrightarrow MH_{x\,(s)} + Q \quad (1)$$

Figure 3.1 illustrates the steps involved in metal hydride formation. Upon the formation of interstitial hydrides, the initial step involves the interaction between the hydrogen molecules and the metal surfaces through Van der Waals forces, leading to the physisorbed state. Subsequently, the hydrogen molecules dissociate, transitioning to a chemisorbed state on the metal surface, where hydrogen-metal bonds form. Then, hydrogen atoms diffuse into the bulk and randomly occupy interstitial sites within the structure, thereby forming an M-H solid solution (α-phase) [3]. The α-phase can absorb a maximum quantity of hydrogen, proportional to the hydrogen pressure, as described by Sievert's law [25] (Equation 2):

$$c\left(\frac{H}{M}\right) = K\sqrt{pH_2} \quad (2)$$

where c(H/M) is the solubility limit, K is a temperature-dependent constant, and pH_2 is the hydrogen pressure. With an increase in hydrogen pressure, the solubility limit is reached, marking the onset of hydride formation (β-phase).

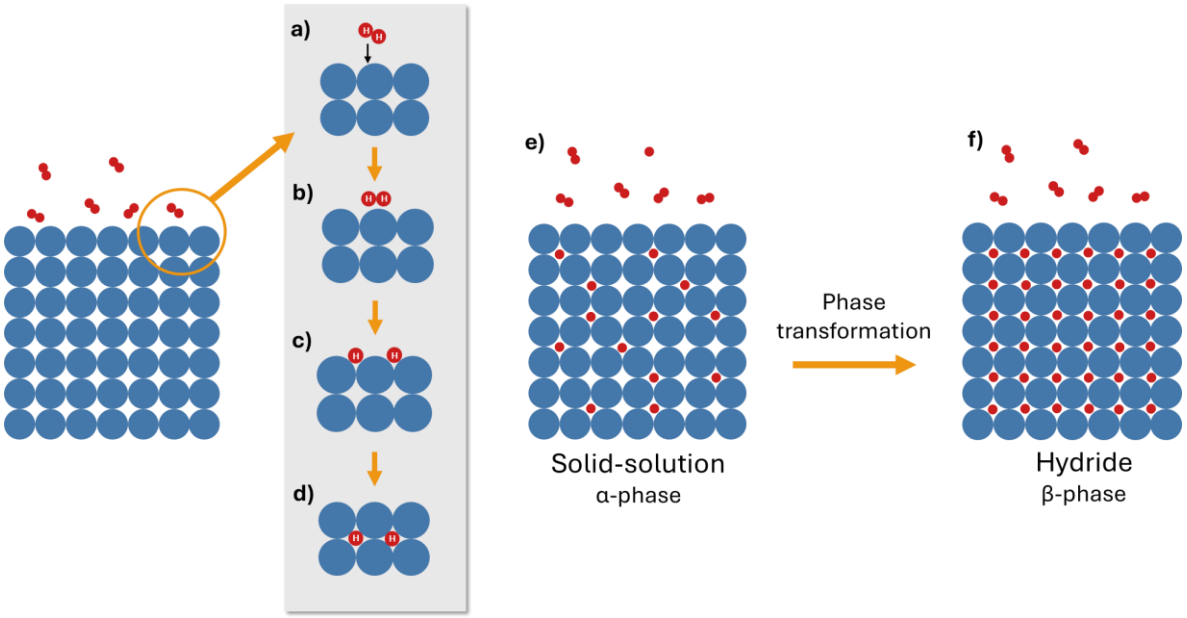

Figure 3.1: Illustration of the steps in metal hydride formation: a) interaction between hydrogen molecules and the metal surfaces via Van der Waals forces, b) adsorption of hydrogen molecules on the metal surface, c) dissociation of hydrogen molecules, d) absorption and diffusion of hydrogen atoms within the metal lattice, e) formation of a solid solution (α-phase), and f) formation of a hydride (β-phase).

3.2 Thermodynamics of Metal Hydride Formation

It is important to distinguish the different types of equilibrium that can occur in metal-hydrogen systems. Complete equilibrium (CE) is achieved when the chemical potential of all elements is the same across all co-existing phases. This state is typically reached at high temperatures, where the mobility of metal atoms is sufficiently high. However, because metal hydrides are usually employed at low or moderate temperatures, para-equilibrium (PE) occurs instead: the metal atoms can be considered “frozen”, meaning that there is no chemical partitioning of the metal elements during the hydride formation, and the equilibrium is reached due to the mobility of hydrogen atoms, when the hydrogen chemical potential becomes the same in the co-existing phases [30,31].

The amount of hydrogen in a phase is given by:

$$c_H = \frac{n_H}{n_M} \tag{3}$$

where n_H and n_M represent de number of moles of hydrogen and metal atoms in a phase, respectively. Under PE conditions, the chemical compositions of the phases in terms of metal atoms are fixed, and the equilibrium is achieved through variations in the hydrogen concentration (c_H).

The Gibbs free energy (ΔG_m) of the phases depends on c_H. Specifically, $\Delta G_m(c_H)$ represents the difference in Gibbs free energy between a phase with a composition c_H and a reference state.

$$\Delta G_m(c_H) = \Delta H_m(c_H) - T\Delta S_m(c_H) \quad (4)$$

The chemical potential of hydrogen in the α- and β-phases are given by equations 5 and 6, respectively. Additionally, the chemical potential of H_2 gas per mol of hydrogen is provided by equation 7.

$$\mu_H^{\alpha}(c_H) = \frac{d\Delta G_m^{\alpha}(c_H)}{dc_H} \quad (5)$$

$$\mu_H^{\beta}(c_H) = \frac{d\Delta G_m^{\beta}(c_H)}{dc_H} \quad (6)$$

$$\mu_H^{H_2} = \frac{1}{2} RTIn\frac{P_{H_2}}{P^0} \quad (7)$$

Due to the PE condition, the chemical potentials of metal atoms in α- and β-phases are also functions of c_H. These are given by equations 8 and 9, respectively.

$$\mu_M^{\alpha}(c_H) = \Delta G_m^{\alpha}(c_H) - c_H\mu_H^{\alpha}(c_H) \quad (8)$$

$$\mu_M^{\beta}(c_H) = \Delta G_m^{\beta}(c_H) - c_H\mu_H^{\beta}(c_H) \quad (9)$$

Phases are in equilibrium when their chemical potentials of hydrogen and metal atoms are the same in each phase: $\mu_H^{H_2} = \mu_H^{\alpha}(c_H) = \mu_H^{\beta}(c_H)$ and $\mu_M^{\alpha}(c_H) = \mu_M^{\beta}(c_H)$. Since $\mu_H^{H_2}$ depends on the hydrogen pressure (P_{H_2}), the equilibrium of the phases will depend on P_{H_2}, with a specific pressure value at which α, β, and H_2 coexist in equilibrium.

Building upon this premise, the Pressure-Composition-Isotherm (PCI) diagram is illustrated in Figure 3.2. This diagram demonstrates the equilibrium pressure of hydrogen as a function of its concentration in the metal at a specific temperature. While α, β, and H_2 coexist, a pressure plateau appears on the isotherms. When the α-phase is entirely transformed into the β-phase, the

equilibrium pressure increases abruptly with the hydrogen concentration. Below the plateau pressure (P_{plat}), only the α-phase remains in equilibrium with the H_2 gas, while above the plateau, only the β-phase is in equilibrium with the H_2 gas.

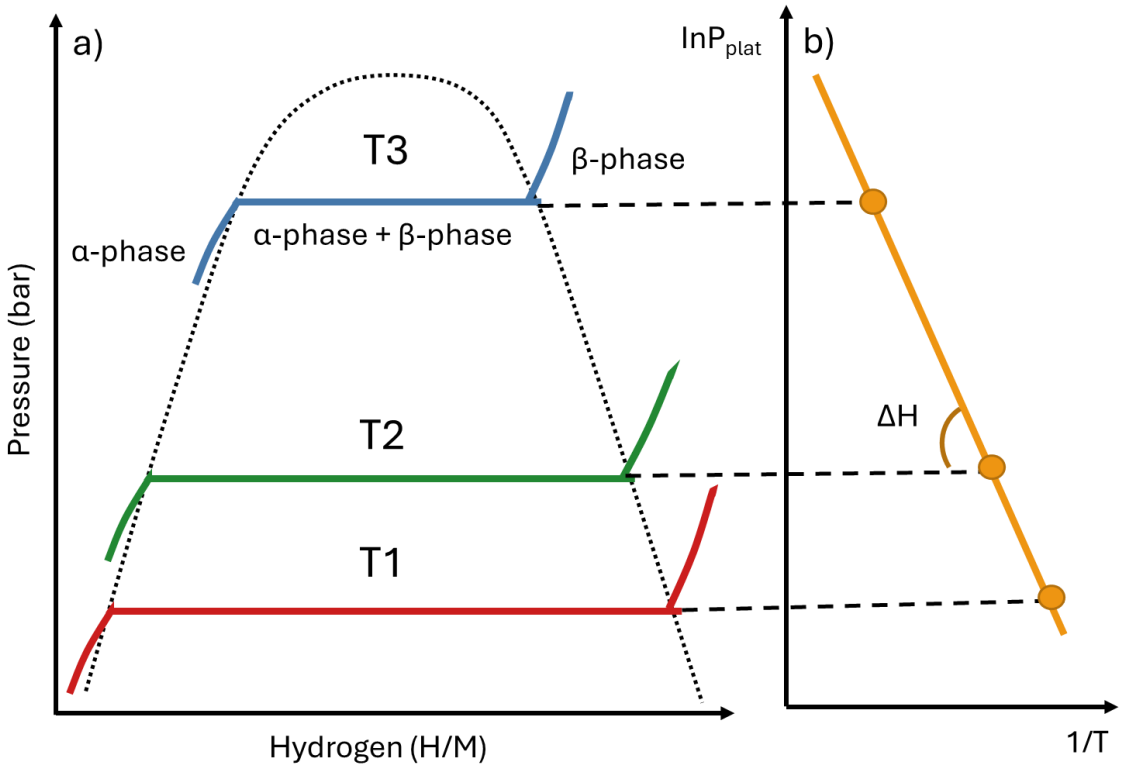

Figure 3.2: a) PCT (Pressure-Composition-Temperature) diagram and b) Van't Hoff diagram for a hypothetical metal-hydrogen system.

Figure 3.3 illustrates the equilibrium condition represented by the common tangent of the $\Delta G_m(c_H)$ curves for the α- and β-phases, with compositions $c^{\alpha}_{H\ plat}$ and $c^{\beta}_{H\ plat}$, respectively. During the hydride formation, the α- and β-phases will coexist in equilibrium and the H_2 will be at the plateau pressure P_{plat}, which is described by equation 10 as a function of temperature.

$$\frac{1}{2}RT\left(\frac{P_{plat}}{P^0}\right) = \frac{\Delta G_m^{\beta}\left(c^{\beta}_{H\ plat}\right) - \Delta G_m^{\alpha}\left(c^{\alpha}_{H\ plat}\right)}{c^{\beta}_{H\ plat} - c^{\alpha}_{H\ plat}} \qquad (10)$$

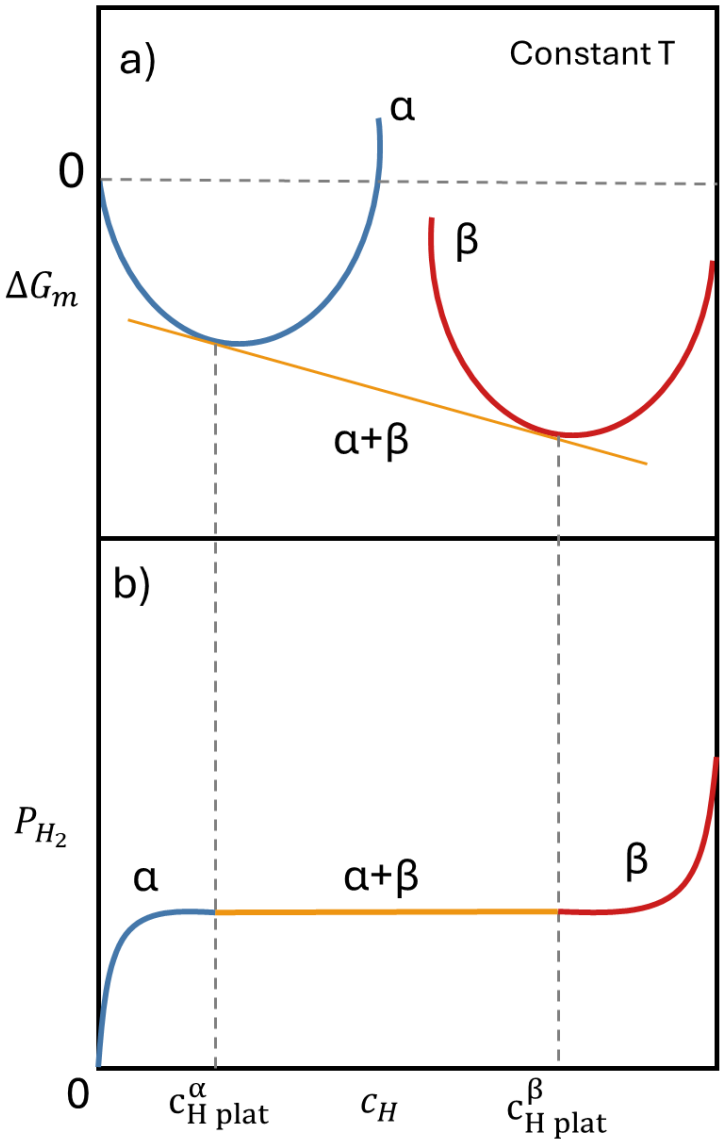

Figure 3.3: a) Gibbs Free Energy of α- and β-phases as a function of c_H for a hypothetical metal hydride system for a given temperature under PE condition, and b) the corresponding PCI diagram. Adapted from [30].

The Van't Hoff equation (equation 11) relates the equilibrium plateau pressure (P_{plat}) to the enthalpy and entropy changes in the transition from the α-phase to β-phase [5].

$$\frac{1}{2}\ln(P_{plat}) = \frac{\Delta H_{plat}}{RT} - \frac{\Delta S_{plat}}{R} \tag{11}$$

From the pressures of the measured plateaus at different temperatures (PCT diagram), it is possible to plot a graph of the natural logarithm of P_{plat} as a function of the inverse of the absolute temperature (1/T). This produces a straight line, where the slope represents the plateau enthalpy divided by the universal gas constant (R). This graphical representation, known as the Van't Hoff diagram, is schematized in Figure 3.2 (b). Additionally, Van't Hoff plots of selected hydrides and composite materials are presented in Figure 3.4. The blue shaded area represents the optimal operation conditions for temperature and pressure. It is evident that different metal hydrides can exhibit a wide range of thermodynamic properties. Notably, several binary hydrides, such as TiH_2 and MgH_2, show significantly greater stability than the ideal conditions.

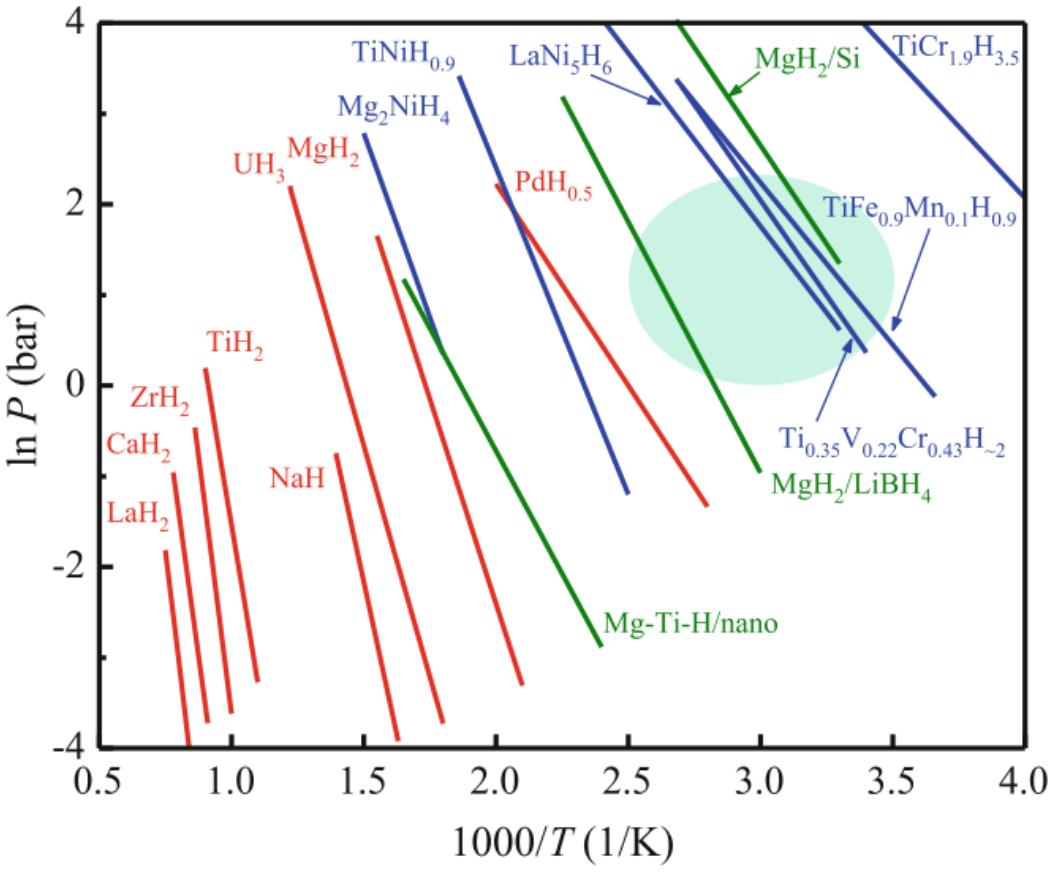

Figure 3.4: Van't Hoff plots of selected binary hydrides (red), hydrides of A_nB_m intermetallics (blue), and composite materials (green). The shaded area represents optimal operating conditions [32].

Additionally, the alloys exhibit hysteresis, wherein the absorption plateau pressure surpasses that observed during desorption, as illustrated in Figure 3.5. This phenomenon is commonly seen in metal hydrides and multiple theories seek to elucidate its origin. Proposed explanations involve factors such as plastic deformation during both hydride formation and decomposition, defects generation, particle size, and elastic strain energy [33–36].

Moreover, it is common to observe inclined plateaus, which are associated with heterogeneities in the chemical composition of metal alloys or intermetallic compounds. However, it's noteworthy that even pure metals can display inclined plateaus during absorption/desorption processes, suggesting the influence of other contributing factors. For example, internal stresses arising from abrupt volume changes during hydrogenation and dehydrogenation processes result in more pronounced inclinations at the onset and completion of hydride formation [37,38] .

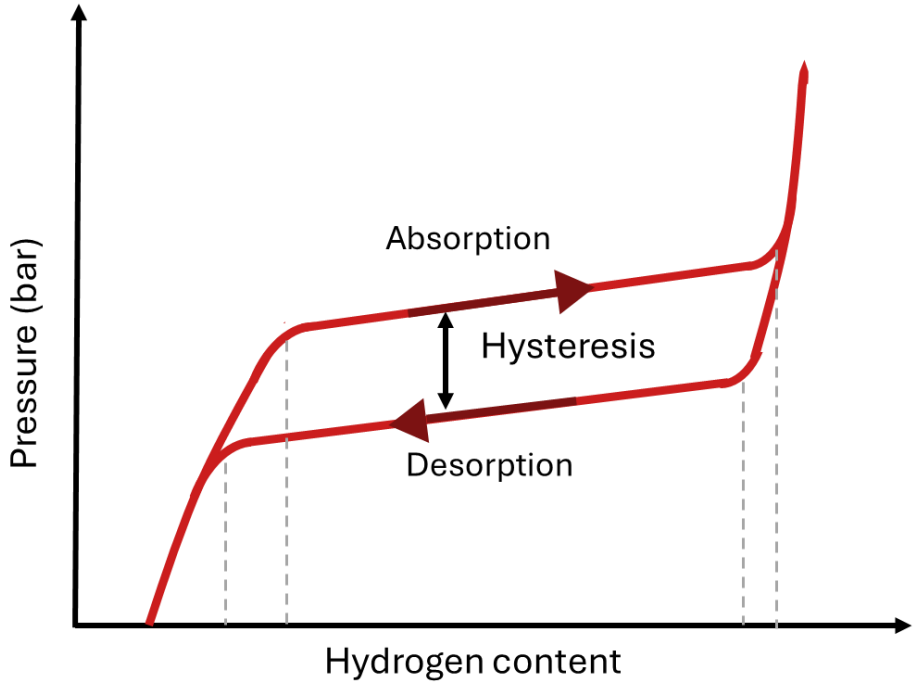

Figure 3.5: Schematic PCI curve with hysteresis and inclined plateaus for a hypothetical metal-hydrogen system.

3.3 Key Properties of Metal Hydrides

There are several key properties of metal hydrides that need to be thoroughly characterized when investigating new systems and considering their applications. Firstly, the gravimetric capacity refers to the amount of hydrogen stored per unit weight of metal, usually expressed as weight percentage (wt.%). In contrast, the reversible storage capacity is typically lower than the maximum gravimetric capacity and indicates the amount of hydrogen absorbed and desorbed between the lower and upper operating pressures [7]. The absorption capacity can also be expressed as H/M, which is the number of hydrogen atoms per number of metal atoms. Current alloys that can reversibly store hydrogen at room temperature generally have hydrogen storage capacity of 2-3 wt.%, presenting a challenge to design materials with higher capacities (> 5 wt.%). Achieving higher storage capacities would enable more compact storage solutions, which are essential for applications such as vehicles[37].

Another crucial property is the kinetics in absorption and desorption, which defines how rapidly the material can absorb and release hydrogen. The absorption kinetics initially depends on the probability of collision between hydrogen molecules and the metal's surface. Thus, a high surface area is essential for a higher absorption rate. Additionally, the absorption rate is also influenced by barriers such as the penetration of hydrogen into the subsurface and its further diffusion through the metal. From an application perspective, the kinetics of absorption and desorption are vital because they determine the refueling speed of the tank and whether the material can release hydrogen at a rate sufficient to supply the fuel cell during use [7,37].

The absorption reaction can vary from minutes to hours, but some materials cannot absorb hydrogen without an activation treatment. It is hypothesized that the activation process dissociates oxide layers on the surface into metals or sub-oxides [39]. These layers might prevent the dissociation of H_2 molecules into atoms and hinder the penetration of hydrogen atoms into the metal. Literature also suggests that activation processes induce crack formation, exposing fresh metallic surfaces to hydrogen, and creating lattice defects such as grain boundaries, stacking faults, and dislocations, which serve as pathways

for hydrogen atoms[34,35,40,41]. Materials that do not require activation to effectively absorb hydrogen are advantageous.

Moreover, the thermodynamic properties define metal hydrides' operating pressure and temperature ranges. The primary property is the enthalpy of hydride formation and decomposition. The amount of heat released during hydrogen absorption is determined by the enthalpy of formation (ΔH_f) of the hydride. During hydrogen desorption, the same amount of heat needs to be supplied. For most applications, a low desorption temperature is desirable to reduce the amount of heat required to release hydrogen, and, therefore, a less stable hydride is advantageous. Hydride stability, defined by the enthalpy of formation, is directly related to the plateau pressure in PCI curves - the higher the stability, the lower the plateau pressure. The enthalpy of formation of a hydride depends on the combination of the ΔH_f values of the binary hydrides of the elements composing the alloy. There are two groups of elements, as illustrated in Figure 3.6: hydride-forming elements (A), with negative values of the enthalpy of formation and higher metal-hydrogen (M-H) bonding strength, and non-hydride-forming (B), with positive values of enthalpy of formation and weaker M-H bond, providing lower decomposition temperatures [8,37,42].

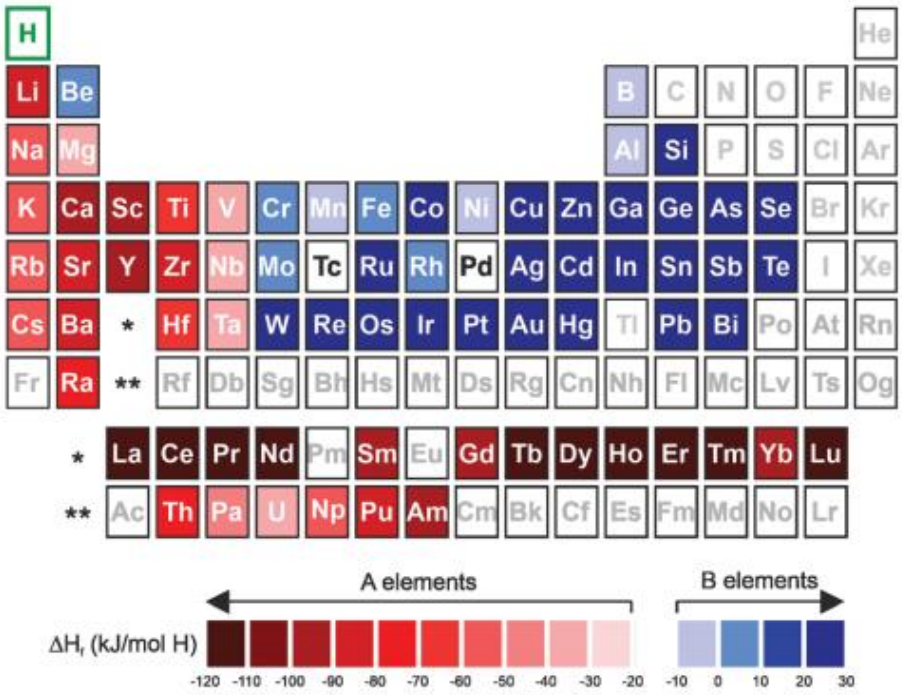

Figure 3.6: Periodic table illustrating the division between elements A and elements B based on the enthalpies of formation of their binary hydrides [8].

Finally, cycle stability is the ability of a metal hydride to retain its reversible storage capacity in multiple cycles of hydrogenation/dehydrogenation. The drop in capacity with the number of cycles is common and can be associated with several factors. For BCC alloys, for example, one possibility is that the structure does not fully revert to BCC upon hydrogen desorption, resulting in a combination of BCC monohydride and FCC dihydride. This incomplete reversion can lead to reduced hydrogen absorption capacity in subsequent cycles. In this context, the insertion of BCC-stabilizing elements could potentially favor the FCC→BCC transformation [10,43]. On the other hand, some authors have reported that the high stability of the intermediate hydride (β-phase) can result in incomplete hydrogen desorption. This incomplete desorption from the β-phase to the α-phase continuously lowers the hydrogen absorption capacity. Therefore, destabilizing the hydrides could potentially improve cycling performance. Additionally, other possible causes include the alloy disproportionation, structural distortion, defects insertion, phase segregation, and extensive amorphization [19,24,44–48].

In general, the investigation of new metal hydrides aims to develop materials with high gravimetric capacity, the highest possible reversible capacity, rapid kinetics of absorption and desorption, no need for activation for hydrogen absorption or easy activation, and cycling stability. Additionally, the operating conditions (equilibrium temperature and pressure for hydrogen absorption/desorption) should be suitable for the intended application. The U.S. Department of Energy (DOE) has established ultimate targets for onboard hydrogen storage in light-duty fuel cell vehicles. The DOE document specifies values for all relevant properties of metal hydrides. For example, the hydrogen desorption temperature must be lower than 85 °C [27].

3.4 Classes of Metal Hydrides

Multiple classes of metal hydrides are promising for hydrogen storage, each offering specific advantages and drawbacks concerning the key properties described in section 2.3. Magnesium-based alloys are lightweight materials that offer high hydrogen storage capacity (up to 7.6 wt.%) and low cost due to Mg's high natural abundance. However, the hydrides are highly stable and require high decomposition temperatures (~300 °C) due to the strong bonding between Mg and hydrogen. Besides, both absorption and desorption kinetics are slow. Multiple studies have been conducted seeking to improve the kinetics and lower the stability through the addition of transition elements [4,7,49].

Moreover, intermetallic compounds have gained importance for hydrogen storage. The general formula for intermetallic hydrides is $A_nB_mH_x$, where A is a hydride-forming element and B is a non-hydride-forming element, which contributes to destabilizing the hydride. Commonly studied families are AB (TiFe), AB_2 ($TiMn_2$), A_2B (Mg_2Ni), and AB_5 ($LaNi_5$) alloys. However, a significant drawback for the application of intermetallic hydrides is their low gravimetric capacity, which usually does not exceed 2 wt.%.

The most common AB-type compound is TiFe, which forms a cubic CsCl-type structure. It can operate under mild temperature and pressure conditions but requires an activation treatment before the initial hydrogenation [50]. The AB_5 family is represented by $LaNi_5$, which has rapid kinetics and presents reversibility at room temperature, though its maximum absorption capacity is lower than 1.5 wt.%. AB_2-type intermetallic compounds generally exhibit Laves Phase structures, such as C15, C14 and C36. For example, Laves Phases with A=Zr, such as ZrV_2, $ZrMn_2$, and $ZrCr_2$, form hydrides that show fast kinetics but are too stable at room temperature. In summary, for all these families, partial substitution at either the A or B site allows for tuning of their properties [49,51].

Building on the concept of tuning the properties of metal hydrides through alloying, which has been extensively studied for traditional systems such as Mg-based hydrides and intermetallic compounds, it is essential to introduce multicomponent alloys. These systems are based on three or more elements, with one or more base elements and the remaining elements present in small

fractions, and have been classified as BCC solid solutions, lightweight, and intermetallic multicomponent alloys [8,52,53]. BCC solid solutions are notable for their high hydrogen/metal ratios, reaching up to 2 H/M. Conventional compositions often utilize first-series transition metals like Ti, V, Cr, Mn, and Fe, taking advantage of their lower molar weights to achieve enhanced gravimetric capacity [8].

Given that the alloys studied in this work are BCC solid solutions, this type of metal hydride will be described in greater detail in this section. Hydrogenation in these systems occurs in two distinct stages, resulting in the formation of three different phases throughout the process. Initially, the α-phase forms, which is a solid solution with a BCC structure where hydrogen atoms occupy tetrahedral interstices. Subsequently, the β-phase forms, characterized as an intermediate hydride with structures that vary depending on the system. For instance, Nygard et al. [15] reported that TiVNb and TiVNbCr alloys exhibit β-phases with BCC structures. In contrast, Zlotea et al. [54] observed that an equiatomic TiZrNbHfTa alloy transitioned from a BCC α-phase to a body-centered tetragonal (BCT) β-phase. Finally, the δ-phase forms with a face-centered cubic (FCC) structure, in which hydrogen occupies tetrahedral interstices (CaF_2-type structure). The characteristic hydrogenation steps in BCC solid solutions result in two plateaus. The first occurs at low pressures, corresponding to the coexistence of the α- and β-phases, while the second plateau appears at higher pressures and is associated with the equilibrium between β- and δ-phases.

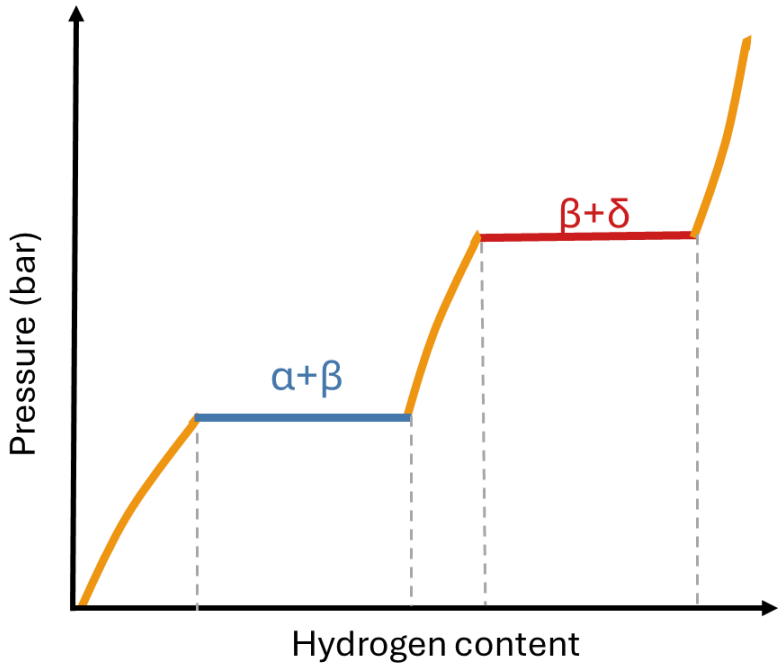

Figure 3.7: Illustration of a PCI curve with two plateau pressures for a hypothetical BCC system.

Among BCC solid solutions, the Ti-V-Cr and Ti-Nb-V-Cr systems are particularly noteworthy. Sapru et al.[55] reported alloys of the Ti-V-Cr system exhibiting storage capacities of approximately 4.0 wt.% and desorption of 2.8 wt.% at temperatures above 100 °C. Huang et al. [56] highlighted the $Ti_{35}V_{20}Cr_{45}$ alloy, which demonstrated good reversibility at relatively low temperatures, absorbing 3.2 wt.% at 40 °C and 20 atm and desorbing 2.0 wt.% at 60 °C and 0.1 atm. Additionally, Young et al. [43] reported excellent absorption/desorption kinetics, with compositions absorbing 80% of their storage capacity in 30 seconds and desorbing 80% in 90 seconds at temperatures above 110 °C.

For the Ti-V-Nb-Cr system, Nygard et al. [15] reported that the equiatomic TiVNbCr alloy had a reversible capacity of 1.96 wt.% at room temperature and moderate pressures, along with fast absorption kinetics. Strozi et al. [13] analyzed the effect of Cr content in $(TiVNb)_{100-x}Cr_x$ alloys, discovering that increasing the Cr content raises the plateau pressure in PCT diagrams without significantly affecting the maximum absorption capacity, which was 3.0 wt.%, 2.7 wt.%, and 2.8 wt.% for Cr contents of 15 at.%, 25 at.%, and 35 at.%, respectively. Silva et

al. [10] reported that the $Ti_{11}V_{30}Nb_{28}Cr_{31}$ alloy achieved a maximum absorption capacity of approximately 2.5 wt.% (1.6 H/M) with absorption and desorption plateau pressures of 10.3 bar and 1.7 bar, respectively, enabling reversibility at room temperature and moderate pressure conditions (~1.7 wt.%). In another study, the authors found that the $(TiVNb)_{85}Cr_{15}$ alloy had a maximum storage capacity of 3.18 wt.% (close to 2 H/M).

4 MATERIALS AND METHODS

4.1 Alloy Designing via Thermodynamic Calculation.

4.1.1 PCI Curves Calculation via Thermodynamic Model

A thermodynamic model developed by Zepon et al. [30] was utilized to calculate Pressure-Composition-Isotherm (PCI) curves for the selected compositions within the Ti-Nb-Cr system. The goal was to predict variations in plateau pressures based on composition before experimental measurements. This model, implemented in an open-source code by Pedroso et al. [57], calculates PCI curves of multicomponent BCC solid solution alloys by considering their chemical composition and structure.

Three phases typically associated with the hydrogen absorption process in BCC alloys are considered: α-phase, an interstitial BCC solid solution where hydrogen typically occupies the tetrahedral sites; β-phase, an intermediate hydride with variable structures that can be understood as an expanded BCC structure with hydrogen located in some preferential interstitial sites; and δ-phase, an FCC hydride with hydrogen occupying the tetrahedral sites (CaF_2-type structure). These phases may lead to two plateau pressures, the lower one corresponding to equilibrium between α and β phases and the higher one between the β and δ phases.

Given the prevalent application of solid-state hydrogen storage at low or moderate temperatures, the model adopts the para-equilibrium (PE) condition. To determine the chemical potentials, the model describes how the Gibbs free energy of each phase varies with hydrogen content. The mixing enthalpy of hydrogen in a phase is assumed to vary linearly with hydrogen content, according to equation 12:

$$\Delta H_m(c_H) = H_M + h_M \times \ c_H \qquad (12)$$

where H_M is a constant and h_M is the hydrogen partial molar enthalpy. Considering that the BCC alloy with $c_H = 0$ is taken as reference state, $H_M^{\alpha} = 0$. Additionally, when $c_H \to 0$, the α- and β- phases are almost identical, so $H_M^{\beta} = 0$. H_M^{δ} represents the enthalpy of phase transition from the BCC to the FCC structure and is given by equation 13:

$$H_M^{\delta} = E_{total}^{\delta} - E_{total}^{\alpha} \quad (13)$$

Where E_{total}^{δ} and E_{total}^{α} are the total energies for the δ- and α- phases, respectively. For multicomponent alloys, the total energies are obtained by considering the M-M bonds between the nearest neighbor atoms. These calculations were performed using Density Functional Theory (DFT) [57].

Additionally, h_M is assumed to be approximately the average hydrogen partial molar enthalpy of the pure elements in the same phase, as described by equation 14:

$$h_M = \sum_i c_i \times h_i \quad (14)$$

where c_i and h_i are the atomic fraction and hydrogen partial molar enthalpy for an element i, respectively. The values of h_i^{α} and h_i^{β} were determined from experimental data on the enthalpy of hydrogen solution at infinite dilution for the elements. The values of h_i^{δ} were obtained through total energy calculations using DFT [57].

Finally, for assessing entropy variation, the authors employed the configurational entropy model proposed by Garcés et al.[58]. This model accounts for the site-blocking effect (SBE), where the occupation of an interstitial site is hindered by the occupation of a neighboring site due to chemical and/or strain repulsion. Two key parameters, θ (number of interstitial sites per metal) and r (blocking parameter), are used for entropy-related calculation by applying equation 15:

$$\Delta S_m(c_H) = -R\left[c_H\, In\left(\frac{c_H}{\theta - [(r-1)c_H]}\right) + (\theta - rc_H)\, In\left(\frac{\theta - rc_H}{\theta - [(r-1)c_H]}\right)\right] - \frac{c_H}{2} S°(H_2) \quad (15)$$

where R is the ideal gas constant. The parameters applied for the reported calculations in this work were: θ = 6 and r = 7 for the α phase, θ = 4 and r = 2 for the β phase and θ = 2 and r = 1 for the δ phase [57].

4.1.2 CALPHAD Method

The CALPHAD (Calculation of Phase Diagrams) method utilizes computational tools to calculate equilibrium phase diagrams. In this method, thermodynamic models represented by polynomial forms, specifically Redlich-Kister functions, are employed to compute the Gibbs free energy of competing phases. Parameters for these functions are determined using a combination of reliable experimental and theoretical data. Consequently, the identification of the thermodynamic equilibrium phase at various temperatures is achieved by minimizing the free-energy approximations of competing phases, thereby constructing a phase diagram [8,59]. For this study, the Thermo-Calc software and TCHEA5 database were utilized as the implementation platform for the CALPHAD method, facilitating the computation of equilibrium phases for the designed alloys.

4.2 Synthesis of Alloys

The $Ti_{1.0}Nb_{1.0}Cr_{1.0}$, $Ti_{0.8}Nb_{1.4}Cr_{1.0}$, $Ti_{0.6}Nb_{1.8}Cr_{1.0,}$ and $Ti_{0.4}Nb_{2.2}Cr_{1.0}$ alloys were synthesized via arc-melting using an Edmund Bühler GmbH furnace. High-purity titanium (99.7%), niobium (99.8%), and chromium (99.995%) pieces were used as feedstock. The melting process was conducted under an inert argon atmosphere, and the ingots were subjected to a minimum of ten melting repetitions to ensure chemical homogenization. The ingots were then stored in an MBRAUM glovebox with an argon atmosphere, maintaining H_2O and O_2 levels below 1 ppm. Samples for structural characterization were obtained from the ingots using an ISOMET cutting machine.

4.3 Structural Characterization

4.3.1 X-Ray Diffraction (XRD)

X-ray diffraction (XRD) analyses were conducted to identify the phases present in both the as-cast ingots and the hydrogenated alloys. Diffractograms were acquired using a Bragg-Brentano Bruker D8 Advance Eco diffractometer

with KαCu radiation ($K_{\alpha1}$=1.5406 Å, $K_{\alpha2}$=1.5444 Å) operating at 40 kV and 25 mA. The Rietveld refinement method, implemented via the General Structure Analysis System II (GSAS II) software, was used to analyze the patterns and determine the lattice parameters and phase fractions. The refined parameters included background, lattice parameter, crystallite size, and isotropic micro-strain.

4.3.2 Synchrotron Radiation X-ray Diffraction (SR-XRD)

Synchrotron radiation X-Ray diffraction (SR-XRD) measurements were carried out in different conditions of the $Ti_{0.8}Nb_{1.4}Cr_{1.0}$ alloy at the ID11 beamline at European Synchrotron Radiation Facility (ESRF) in Grenoble, France. This beamline is specialized in moderate to high energy diffraction and imaging studies. The X-ray wavelength used for these measurements was 0.1899 Å (65.3508 keV). Rietveld refinement analyses were performed using the GSAS II software. The selection of the $Ti_{0.8}Nb_{1.4}Cr_{1.0}$ alloy for analysis was based on the fact that it was the only alloy for which all cycling experiments had been completed at the time of the synchrotron experiments.

4.3.3 Scanning Electron Microscopy (SEM) and Energy Dispersive X-Ray (EDX)

The microstructure of the alloys was analyzed using a Philips XL-30 FEG Scanning Electron Microscope (SEM), which acquired backscattered electron (BSE) images at a working distance of 10 mm and an acceleration voltage of 25 kV. The chemical composition was assessed by Energy Dispersive X-ray (EDX) analysis using a Bruker Nano XFlash 6|60 EDX Detector. Before the analyses, the samples extracted from the ingots were ground with SiC papers of mesh sizes 240, 400, 600, and 1200, followed by polishing with a 1 µm alumina suspension.

4.4 Hydrogen Storage Properties Measurements

The hydrogen storage properties were investigated using a Sieverts-type apparatus (SETARAM® PCT-Pro), illustrated in Figure 4.1. Before the analyses, the ingots were crushed into small pieces using a stainless-steel mortar and pestle inside the glovebox. A sample mass between 300 mg and 700 mg was

then loaded into a dedicated sample holder. First, the volume of the sample holder is calibrated at the experiment temperature. During the absorption process, the reference volume is filled with a predetermined hydrogen pressure. Subsequently, the isolation valve between the reference volume and the sample volume is opened, allowing the gas to equilibrate between both volumes. By measuring the change in pressure, it is possible to determine the quantity of hydrogen absorbed.

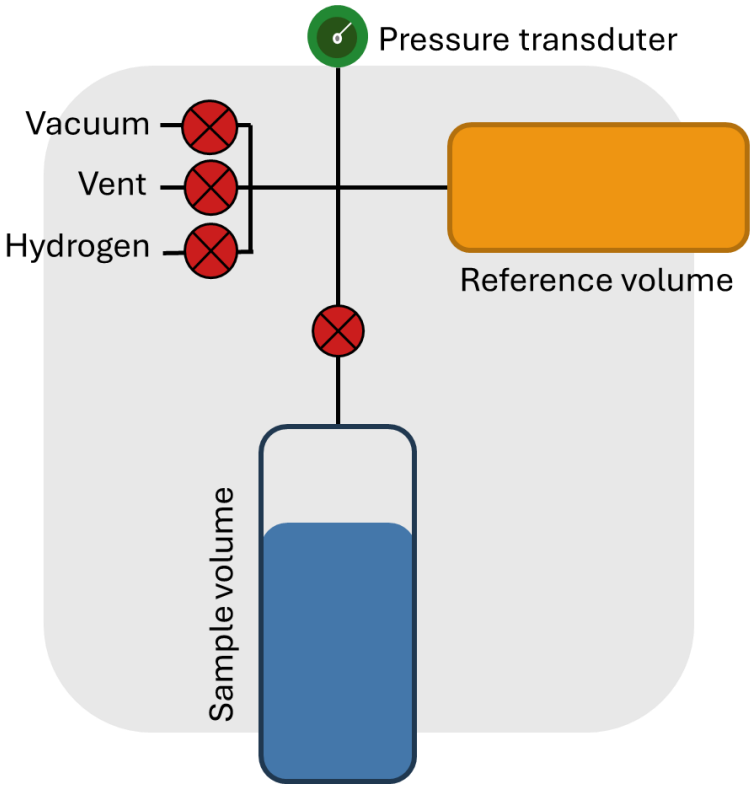

Figure 4.1: Illustration of a Sieverts-type apparatus.

The initial hydrogenation kinetic measurements were carried out at room temperature (~25 °C) under a hydrogen pressure ranging from 25 to 40 bar. These measurements were first performed without any activation treatment and then repeated after an activation treatment at 400 °C under dynamic vacuum for 2 h, a procedure analogous to that previously reported as effective for activating Ti-V-Nb-Cr alloys [14,15].

Pressure-Composition-Isotherms measurements were conducted at temperatures ranging from 25 °C to 150 °C in both absorption and desorption conditions by incrementally adding doses of hydrogen up to a maximum pressure

of approximately 70 bar. Before the first PCI measurement for each sample, a complete cycle of hydrogenation at 25 °C followed by dehydrogenation at 400 °C under dynamic vacuum for 2 h was performed to ensure the alloy's full activation. The H_2 doses were added to a 13 cm^3 reservoir and adjusted throughout the experiment based on the H_2 pressure and temperature. Following each PCI measurement, complete hydrogen desorption was carried out at 400 °C in dynamic vacuum for 2 hours. The PCI curves obtained at different temperatures were utilized to calculate both the plateau enthalpy (ΔH_{Plat}) and plateau entropy (ΔS_{Plat}) using the Van't Hoff equation (equation 11).

The hydrogen desorption mechanism was investigated using a combination of differential scanning calorimetry (DSC), thermogravimetry analysis (TGA), and quadrupole mass spectrometry (QMS). These techniques allow for the simultaneous monitoring of heat release or absorption, mass loss, and gas releases during the heating process. The experiments were performed using a Netzsch STA 449 C instrument, with around 15 mg of hydrogenated material contained in an alumina crucible. The experimental conditions involved a constant argon flow of 25 cm^3/min and a heating rate of 10 K/min, reaching a maximum temperature of 550 °C.

The reduction in maximum hydrogen storage capacity over absorption/desorption cycles is a well-documented phenomenon in alloys such as TiVNbCr and TiVCr. To investigate this, the hydrogen absorption capacity of the $Ti_{1.0}Nb_{1.0}Cr_{1.0}$, $Ti_{0.8}Nb_{1.4}Cr_{1.0}$, $Ti_{0.6}Nb_{1.8}Cr_{1.0,}$ and $Ti_{0.4}Nb_{2.2}Cr_{1.0}$ alloys was measured over 10 absorption/desorption cycles. The cycled samples underwent a comprehensive characterization via SR-XRD and DSC/TGA/QMS experiments.

5 RESULTS AND DISCUSSION

5.1 Alloy Designing via Thermodynamic Modeling

The PCI diagrams calculated at 25 °C for the investigated compositions are illustrated in Figure 5.1. It is noteworthy that the thermodynamic model [30] predicted only a plateau pressure related to the equilibrium between the α- (BCC solid solution) and δ- (FCC hydride) phases for all compositions. This observation is consistent with the findings of Silva et al. [60] and Strozi et al. [14] in different compositions of the Ti-V-Nb-Cr system. However, experimental curves in both works exhibited two equilibrium plateau pressures: a lower plateau pressure corresponding to the equilibrium between the α- and β- (BCC intermediate hydride) phases and a higher plateau pressure related to the equilibrium between the β- and δ- phases. Remarkably, the experimental values of the higher plateau pressure agreed with the calculated ones in both works. The model's relatively precise prediction of the higher plateau can be attributed to the description of the β- and α- phases as similar BCC structures.

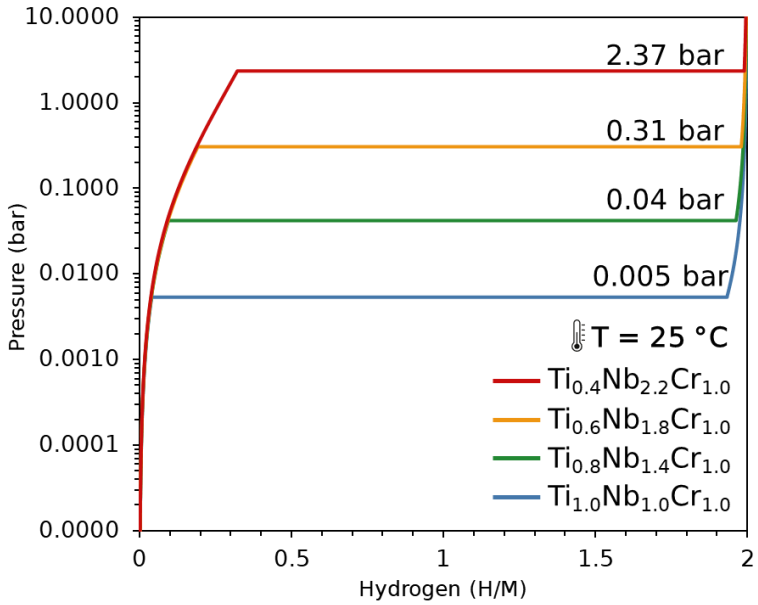

Figure 5.1: PCI curves at 25 °C for the $Ti_{1.0}Nb_{1.0}Cr_{1.0}$, $Ti_{0.8}Nb_{1.4}Cr_{1.0}$, $Ti_{0.6}Nb_{1.8}Cr_{1.0}$, and $Ti_{0.4}Nb_{2.2}Cr_{1.0}$ alloys calculated using the thermodynamic model proposed by Zepon et al. [30].

In Figure 5.1, it's evident that the plateau pressure increases notably with increasing the Nb/Ti ratio. The equiatomic alloy displays a calculated plateau

pressure of 0.005 bar, whereas the $Ti_{0.4}Nb_{2.2}Cr_{1.0}$ alloy presents a plateau of 2.37 bar, marking an increase of three orders of magnitude.

Figure 5.2 presents the diagrams of equilibrium phase fraction versus temperature, calculated by CALPHAD for the four compositions under investigation. In all compositions, solidification initiates with the formation of a BCC phase. Extensive solidification intervals – the temperature interval between liquidus and solidus temperatures – are observed across all the alloys, which increase with higher Nb content, reaching 410 °C for the $Ti_{0.4}Nb_{2.2}Cr_{1.0}$ alloy. Between 1470 °C and 1576 °C, solidification concludes with the formation of a C14 Laves phase (P63/mmc space group) for all the alloys, with its fraction increasing upon cooling. From 1210 °C to 1340 °C, the C14 phase transitions into a C15 Laves phase (Fd-3m space group). CALPHAD calculations consistently show a decrease in the BCC phase fraction as the C15 fraction rises.

It’s crucial to note, however, that this prediction assumes equilibrium conditions during solidification. The arc melting process for small ingots (~10 g) is characterized by rapid cooling, resulting in non-equilibrium solidification. Consequently, phases formed at high temperatures, such as the BCC phase, likely retain a significant fraction at low temperatures. Some authors have reported that Laves phase formation might even be prevented by rapid cooling in some compositions of the Ti-V-Nb-Cr system [11,13].

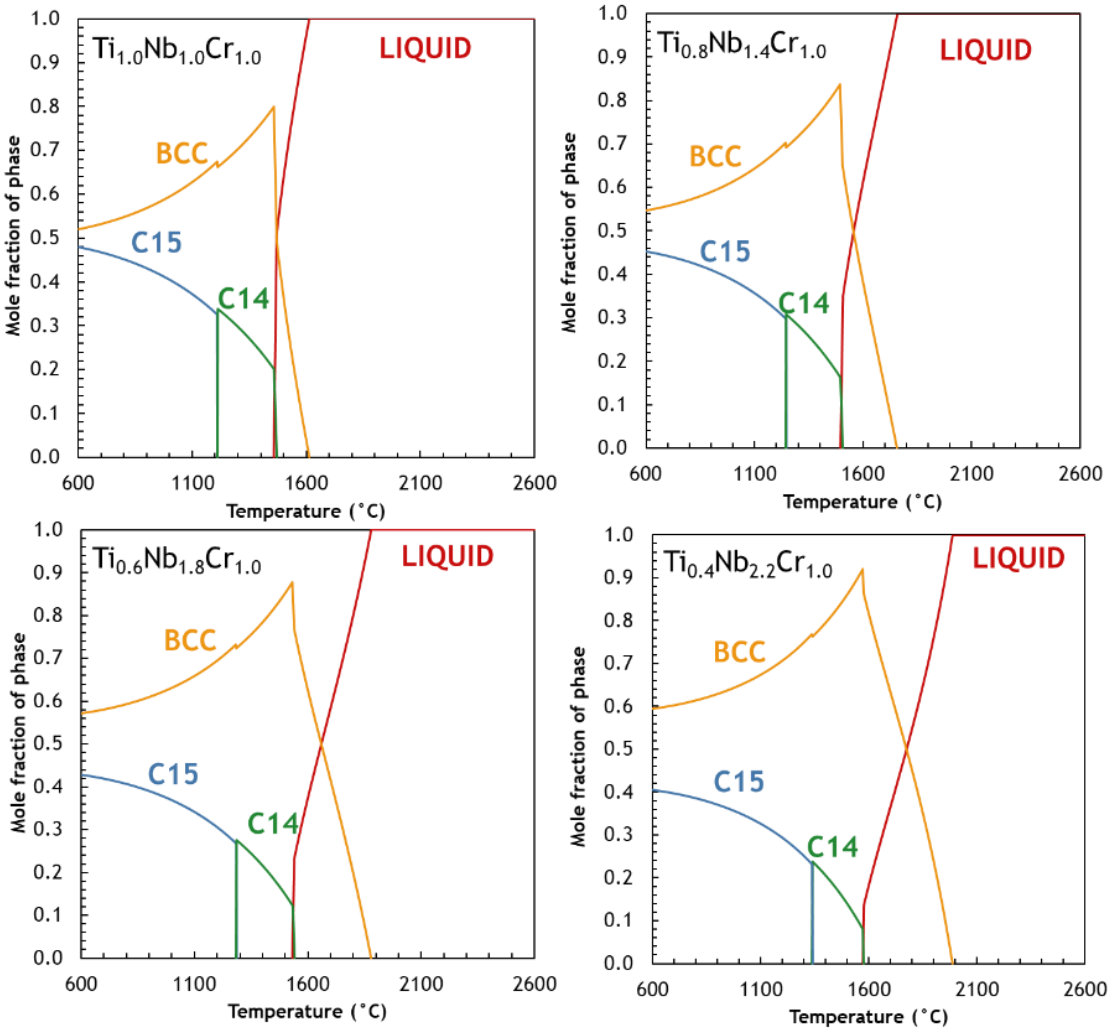

Figure 5.2: Mole fraction of the equilibrium phases as a function of temperature calculated using the CALPHAD method for the $Ti_{1.0}Nb_{1.0}Cr_{1.0}$, $Ti_{0.8}Nb_{1.4}Cr_{1.0}$, $Ti_{0.6}Nb_{1.8}Cr_{1.0}$, and $Ti_{0.4}Nb_{2.2}Cr_{1.0}$ alloys.

5.2 Structural Characterization

The XRD patterns of the as-cast $Ti_{1.0}Nb_{1.0}Cr_{1.0}$, $Ti_{0.8}Nb_{1.4}Cr_{1.0}$, $Ti_{0.6}Nb_{1.8}Cr_{1.0}$, and $Ti_{0.4}Nb_{2.2}Cr_{1.0}$ alloys are shown in Figure 5.3. Although CALPHAD calculations predict a significant fraction of the C15 phase at low temperatures, a predominant BCC phase is observed, with small intensity diffraction peaks attributed to the C15 Laves phase. The results of the Rietveld refinement analysis, including phase concentrations and lattice parameters of the phases, are summarized in Table 5.1. The Rietveld refinement plots are provided in Appendix A.

The BCC solid solution was described by the random occupation of the 2a Wyckoff position of the Im-3m space group by Ti, Nb, and Cr. The site occupation factor was determined based on the chemical compositions of the dendrites measured by EDX for each alloy (refer to Table 5.2). For the C15 Laves phase, it was considered as the (Ti,Nb)Cr_2 intermetallic compound, with the 8a Wyckoff position randomly occupied by Ti and Nb (each with an occupation factor of 50%), and Cr occupying the 16d Wyckoff position of the Fd-3m space group.

An increase in the lattice parameters of the BCC phases is observed with higher Nb/Ti ratios. For the intermediate compositions, $Ti_{0.8}Nb_{1.4}Cr_{1.0}$ and $Ti_{0.6}Nb_{1.8}Cr_{1.0}$, the lattice parameters are very similar. In terms of the C15 Laves phase, all alloys show comparable lattice parameters. The phase concentrations analysis indicates that the equiatomic alloy has a significantly lower C15 fraction (2.8%) compared to the other alloys, which range from 8.7 wt.% for the $Ti_{0.6}Nb_{1.8}Cr_{1.0}$ alloy to 12.7 wt.% for the $Ti_{0.8}Nb_{1.4}Cr_{1.0}$ alloy.

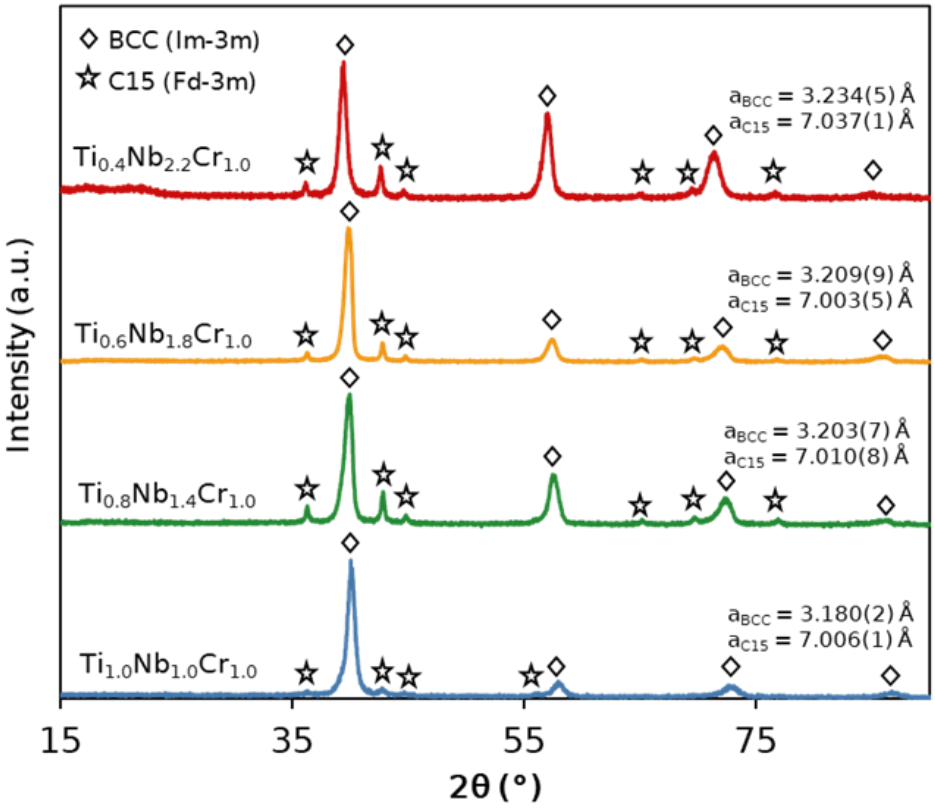

Figure 5.3: Indexed XRD patterns of the as-cast $Ti_{1.0}Nb_{1.0}Cr_{1.0}$, $Ti_{0.8}Nb_{1.4}Cr_{1.0}$, $Ti_{0.6}Nb_{1.8}Cr_{1.0}$, and $Ti_{0.4}Nb_{2.2}Cr_{1.0}$ alloys.

Table 5.1: Lattice parameters and phase concentrations determined via Rietveld refinement of XRD patterns for as-cast and first-hydrogenated states of $Ti_{1.0}Nb_{1.0}Cr_{1.0}$, $Ti_{0.8}Nb_{1.4}Cr_{1.0}$, $Ti_{0.6}Nb_{1.8}Cr_{1.0}$, and $Ti_{0.4}Nb_{2.2}Cr_{1.0}$ alloys.

	As-cast				Hydrogenated					
	Lattice parameters (Å)		Phase concentrations (wt.%)		Lattice parameters (Å)			Phase Concentrations (wt.%)		
Alloy	BCC	C15	BCC	C15	BCC	FCC	C15	BCC	FCC	C15
$Ti_{1.0}Nb_{1.0}Cr_{1.0}$	3.180(2)	7.006(1)	97.2	2.8	X	4.415(9)	7.025(7)	X	95.7	4.3
$Ti_{0.8}Nb_{1.4}Cr_{1.0}$	3.203(7)	7.010(8)	87.3	12.7	X	4.446(6)	7.033(4)	X	81.0	19.0
$Ti_{0.6}Nb_{1.8}Cr_{1.0}$	3.209(9)	7.003(5)	91.3	8.7	X	4.454(1)	7.031(3)	X	90.0	10.0
$Ti_{0.4}Nb_{2.2}Cr_{1.0}$	3.234(5)	7.037(1)	87.9	12.1	3.329(8)	4.470(3)	7.025(9)	9.4	77.1	13.5

Figure 5.4 displays the BSE-SEM micrographs of the as-cast alloys. All microstructures exhibit a dendritic morphology. Microsegregation is evident, having occurred during the solidification process. Systematic EDX measurements were performed across different areas of the samples, and the average chemical composition of each alloy is summarized in Table 5.2. The analyses confirmed the alloys' homogeneity and the absence of partially melted pure elements, with no macrosegregation detected throughout the ingot.

Furthermore, compositions were measured separately in the interdendritic regions (dark grey contrast) and within the dendrites (light grey contrast). This confirmed a Cr microsegregation, with Cr-rich interdendritic regions and Nb-rich dendrites, while Ti content remained relatively uniform across both areas. Alloys with higher Nb and lower Ti contents exhibited more significant Cr microsegregation, resulting in increasingly Nb-richer dendrites and Cr-richer interdendritic regions. This phenomenon is associated with the increase in solidification intervals as the Nb/Ti ratio rises. The microsegregation occurs because solutes are rejected by the solid during solidification, as the solubility in the solid phase is lower compared to the liquid phase. Therefore, wider solidification intervals lead to greater solute enrichment (in this case, Cr) in the

interdendritic regions [61]. The C15 Laves phase is likely located in the interdendritic region, where chromium concentration is higher.

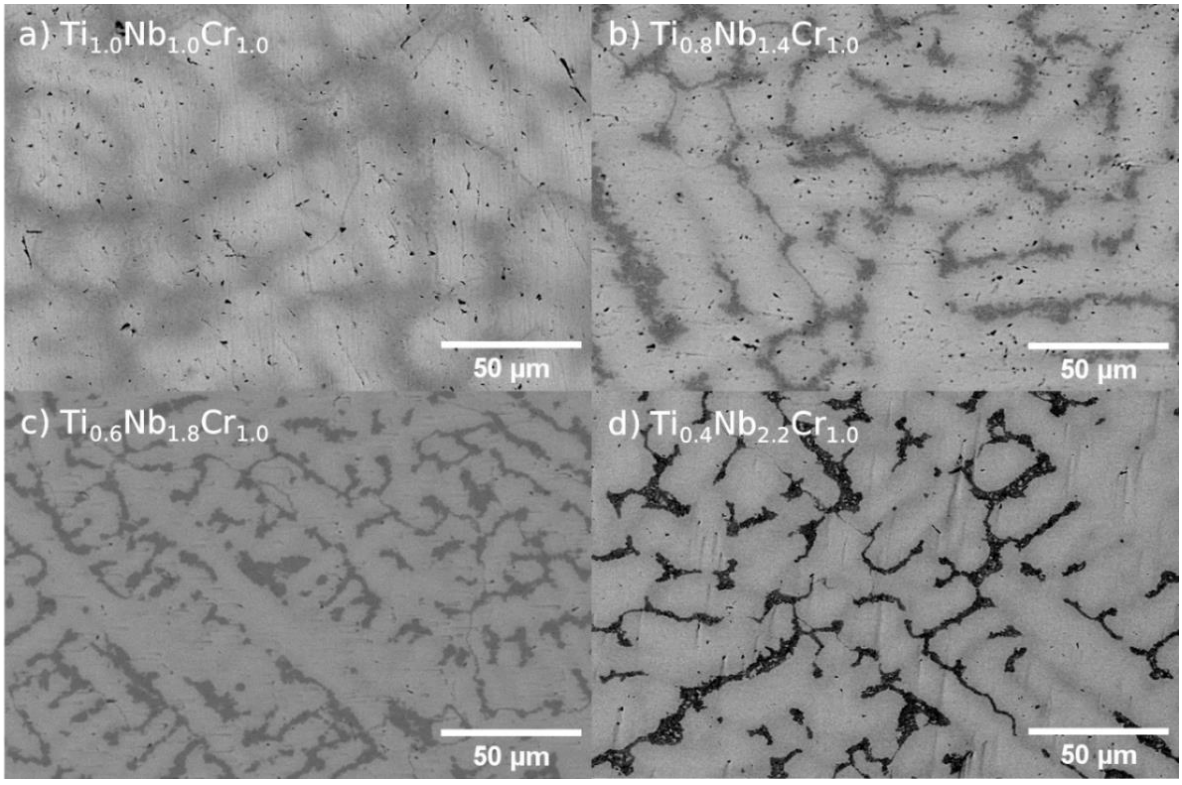

Figure 5.4: SEM-BSE images of the a) $Ti_{1.0}Nb_{1.0}Cr_{1.0}$, b) $Ti_{0.8}Nb_{1.4}Cr_{1.0}$, c) $Ti_{0.6}Nb_{1.8}Cr_{1.0}$, and d) $Ti_{0.4}Nb_{2.2}Cr_{1.0}$ alloys.

Table 5.2: Chemical compositions of the $Ti_{1.0}Nb_{1.0}Cr_{1.0}$, $Ti_{0.8}Nb_{1.4}Cr_{1.0}$, $Ti_{0.6}Nb_{1.8}Cr_{1.0}$, and $Ti_{0.4}Nb_{2.2}Cr_{1.0}$ alloys determined via SEM-EDX.

Alloy		Nominal (at.%)	General (at.%)	Dendrites (at.%)	Interdendritic regions (at.%)
$Ti_{1.0}Nb_{1.0}Cr_{1.0}$	**Ti**	33.3	34.8 ± 0.2	36.3 ± 0.5	38.3 ± 0.2
	Nb	33.3	34.3 ± 0.6	32.3 ± 1.0	26.5 ± 1.9
	Cr	33.3	30.8 ± 0.5	31.4 ± 0.6	35.2 ± 2.1
$Ti_{0.8}Nb_{1.4}Cr_{1.0}$	**Ti**	25.0	23.8 ± 1.0	21.3 ± 0.9	25.0 ± 1.2
	Nb	43.8	47.1 ± 2.9	57.7 ± 3.0	46.9 ± 2.8
	Cr	31.3	29.1 ± 2.1	21.0 ± 2.0	28.1 ± 1.5
$Ti_{0.6}Nb_{1.8}Cr_{1.0}$	**Ti**	17.7	19.8 ± 0.2	16.3 ± 0.7	16.1 ± 1.0
	Nb	52.9	49.4 ± 1.0	61.0 ± 2.0	31.5 ± 1.7
	Cr	29.4	30.9 ± 1.0	22.7 ± 1.3	52.4 ± 2.7

$Ti_{0.4}Nb_{2.2}Cr_{1.0}$	**Ti**	11.1	11.9 ± 0.2	11.0 ± 0.5	8.9 ± 0.2
	Nb	61.1	60.6 ± 0.6	70.6 ± 2.1	28.7 ± 1.7
	Cr	27.8	27.6 ± 0.5	18.4 ± 1.7	62.4 ± 1.5

The microsegregation is visible in the EDX elemental maps. Figure 5.5 presents the mappings for the $Ti_{0.4}Nb_{2.2}Cr_{1.0}$, which exhibits the most intense microsegregation. The mappings for the other three alloys are available in Appendix B. Some studies have suggested that homogenizing the alloys could enhance their hydrogen storage properties [62–65]. However, according to CALPHAD predictions, heat treatments are not suitable for the alloys in the present work, as they would promote the formation of equilibrium phases, consequently increasing the fraction of the C15 Laves Phase (refer to Figure 5.2). This phase does not possess hydrogen storage properties as favorable as those of the BCC phase, according to kinetics results in section 5.3.

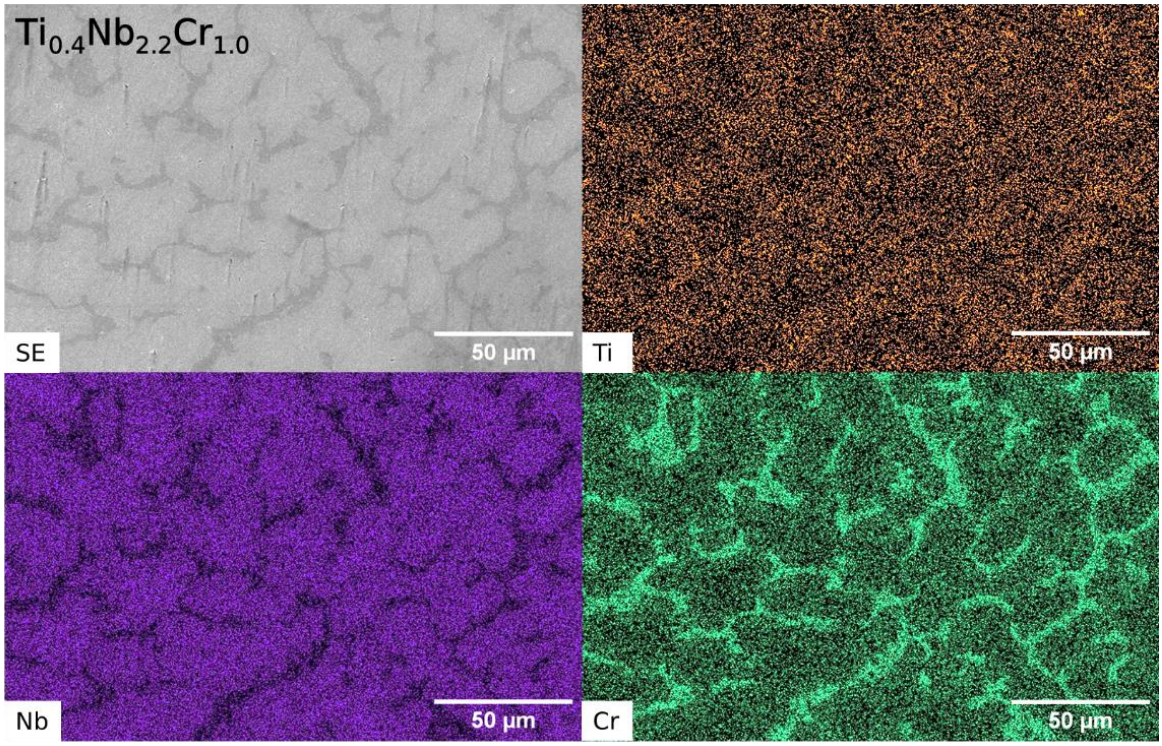

Figure 5.5: EDX elemental maps of the as-cast $Ti_{0.4}Nb_{2.2}Cr_{1.0}$.

Analyzing the average chemical compositions of the alloys provides insights into the observed increase in the lattice parameter of the BCC phase with

higher Nb content and reduced Ti content. Although the atomic radii of Ti and Nb (1.46 Å and 1.47 Å, respectively) are very similar, the smaller radius of Cr (1.28 Å) significantly influences the lattice parameters [66]. The chemical compositions show a decrease in Cr content as Nb content rises and Ti content decreases. As a result, the lattice parameters increase from the $Ti_{1.0}Nb_{1.0}Cr_{1.0}$ to the $Ti_{0.4}Nb_{2.2}Cr_{1.0}$ alloy.

5.3 Hydrogen Absorption Kinetics

Hydrogen absorption kinetics measurements (Figure 5.6) were performed at room temperature under H_2 pressures ranging from 25 to 40 bar, revealing rapid absorption kinetics across all alloys. However, the equiatomic alloy exhibited a prolonged incubation time – the interval between the start of the experiment and the onset of hydrogen absorption - compared to the other alloys. Consequently, the impact of activation on absorption kinetics was evaluated. The activation process was conducted at 400 °C for 2 hours under dynamic vacuum. Following activation, the observed incubation time for the equiatomic alloy disappeared, and all alloys reached their maximum capacities in less than 2 minutes. The maximum storage capacities remained nearly unaltered after activation. Notably, the equiatomic alloy exhibited a superior value compared to the other alloys. The gravimetric capacities decrease with increasing the Nb/Ti ratio, likely due to the higher molar weight of Nb (92.90 g/mol) compared to Ti and Cr (47.86 and 52.0 g/mol, respectively).

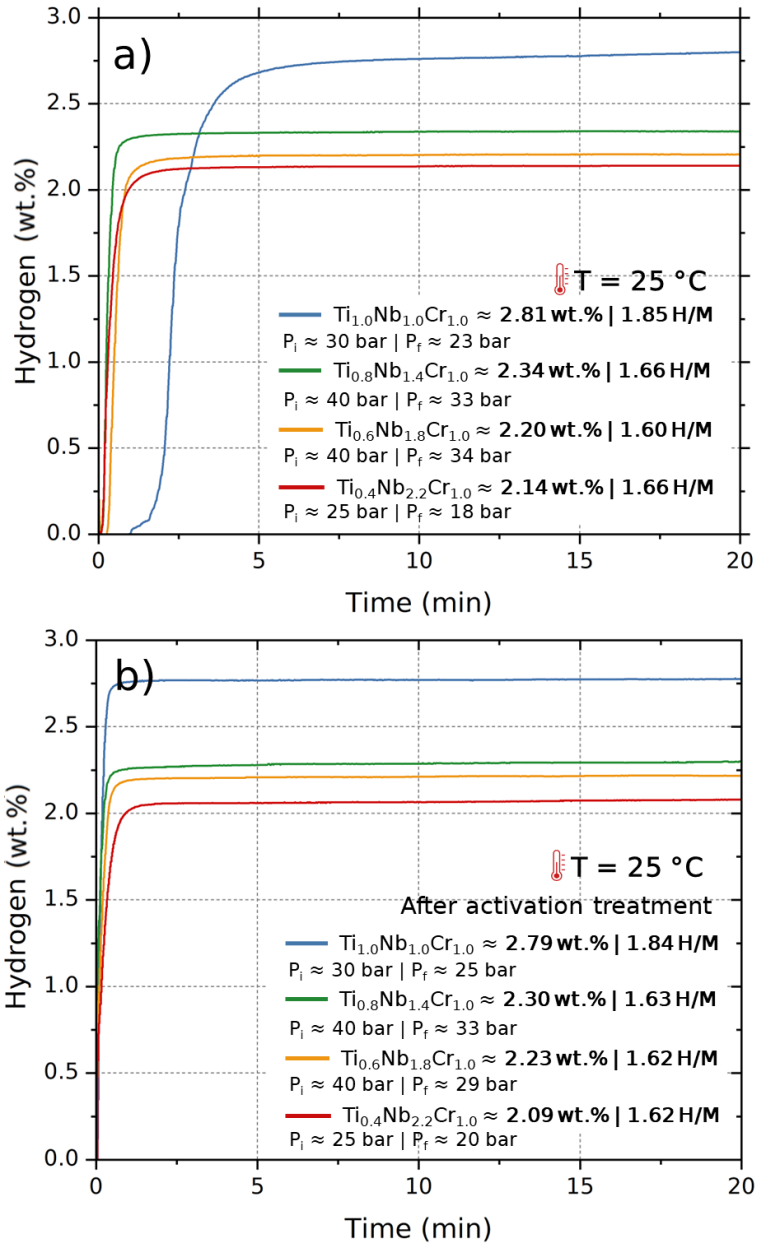

Figure 5.6: Hydrogen absorption kinetics curves at 25 °C for a) non-activated, and b) thermally activated $Ti_{1.0}Nb_{1.0}Cr_{1.0}$, $Ti_{0.8}Nb_{1.4}Cr_{1.0}$, $Ti_{0.6}Nb_{1.8}Cr_{1.0}$, and $Ti_{0.4}Nb_{2.2}Cr_{1.0}$ alloys.

The XRD patterns obtained from the samples after the first hydrogenation are illustrated in Figure 5.7. All hydrides display a face-centered cubic (FCC) phase along with the C15 Laves phase. Interestingly, the diffractogram of the $Ti_{0.4}Nb_{2.2}Cr_{1.0}$ alloy reveals a peak corresponding to the BCC phase. This implies

that partial desorption of hydrogen from this sample may occur spontaneously upon removal from the sample holder.

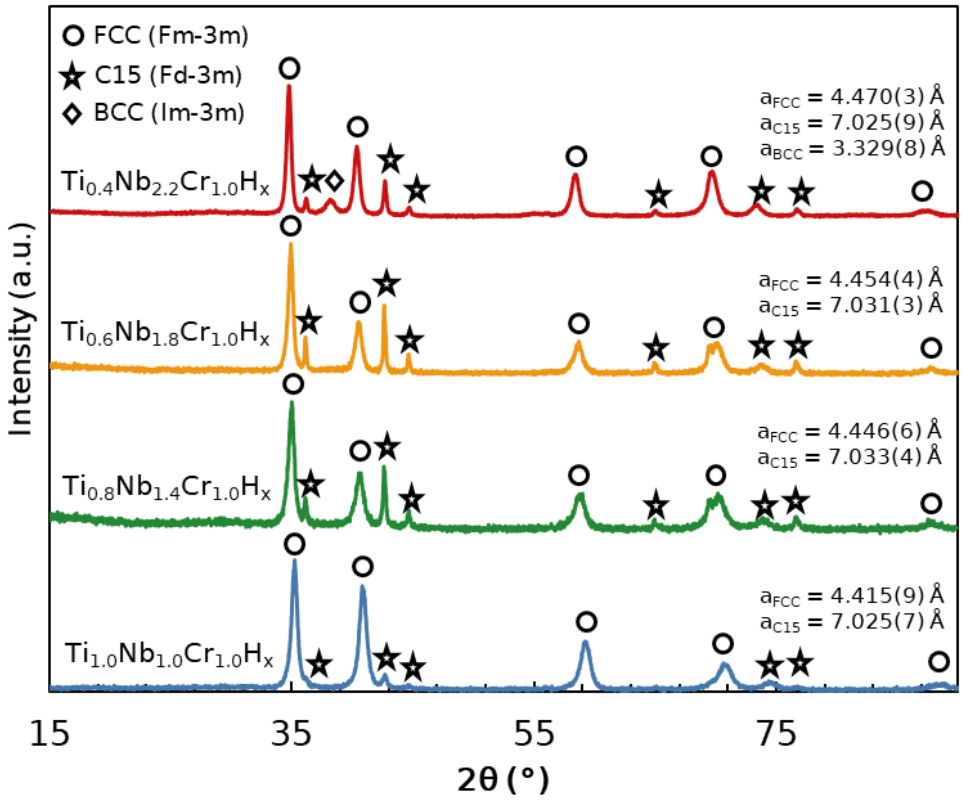

Figure 5.7: Indexed XRD patterns of the hydrogenated $Ti_{1.0}Nb_{1.0}Cr_{1.0}$, $Ti_{0.8}Nb_{1.4}Cr_{1.0}$, $Ti_{0.6}Nb_{1.8}Cr_{1.0}$, and $Ti_{0.4}Nb_{2.2}Cr_{1.0}$ alloys.

Table 5.1 presents the lattice parameters of FCC, BCC, and C15 phases in the hydrogenated alloys determined via Rietveld refinement (refer to Appendix A for the corresponding Rietveld refinement plots). Consistent with the observed trend in the BCC phase of the as-cast alloy, the FCC phase also exhibits an increased lattice parameter with higher Nb content and simultaneous reductions in both Ti and Cr content (as determined by compositions measured via EDX). Particularly noteworthy is that the lattice parameter of the BCC phase in the hydrogenated $Ti_{0.4}Nb_{2.2}Cr_{1.0}$ alloy exceeds that of the BCC phase in the as-cast sample by 0.096 Å. According to the Peisl relationship [67], the volume occupied by an interstitial hydrogen atom falls within the ranges of 2.0 and 2.9 A^3. By applying this criterion, the expected content within the BCC phase would range between 0.529 and 0.767 H/M (corresponding to 0.69 and 1.0 wt.%).

An important observation is the minimal change in the lattice parameters of the C15 Laves phase from the as-cast to hydrogenated alloys. This implies a minimal presence of hydrogen within the C15 phase in the hydrogenated samples. Johnson et al. [68] investigated the C15 Laves phase $TiCr_{1.8}$ and reported PCT diagrams revealing notably high plateau pressures. At -90 °C, the curve displayed a first plateau at 1 bar and a second plateau at around 20 bar, reaching a maximum capacity of 1.2 H/M. The authors identified the formation of two hydrides: an α' Laves phase and an FCC phase. [69] Considering measurements at room temperature and moderate pressures (25 - 40 bar), it is expected that hydrogen absorption would be limited to the formation of a solid solution without reaching its solubility limit. Additionally, since the C15 Laves phase formed in the Ti-Nb-Cr alloys is likely associated with $(Ti,Nb)Cr_2$, where both Ti and Nb occupy the sub-lattice A, it is anticipated that its equilibrium pressure would exceed that of $TiCr_2$. This expectation arises from the less negative enthalpy of the hydrogen solution of Nb compared to Ti, indicating a weaker hydride-forming element. Therefore, achieving maximum absorption in the C15 Laves phase (close to 1 H/M [70]) would require either high pressures or very low temperatures.

The decrease in maximum hydrogen capacity (H/M) with increasing the Nb/Ti ratio, as shown in Figure 5.6, can be attributed to the C15 Laves phase's inability to absorb hydrogen under the pressure and temperature conditions used in the kinetics experiments. XRD results for the as-cast samples indicated that the fraction of the C15 Laves phase increases as the Nb/Ti ratio increases. Since this phase does not significantly contribute to hydrogen absorption, the overall maximum capacity is reduced. Therefore, it appears advantageous to design alloys with the lowest possible fraction of the C15 phase. Phase diagrams obtained using the CALPHAD method suggest that this could be achieved by further reducing the Cr content. However, reducing Cr, the non-hydride forming element in the system, would result in increased hydride stability.

The hydrogenated samples underwent characterization via SEM, and the SE micrographs are presented in Figure 5.8. Cracks were observed in the particles due to the volume expansion upon hydrogen absorption, a phenomenon

known as pulverization inherent to hydrogen absorption processes. This process significantly reduces the particle size and increases the surface area, becoming more intense with an increase in the number of absorption/desorption cycles, especially for brittle materials such as C14 Laves Phase alloys [53,71].

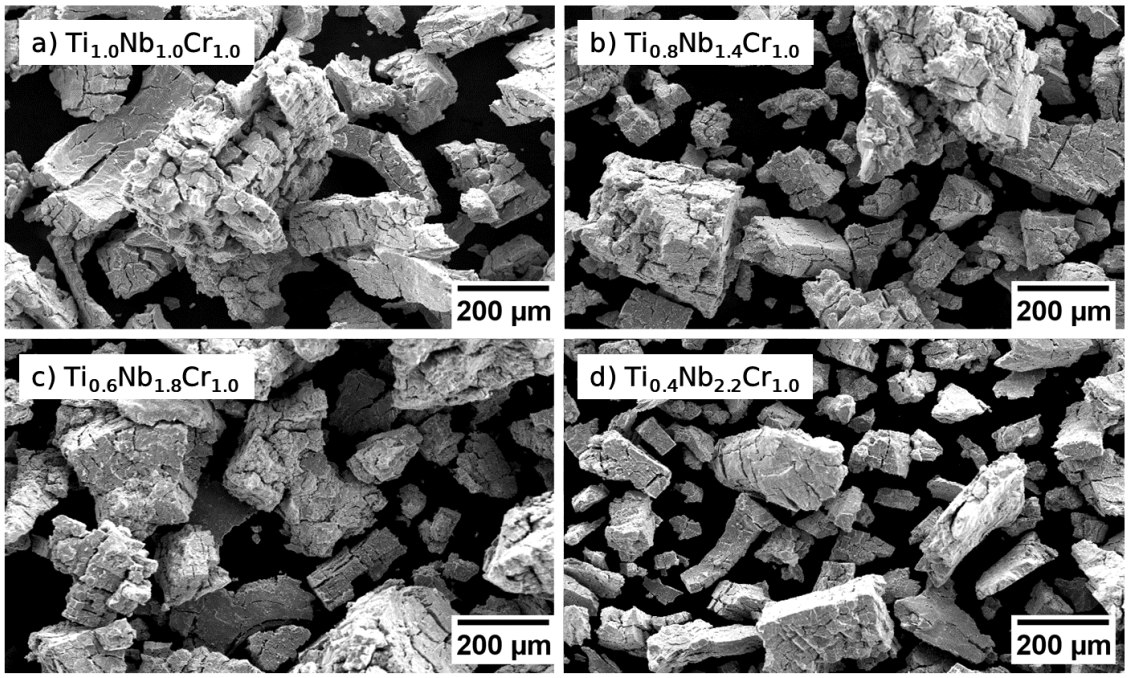

Figure 5.8: SEM-SE images of the hydrogenated a) $Ti_{1.0}Nb_{1.0}Cr_{1.0}$, b) $Ti_{0.8}Nb_{1.4}Cr_{1.0}$, c) $Ti_{0.6}Nb_{1.8}Cr_{1.0}$, and d) $Ti_{0.4}Nb_{2.2}Cr_{1.0}$ alloys.

5.4 Pressure-Composition-Temperature Diagrams

Figure 5.9 illustrates the PCT diagrams of the investigated alloys. Analysis of the PCI curves indicates that all alloys undergo a two-step hydrogen absorption process characterized by two plateau pressures. The lower plateau falls below the detection limit of the pressure transducers (10^{-2} bar), while the higher plateau remains consistently measurable across all temperatures. Furthermore, hysteresis is observed in all alloys, with a magnitude of approximately one order of magnitude, which decreases as temperature rises. This observation is consistent with findings reported by other researchers [34,72].

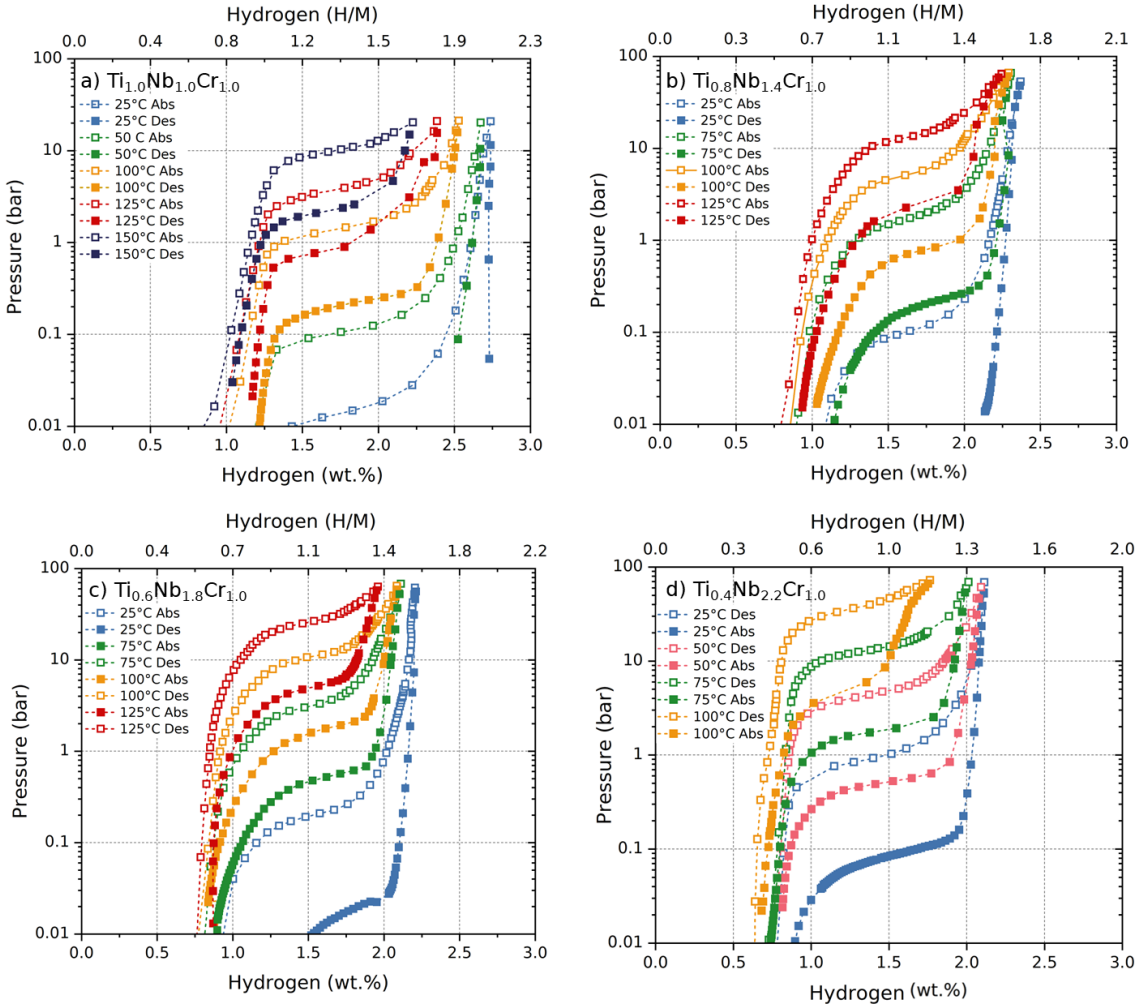

Figure 5.9: Pressure-Composition-Temperature diagrams of the a) $Ti_{1.0}Nb_{1.0}Cr_{1.0}$, b) $Ti_{0.8}Nb_{1.4}Cr_{1.0}$, c) $Ti_{0.6}Nb_{1.8}Cr_{1.0}$, and d) $Ti_{0.4}Nb_{2.2}Cr_{1.0}$ alloys. Hydrogen content in H/M was determined using molar masses derived from the chemical compositions measured via EDX.

The plateau pressure rises with higher Nb content and lower Ti content. At room temperature, the equiatomic alloy shows a plateau pressure close to 0.01 bar during absorption, while the $Ti_{0.4}Nb_{2.2}Cr_{1.0}$ alloy exhibits a plateau around 1 bar. This escalating trend is consistent with predictions from the previously applied thermodynamic model (refer to section 5.1). However, even for the $Ti_{0.4}Nb_{2.2}Cr_{1.0}$ alloy, complete desorption is not attained at any of the four measured temperatures on the PCT diagram due to the high stability of the intermediate BCC hydride. This alloy demonstrates a reversible hydrogen content

at 25 °C close to 1.24 wt.%. Furthermore, the reversible capacities measured at 100 °C for the $Ti_{1.0}Nb_{1.0}Cr_{1.0}$, $Ti_{0.8}Nb_{1.4}Cr_{1.0}$, $Ti_{0.6}Nb_{1.8}Cr_{1.0}$, and $Ti_{0.4}Nb_{2.2}Cr_{1.0}$ alloys were 1.31 wt.%, 1.25 wt.%, 1.25 wt.%, and 1.08 wt.%, respectively.

The plateau pressures, calculated from the thermodynamic model at 25 °C, are detailed in Table 5.3, derived from both the nominal alloy composition and the experimental ones obtained by EDX in the dendritic regions. The table also presents the plateau pressures measured from the PCI curves at the same temperature. Since the experimental plateaus are sloppy, the pressure values listed in the table were selected at 1 H/M for all curves, enabling a comparative analysis.

Moreover, upon analyzing P_{plat} values derived from both nominal and dendritic compositions measured via EDX, it is evident that the nominal values are consistently lower across all alloys. Notably, P_{plat} values obtained from the dendritic composition closely match the experimental absorption and desorption plateaus for $Ti_{1.0}Nb_{1.0}Cr_{1.0}$, $Ti_{0.8}Nb_{1.4}Cr_{1.0}$, and $Ti_{0.6}Nb_{1.8}Cr_{1.0}$ alloys, with a slight overestimation observed for the $Ti_{0.4}Nb_{2.2}Cr_{1.0}$ alloy.

Figure 5.10 shows the resulting plots from Van't Hoff analyses conducted based on the experimental PCT diagrams (Figure 5.9). The ΔS_{plat} and ΔH_{plat} values extracted from the linear equations are compared with those computed from the thermodynamic model in Table 5.3. Remarkably, the experimental ΔH_{plat} in desorption becomes lower with increasing Nb/Ti, indicative of hydride destabilization. For instance, the $Ti_{1.0}Nb_{1.0}Cr_{1.0}$ alloy presents a desorption ΔH_{plat} of 33.4 kJ/mol of H, while the $Ti_{0.4}Nb_{2.2}Cr_{1.0}$ alloy exhibits a value of 27.3 kJ/mol of H. The same trend is observed in the absolute values of the calculated ΔH_{plat}, using both the nominal and dendritic compositions.

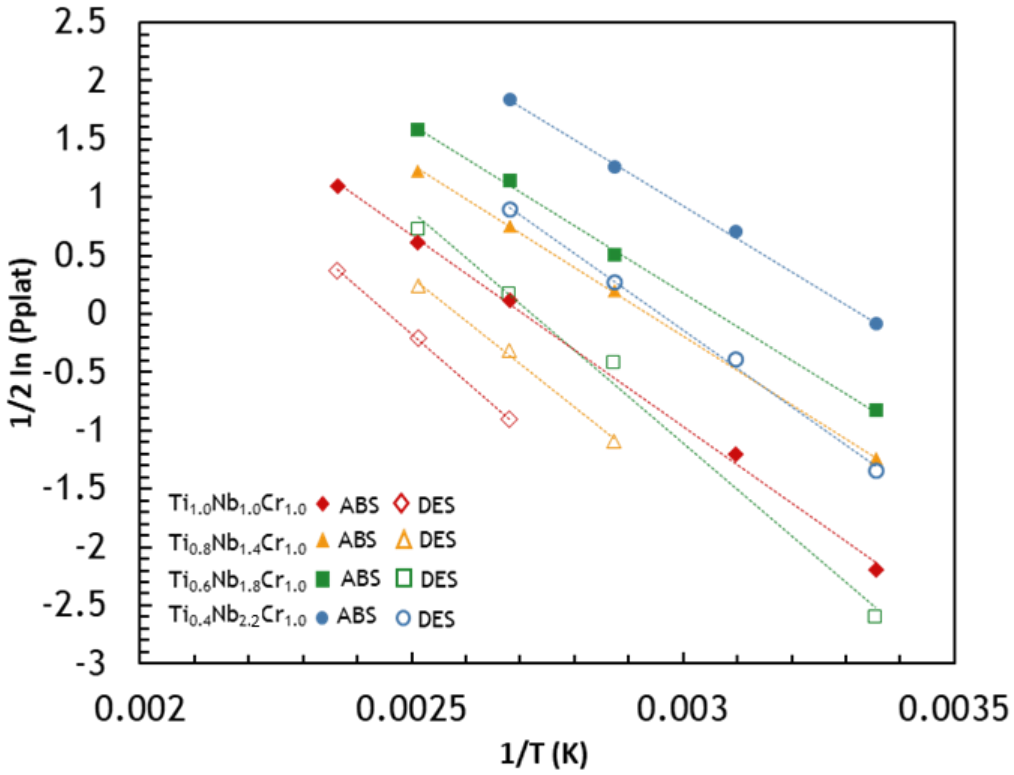

Figure 5.10: Van't Hoff plots of the $Ti_{1.0}Nb_{1.0}Cr_{1.0}$, $Ti_{0.8}Nb_{1.4}Cr_{1.0}$, $Ti_{0.6}Nb_{1.8}Cr_{1.0}$, and $Ti_{0.4}Nb_{2.2}Cr_{1.0}$ alloys.

Several factors influencing the accuracy of the thermodynamic model must be considered to comprehensively understand the discrepancies between experimental and calculated P_{plat}, ΔS_{plat}, and ΔH_{plat} values. Firstly, the model does not account for the hysteresis effect, leading to a single equilibrium plateau pressure. Additionally, since the model was specifically developed for BCC alloys, the presence of secondary phases, such as the C15 Laves phase, is not considered, potentially causing deviations in predictions.

Despite these constraints, the model's high sensitivity to small composition variations becomes evident when comparing results obtained from nominal and EDX compositions. This sensitivity makes the model a powerful tool for predicting the impact of minor compositional changes on calculated properties. Moreover, it effectively predicts trends in plateau pressure and plateau enthalpy variation with composition, greatly facilitating alloy design for diverse applications.

Table 5.3: Experimental and calculated plateau pressures at 25 °C and 1.0 H/M, along with ΔH_{Plat} and ΔS_{Plat} values. Thermodynamic model calculations were conducted using both nominal and dendritic composition measured by EDX, with the results given as absolute values

		Experimental Van't Hoff			**Calculated** Thermodynamic model [24]					
		P_{Plat} 25 °C at 1.0 H/M (bar)	**ΔH_{Plat} (kJ/mol of H)**	**ΔS_{Plat} (J/mol of H)**	**P_{Plat} 25 °C (bar)**		**ΔH_{Plat} (kJ/mol of H)**		**ΔS_{Plat} (J/mol of H)**	
Alloy					**Nominal**	**EDX**	**Nominal**	**EDX**	**Nominal**	**EDX**
$Ti_{1.0}Nb_{1.0}Cr_{1.0}$	Abs	1.0×10^{-2}	-27.3	-73.8	6.0×10^{-3}	1.0×10^{-3}	25.9	28.0	65.1	64.9
	Des	-	33.4	82.2						
$Ti_{0.8}Nb_{1.4}Cr_{1.0}$	Abs	8.0×10^{-2}	-24.3	-71.5	4.3×10^{-2}	5.0×10^{-3}	23.8	28.1	66.7	72.4
	Des	-	30.7	79.3						
$Ti_{0.6}Nb_{1.8}Cr_{1.0}$	Abs	1.9×10^{-1}	-23.9	-73.2	3.1×10^{-1}	7.3×10^{-2}	21.9	25.2	68.6	73.6
	Des	6.0×10^{-3}	33.1	90.1						
$Ti_{0.4}Nb_{2.2}Cr_{1.0}$	Abs	8.4×10^{-1}	-23.5	-78.2	2.4×10^{0}	1.4×10^{0}	20.0	26.9	70.6	91.5
	Des	7.0×10^{-2}	27.3	80.8						

5.5 Thermal Analysis

DSC/TGA/QMS measurements were performed on the hydrogenated alloys to examine the hydrogen desorption events, with results shown in Figure 5.11. The $Ti_{1.0}Nb_{1.0}Cr_{1.0}$, $Ti_{0.8}Nb_{1.4}Cr_{1.0}$, and $Ti_{0.6}Nb_{1.8}Cr_{1.0}$ alloys exhibited two endothermic peaks, while the $Ti_{0.4}Nb_{2.2}Cr_{1.0}$ alloy displayed three distinct peaks. These peaks corresponded to mass losses detected by TGA and H_2 release signals measured by QMS, confirming hydrogen desorption linked to the observed endothermic events.

Comparing the mass losses with the initial hydrogen content in the samples revealed that complete desorption occurred in all cases. Additionally, the distinct peaks represent two steps of hydrogen desorption. The lower temperature peaks likely correspond to the desorption of the FCC hydride (δ-phase) transitioning to the BCC intermediate hydride (β-phase), while the higher temperature peaks indicate the desorption of the β-phase and BCC solid solution (α-phase).

Gaussian peak deconvolutions were performed to facilitate peak analysis, enabling the determination of the respective desorption enthalpies through integration. These deconvolutions were carefully executed to achieve the most precise cumulative fit, incorporating all necessary peaks to accurately describe the DSC signal. The calculated peak areas, measured in J/g, were converted to kJ/mol of H based on the quantity of hydrogen desorbed in each event. The areas and the hydrogen desorbed in each peak are presented in Table 5.4, with the corresponding calculated enthalpies shown in Table 5.5.

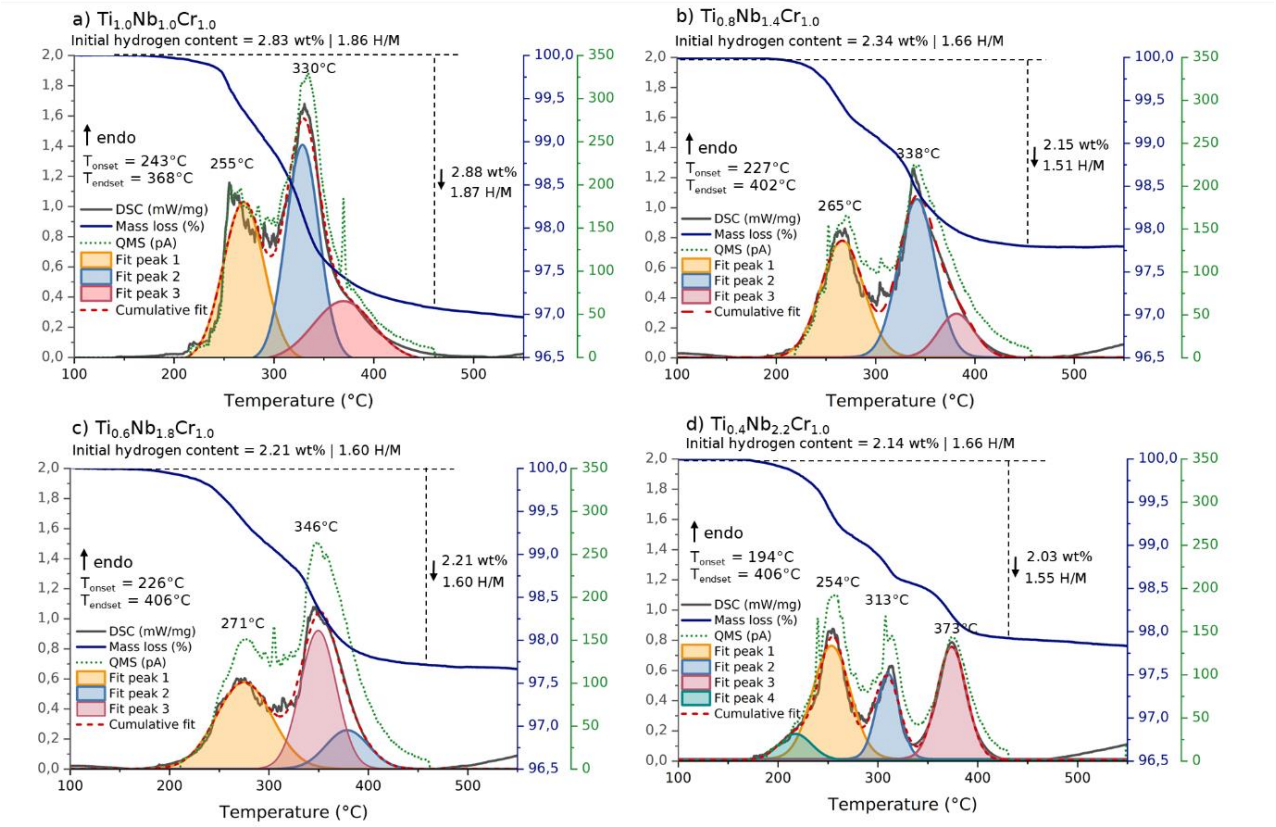

Figure 5.11: DSC/TGA/QMS results of fully hydrogenated a) $Ti_{1.0}Nb_{1.0}Cr_{1.0}$, b) $Ti_{0.8}Nb_{1.4}Cr_{1.0}$, c) $Ti_{0.6}Nb_{1.8}Cr_{1.0}$, and d) $Ti_{0.4}Nb_{2.2}Cr_{1.0}$ alloys.

The enthalpies of the individual peaks revealed that the β→α transition had lower values, indicating greater stabilization of the β-phase. Additionally, the ΔH_{Plat} value in desorption, derived from the Van't Hoff plots (Figure 5.10), corresponds to the δ→β transformation, allowing a comparison with the

enthalpies of the lower temperature peaks measured via DSC, which showed remarkably close values. Finally, the total desorption enthalpies (δ→α) confirm the destabilization of hydrides from the $Ti_{1.0}Nb_{1.0}Cr_{1.0}$ to the $Ti_{0.4}Nb_{2.2}Cr_{1.0}$ alloy, with the latter exhibiting the lower enthalpy.

Table 5.4: Amount of hydrogen desorbed (wt.% and H/M) and peak areas from DSC/TG/QMS measurements of fully and partially hydrogenated $Ti_{1.0}Nb_{1.0}Cr_{1.0}$, $Ti_{0.8}Nb_{1.4}Cr_{1.0}$, $Ti_{0.6}Nb_{1.8}Cr_{1.0}$, and $Ti_{0.4}Nb_{2.2}Cr_{1.0}$ alloys.

	Fully hydrogenated				**Partially hydrogenated**			
	Event *(Fit peaks)*	**Desorption (wt.%)**	**Desorption (H/M)**	**Peak area (J/g)**	**Event** *(Fit peaks)*	**Desorption (wt.%)**	**Desorption (H/M)**	**Peak area (J/g)**
$Ti_{1.0}Nb_{1.0}Cr_{1.0}$	**δ → β** *(1)*	1.19	0.77	321.4	**β → α** *(1+2)*	1.30	0.843	384.5
	β → α *(2+3)*	1.69	1.10	532.6				
	Total	2.88	1.87	854.0	**Total**	1.30	0.843	384.5
$Ti_{0.8}Nb_{1.4}Cr_{1.0}$	**δ → β** *(1)*	0.86	0.60	251.0	**δ → β** *(1)*	0.34	0.24	91.9
	β → α *(2+3)*	1.29	0.91	372.2	**β → α** *(2+3)*	0.70	0.49	263.3
	Total	2.15	1.51	623.2	**Total**	1.04	0.73	355.2
$Ti_{0.6}Nb_{1.8}Cr_{1.0}$	**δ → β** *(1)*	0.98	0.70	242.8	**β → α** *(1+2+3)*		0.64	255.3
	β → α *(2+3)*	1.23	0.88	339.4		0.89		
	Total	2.21	1.58	582.2	**Total**	0.89	0.64	255.3
$Ti_{0.4}Nb_{2.2}Cr_{1.0}$	**δ → β** *(1+2+4)*	1.4	0.71	342.3	**β → α** *(1+2)*	0.74	0.56	197.1
	β → α *(3)*	0.63	0.36	177.5				
	Total	2.03	1.55	519.8	**Total**	0.74	0.56	197.1

Table 5.5: Values of ΔH_{des} δ→β, ΔH_{des} β→α, and ΔH_{des} δ→α obtained from DSC measurements for fully and partially hydrogenated $Ti_{1.0}Nb_{1.0}Cr_{1.0}$, $Ti_{0.8}Nb_{1.4}Cr_{1.0}$, $Ti_{0.6}Nb_{1.8}Cr_{1.0}$, and $Ti_{0.4}Nb_{2.2}Cr_{1.0}$ alloys. The ΔH_{des} δ→β results are compared with those derived from Van't Hoff plots.

	ΔH_{des} δ→β (kJ/mol of H)		**ΔH_{des} β→α (kJ/mol of H)**		**ΔH_{des} δ→α (kJ/mol of H)**
Alloy	**Van't Hoff (Abs/Des)**	**DSC (fully hydrogenated)**	**DSC (fully hydrogenated)**	**DSC (partially hydrogenated)**	**DSC (fully hydrogenated)**
$Ti_{1.0}Nb_{1.0}Cr_{1.0}$	-27.3 / 33.4	27.0	31.5	29.6	29.7
$Ti_{0.8}Nb_{1.4}Cr_{1.0}$	-24.3 / 30.7	29.2	28.9	37.6	29.0
$Ti_{0.6}Nb_{1.8}Cr_{1.0}$	-23.9 / 33.1	24.8	27.6	28.7	26.3
$Ti_{0.4}Nb_{2.2}Cr_{1.0}$	-23.5 / 27.3	24.5	28.2	26.6	25.6

To better understand the β→α desorption event, DSC/TGA/QMS experiments were conducted on partially hydrogenated alloys. The chosen approach involved performing PCI measurements at 25 °C, hydrogenating the alloys while maintaining equilibrium pressures below the β→δ plateau. This would yield in samples mostly composed of β-phase. The XRD patterns of the resulting hydrides are exhibited in Figure 5.12. The two compositions with higher plateau pressures ($Ti_{0.6}Nb_{1.8}Cr_{1.0}$ and $Ti_{0.4}Nb_{2.2}Cr_{1.0}$) presented a BCC phase with larger lattice parameters compared to the as-cast alloys, indicating the presence of only the β-phase along with the C15 Laves Phase. However, both the $Ti_{1.0}Nb_{1.0}Cr_{1.0}$ and $Ti_{0.8}Nb_{1.4}Cr_{1.0}$ alloys displayed a peak corresponding to the FCC phase, in addition to the β-phase and C15 Laves Phase. This is particularly understandable for the equiatomic alloy, given its low plateau pressure (~0.01 bar), which coincides with the detection limit of the equipment.

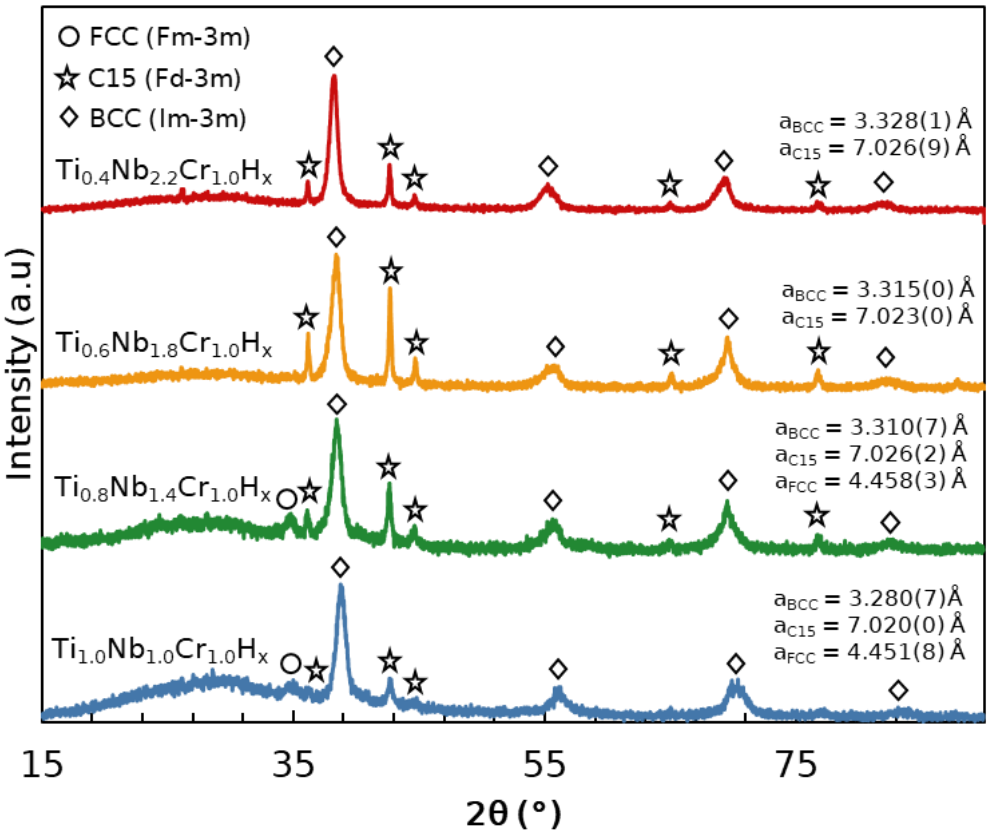

Figure 5.12: Indexed XRD patterns of the partially hydrogenated $Ti_{1.0}Nb_{1.0}Cr_{1.0}$, $Ti_{0.8}Nb_{1.4}Cr_{1.0}$, $Ti_{0.6}Nb_{1.8}Cr_{1.0}$, and $Ti_{0.4}Nb_{2.2}Cr_{1.0}$ alloys.

The DSC/TGA/QMS results for the partially hydrogenated alloys are displayed in Figure 5.13. In the case of the $Ti_{0.6}Nb_{1.8}Cr_{1.0}$ and $Ti_{0.4}Nb_{2.2}Cr_{1.0}$ alloys, which presented only the β-phase along with the C15 Laves Phase, a single endothermic peak, accompanied by corresponding mass losses and H_2 release, was observed. Similar enthalpy values were obtained when compared with those obtained from the higher temperature peaks of the fully hydrogenated alloys. Conversely, distinct results were observed for the two hydrides containing a fraction of δ-phase. The $Ti_{0.8}Nb_{1.4}Cr_{1.0}$ alloy displayed two distinct peaks, while the $Ti_{1.0}Nb_{1.0}Cr_{1.0}$ alloy exhibited a single large peak, potentially resulting from the convolution of two endothermic peaks.

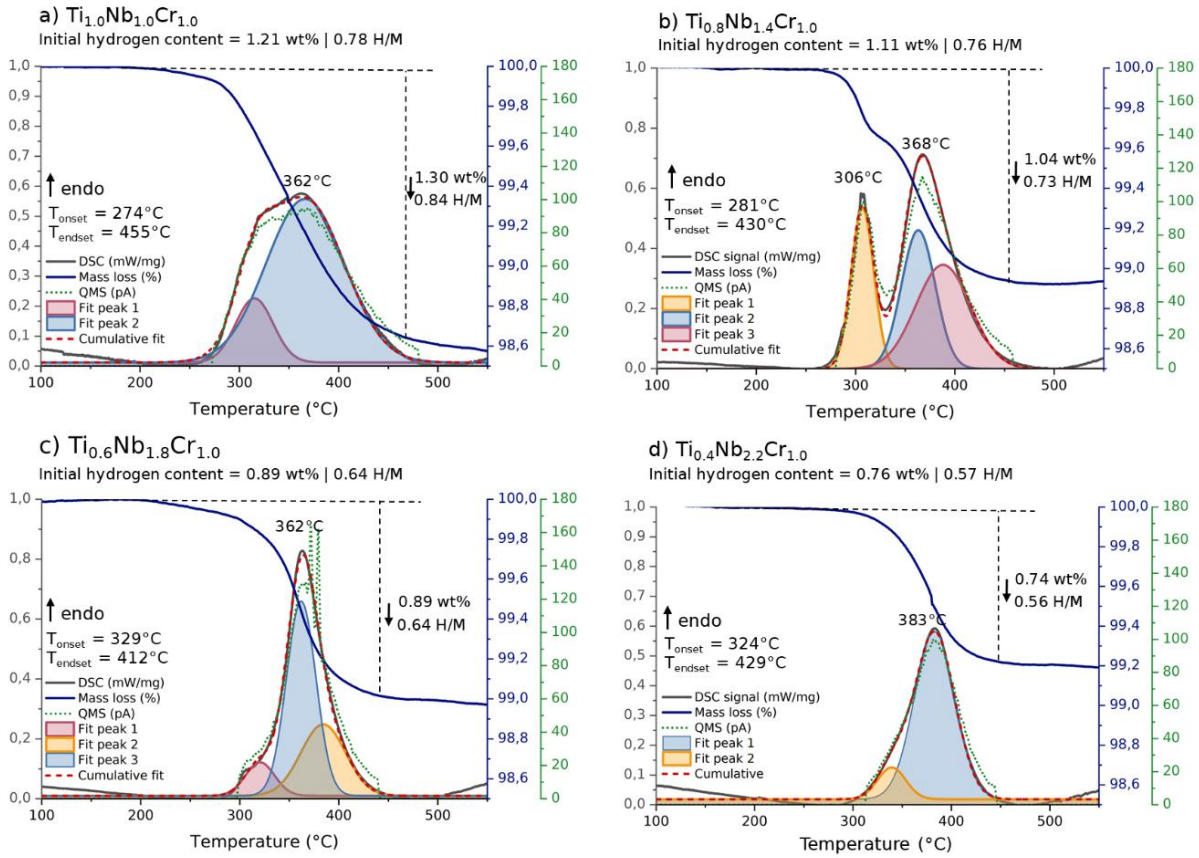

Figure 5.13: DSC/TGA/QMS results of partially hydrogenated a) $Ti_{1.0}Nb_{1.0}Cr_{1.0}$, b) $Ti_{0.8}Nb_{1.4}Cr_{1.0}$, c) $Ti_{0.6}Nb_{1.8}Cr_{1.0}$ and, d) $Ti_{0.4}Nb_{2.2}Cr_{1.0}$ alloy.

These findings indicate that the second endothermic peak observed in the fully hydrogenated $Ti_{0.4}Nb_{2.2}Cr_{1.0}$ alloy upon heating occurs before the β→α desorption, which is accurately described by a single peak in the partially hydrogenated alloy. Calculating the total enthalpy of desorption of the first two peaks of the fully hydrogenated $Ti_{0.4}Nb_{2.2}Cr_{1.0}$ alloy yields a value of 24.5 kJ/mol of H, which is consistent with the value derived from the Van't Hoff plots (27.3 kJ/mol of H). Additionally, the amount of hydrogen desorbed in these two peaks is 1.4 wt.% (1.1 H/M), closely matching the β→δ plateau width in absorption at 25 °C, approximately 1.3 wt.% (1.0 H/M). Therefore, these first two peaks are likely associated with the desorption of the FCC hydride to the BCC intermediate hydride (δ→β).

The reason why this composition exhibits two peaks in this step, while others do not, remains unclear. One possible explanation is that all alloys might exhibit three endothermic peaks upon desorption from the fully hydrogenated state, but the second peak may be convoluted among the other peaks in the $Ti_{1.0}Nb_{1.0}Cr_{1.0}$, $Ti_{0.8}Nb_{1.4}Cr_{1.0}$, and $Ti_{0.6}Nb_{1.8}Cr_{1.0}$ alloys.

The onset temperatures of the first peaks for the fully hydrogenated alloy, as indicated in Figure 5.11, exhibit a slight decrease with an increasing Nb/Ti ratio, reducing from 243 °C for the $Ti_{1.0}Nb_{1.0}Cr_{1.0}$ alloy to 194 °C for the $Ti_{0.4}Nb_{2.2}Cr_{1.0}$ alloy. This trend aligns with the destabilization of the hydrides as the Nb content increases, requiring lower temperatures to initiate hydrogen desorption. However, the interval between the onset and endset temperatures notably widens with the Nb/Ti ratio, expanding from 125 °C for the equiatomic alloy to 212 °C for the $Ti_{0.4}Nb_{2.2}Cr_{1.0}$ alloy.

Thus, it seems that the destabilization of hydrides is more clearly manifested in the desorption enthalpies becoming lower rather than in the reduction of desorption temperatures upon heating. The latter appears to be influenced by factors beyond thermodynamic considerations, such as the kinetics of desorption.

5.6 Hydrogen Absorption/Desorption Cycling

The cycling performance of the $Ti_{1.0}Nb_{1.0}Cr_{1.0}$, $Ti_{0.8}Nb_{1.4}Cr_{1.0}$, $Ti_{0.6}Nb_{1.8}Cr_{1.0}$, and $Ti_{0.4}Nb_{2.2}Cr_{1.0}$ alloys was evaluated in ten cycles of hydrogen absorption and desorption and the results are presented in Figure 5.14. For all the cycles, hydrogen absorption was carried out at 25 °C and 30 bar, while desorption took place at 350 °C under dynamic vacuum for 3 hours. Before the first cycle, the samples underwent an activation treatment at 350 °C under dynamic vacuum for 2 hours.

Throughout the cycling process, a consistent decrease in maximum capacity was observed with each successive cycle. In the 10^{th} cycle, the maximum capacities for the $Ti_{1.0}Nb_{1.0}Cr_{1.0}$, $Ti_{0.8}Nb_{1.4}Cr_{1.0}$, $Ti_{0.6}Nb_{1.8}Cr_{1.0}$, and $Ti_{0.4}Nb_{2.2}Cr_{1.0}$ alloys were found to be 0.20 wt.%, 0.16 wt.%, 0.17 wt.%, and 0.26 wt.% lower, respectively, compared to the 1^{st} cycle. Notably, the most significant

decrease occurred between the 1st and 2nd cycles for all three alloys. Additionally, the $Ti_{0.8}Nb_{1.4}Cr_{1.0}$ alloy exhibited unusual behavior, with an increase in absorption capacity observed from the 3rd to the 4th cycle, followed by a significant drop from the 4th to the 5th cycle.

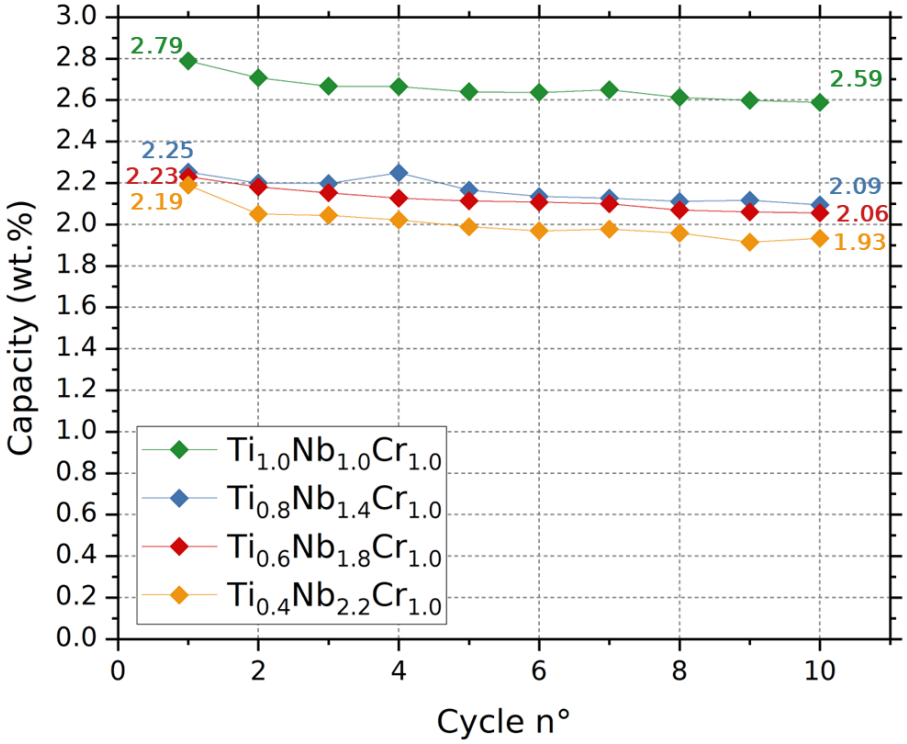

Figure 5.14: Maximum hydrogen absorption capacity (wt.%) of $Ti_{1.0}Nb_{1.0}Cr_{1.0}$, $Ti_{0.8}Nb_{1.4}Cr_{1.0}$, $Ti_{0.6}Nb_{1.8}Cr_{1.0}$, and $Ti_{0.4}Nb_{2.2}Cr_{1.0}$ alloys as a function of the number of hydrogen absorption and desorption cycles.

The drop in maximum capacity observed for the four alloys is similar to the results reported for the $(TiVCr)_{85}Cr_{15}$ [11]. Desorption in each cycle was carried out at 400 °C and under dynamic vacuum, and the maximum capacity decreased from 3.18 to 3.00 wt.%, a drop of 0.18 wt.%, after 10 cycles. Furthermore, the Ti-Nb-Cr and Ti-V-Nb-Cr systems appear to have better cycling performance than certain compositions of the Ti-V-Cr system. Lin et al. [19] reported that the TiVCr alloy's maximum capacity decreased by 1.37 wt.% after 10 cycles, with desorption occurring at 400 °C. Additionally, Kumar et al. [18] reported an improvement in the cycling performance of this system, with the Ti_2CrV showing

a drop of 0.87 wt.% after 10 cycles. Therefore, the cycling performance of the studied alloys within the Ti-Nb-Cr system seems to be comparable to or better than similar systems, although there is room for improvement.

To further understand the capacity loss upon cycling, the $Ti_{0.8}Nb_{1.4}Cr_{1.0}$ alloy was characterized using Synchrotron Radiation Powder X-ray Diffraction (SR-XRD) at the European Synchrotron Radiation Facility (ESRF) in Grenoble, France. Five different conditions were analyzed: as-cast, hydrogenated in the 1st cycle, desorbed in the 1st cycle, hydrogenated in the 10th cycle, and desorbed in the 10th cycle. The diffractograms are presented in Figure 5.15. The Rietveld Refinement results, including lattice parameters, phase concentrations, and microstrain in the predominant phase, are presented in Table 5.6. The crystallite size was consistently maintained at 100 nm in all the refinements, based on Transmission Electron Microscopy (TEM) findings for the hydrogenated $(TiVNb)_{85}Cr_{15}$ alloy [12]. This approach facilitated a qualitative analysis of the microstrain, as both crystallite size and microstrain contribute to peak broadening.

As seen in Figures 5.3 and 5.7, the as-cast $Ti_{0.8}Nb_{1.4}Cr_{1.0}$ alloy exhibits a BCC phase and a fraction of C15 Laves Phase. Upon the first hydrogenation, the BCC phase transforms into an FCC hydride. However, the synchrotron results for the hydrogenated $Ti_{0.8}Nb_{1.4}Cr_{1.0}$ in the first cycle show small intensity peaks corresponding to the BCC phase. These peaks may not have been detected in the diffractogram in Figure 5.3, or some desorption could have occurred in the period between the two measurements, leading to the formation of a fraction of the BCC phase.

Subsequently, desorption to complete the first cycle was performed at 350 °C and under dynamic vacuum for 3 hours. The resulting diffractogram showed that the structure had completely reverted to the BCC phase, with a lattice parameter nearly identical to that of the as-cast alloy. This indicates that the desorption procedure is effective for complete hydrogen removal and was thus adopted for subsequent cycles.

Upon the 10th hydrogenation, the diffractogram shows a predominant BCC phase (65.4 wt.%) along with 18.9 wt.% of FCC phase and 15.7 wt.% of C15

Laves Phase. Two hypotheses can be proposed: extensive hydrogen desorption occurred upon the sample removal from the sample holder, or the BCC phase was largely retained upon cycling. This issue will be further clarified by analyzing the DSC/TGA/QMS measurements on the cycled alloys.

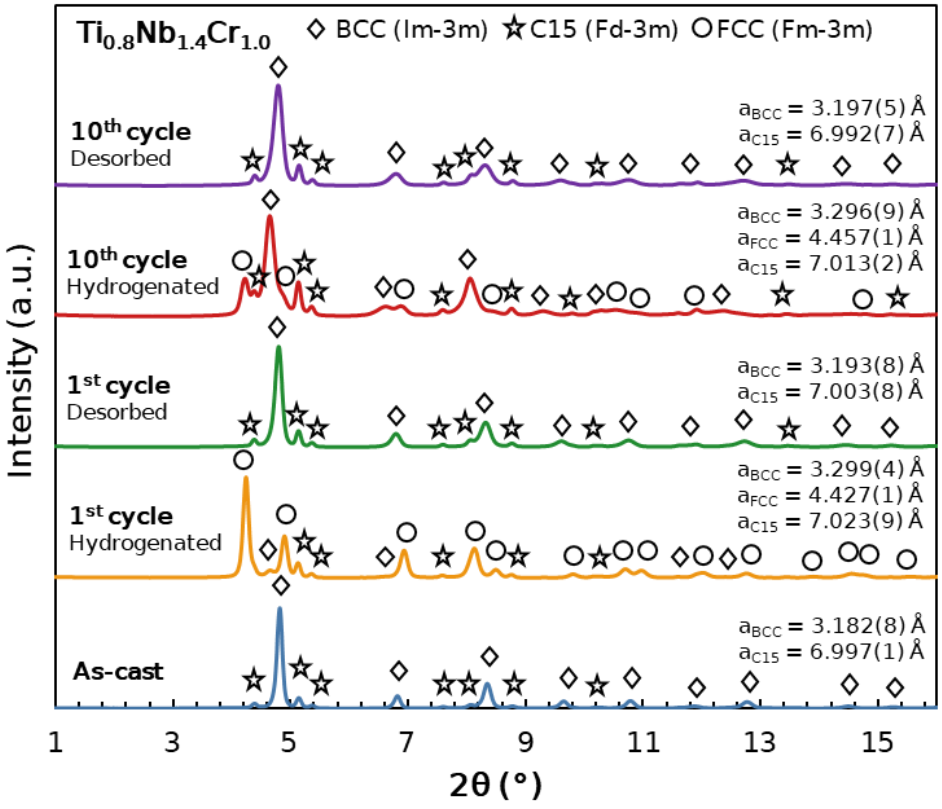

Figure 5.15: SR-XRD results of the $Ti_{0.8}Nb_{1.4}Cr_{1.0}$ alloy in the following conditions: as-cast, hydrogenated in the first cycle, desorbed in the first cycle, hydrogenated in the 10th cycle, and desorbed in the 10th cycle.

The BCC phases present in the hydrogenated states (1st and 10th cycle) exhibit nearly identical lattice parameters of 3.299(4) and 3.296(9) Å, respectively. Using the Peisl relationship [67], the estimated hydrogen content within the BCC phase ranges between 0.64 and 0.92 H/M (0.91 and 1.31 wt.%). Comparing these values with the $Ti_{0.8}Nb_{1.4}Cr_{1.0}$ PCI diagram at 25 °C, in Figure 5.9, they align with the probable end of the first plateau, which is below the detection limit of the equipment. This suggests that the BCC phases in the studied hydrogenated samples are very close to their hydrogen solubility limit.

Table 5.6: Lattice parameters, phase concentrations, and microstrain of the predominant phase obtained via Rietveld Refinement from SR-XRD results of different conditions of the $Ti_{0.8}Nb_{1.4}Cr_{1.0}$ alloy.

	Lattice parameters (Å)			**Phase concentration (wt.%)**			**Microstrain (x 10^3)**
$Ti_{0.8}Nb_{1.4}Cr_{1.0}$	**BCC**	**FCC**	**C15**	**BCC**	**FCC**	**C15**	**Predominant phase**
As-cast	3.182(8)	x	6.997(1)	84.8	x	15.2	3.72
Hydrogenated (1st cycle)	3.299(4)	4.427(1)	7.023(9)	7.0	77.8	15.3	6.62
Desorbed (1st cycle)	3.193(8)	x	7.003(8)	85.3	x	14.7	17.0
Hydrogenated (10th cycle)	3.296(9)	4.457(1)	7.013(2)	65.7	18.4	15.9	37.8
Desorbed (10th cycle)	3.197(5)	x	6.992(7)	86.5	x	13.5	36.2

Completing the 10th cycle, the desorbed alloy returned to the BCC phase with a fraction of the C15 Laves Phase. The lattice parameters remained almost identical to those of the as-cast results. Additionally, peak broadening becomes more pronounced with an increasing number of cycles, especially when comparing the as-cast alloy with the desorbed alloy after the 10th cycle. This characteristic is related to deviations from ideal crystallinity and is attributed to two factors: reduced crystallite size and increased microstrain. Since the crystallite size was considered constant during the Rietveld refinement analyses, the focus will be on the qualitative analysis of the microstrain.

The hydrogen absorption and desorption processes cause the formation of microstrain and defects, such as vacancies and dislocations, in the alloy's structure. This is related to the stresses associated with the BCC↔FCC transformations. Table 5.6 shows that the microstrain in the predominant phase increases with each successive hydrogen absorption and desorption process. The increase in microstrain can be linked to the decrease in absorption capacity, as distortions in the crystal structure and interstices can inhibit hydrogen from entering and exiting the structure [14,48,73,74]. This hypothesis is supported by

the fact that alloys with reduced crystallinity, such as those produced via high-energy ball milling, typically exhibit inferior hydrogen absorption capacities compared to alloys synthesized via arc melting [75,76].

The cycled $Ti_{1.0}Nb_{1.0}Cr_{1.0}$, $Ti_{0.8}Nb_{1.4}Cr_{1.0}$, $Ti_{0.6}Nb_{1.8}Cr_{1.0}$, and $Ti_{0.4}Nb_{2.2}Cr_{1.0}$ alloys were also analyzed through DSC/TGA/QMS measurements. The results are shown in Figure 5.16 and compared to the DSC signal obtained from the non-cycle alloys, previously analyzed in section 5.5, plotted as the orange curves. Following the same procedure of analysis of the non-cycled alloys, Gaussian peak deconvolutions were performed to facilitate peak analysis.

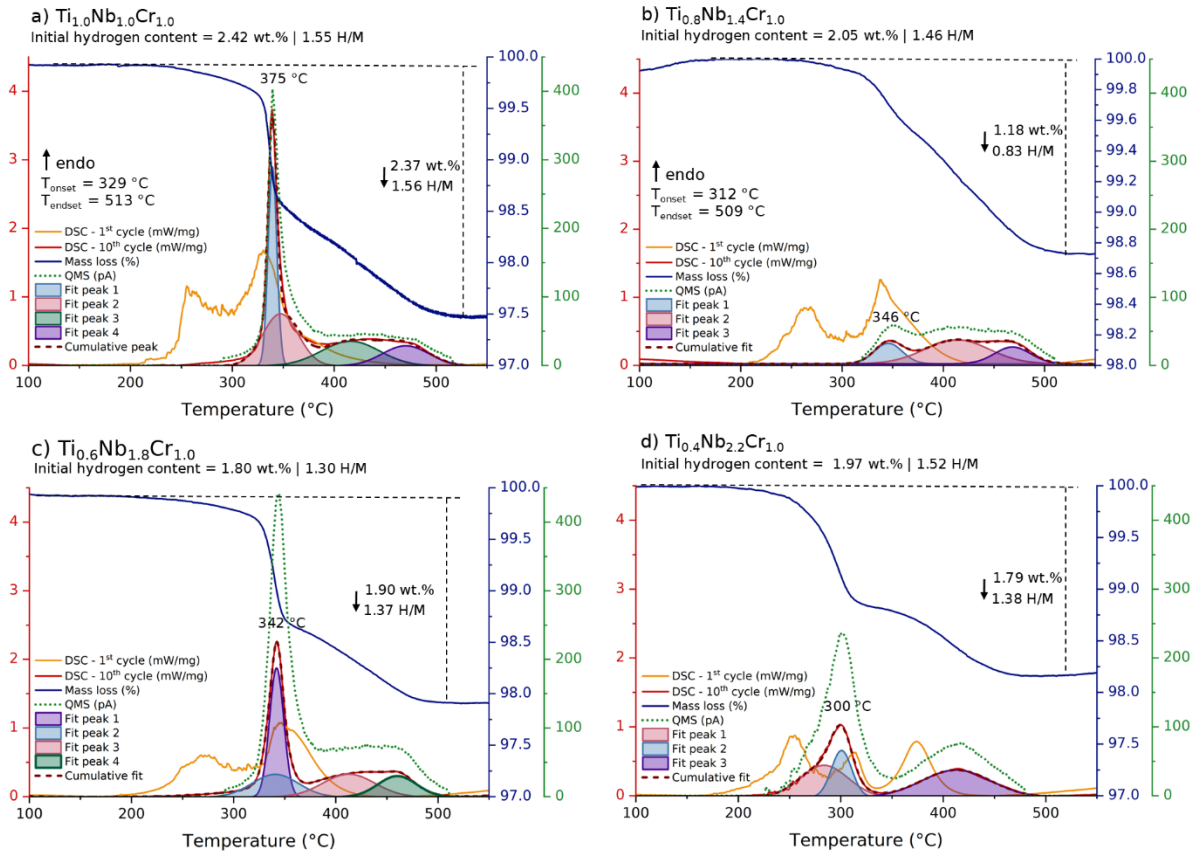

Figure 5.16: DSC/TGA/QMS results of fully hydrogenated a) $Ti_{1.0}Nb_{1.0}Cr_{1.0}$, b) $Ti_{0.8}Nb_{1.4}Cr_{1.0}$, c) $Ti_{0.6}Nb_{1.8}Cr_{1.0}$ and, d) $Ti_{0.4}Nb_{2.2}Cr_{1.0}$ alloys after 10 cycles of absorption and desorption.

Table 5.7 shows the onset (T_{onset}) and endset (T_{endset}) temperatures, and desorption intervals (Δt_{des}) for the non-cycled and cycled alloys. First, the cycled

samples exhibit a shift of the endothermic events to higher temperatures. For all the alloys, the first peaks of the cycle samples appear at nearly the same position as the second peaks of the non-cycled samples. However, the desorption intervals do not show significant differences between the two conditions. Silva et al. [11] reported Thermo Desorption Spectroscopy (TDS) results of the $(TiVNb)_{85}Cr_{15}$ alloy after the 1st and 20th cycle and showed that the desorption events are shifted to higher temperatures upon cycling.

Table 5.7: Onset (T_{onset}) and endset (T_{endset}) temperatures, and desorption intervals (Δt_{des}) in °C for the non-cycled and cycled $Ti_{1.0}Nb_{1.0}Cr_{1.0}$, $Ti_{0.8}Nb_{1.4}Cr_{1.0}$, $Ti_{0.6}Nb_{1.8}Cr_{1.0}$, and $Ti_{0.4}Nb_{2.2}Cr_{1.0}$ alloys.

	Non-cycled			**Cycled**		
	T_{onset} (°C)	**T_{endset} (°C)**	**Δt_{des} (°C)**	**T_{onset} (°C)**	**T_{endset} (°C)**	**Δt_{des} (°C)**
$Ti_{1.0}Nb_{1.0}Cr_{1.0}$	243	368	125	329	513	184
$Ti_{0.8}Nb_{1.4}Cr_{1.0}$	227	402	175	312	509	197
$Ti_{0.6}Nb_{1.8}Cr_{1.0}$	226	406	180	324	497	173
$Ti_{0.4}Nb_{2.2}Cr_{1.0}$	194	406	212	260	483	223

Furthermore, all the alloys presented two endothermic peaks with distinct characteristics. For the $Ti_{1.0}Nb_{1.0}Cr_{1.0}$ and $Ti_{0.6}Nb_{1.8}Cr_{1.0}$ alloys, the first peak is significantly more intense and narrower than the second peak, which is very broad and easily deconvoluted into two separate peaks. On the other hand, the $Ti_{0.8}Nb_{1.4}Cr_{1.0}$ and $Ti_{0.4}Nb_{2.2}Cr_{1.0}$ alloys exhibit both broad endothermic peaks, especially the $Ti_{0.8}Nb_{1.4}Cr_{1.0}$ alloy. Notably, unlike the non-cycled $Ti_{0.4}Nb_{2.2}Cr_{1.0}$ alloy, which presents three endothermic events, the cycled state exhibits only two peaks.

Analyzing the amount of hydrogen desorbed measured through TGA, it is evident that the $Ti_{1.0}Nb_{1.0}Cr_{1.0}$, $Ti_{0.6}Nb_{1.8}Cr_{1.0}$, and $Ti_{0.4}Nb_{2.2}Cr_{1.0}$ alloys desorbed an amount close to the initial hydrogen content, according to the values presented at the top of each graph in Figure 5.16. However, the $Ti_{0.8}Nb_{1.4}Cr_{1.0}$ desorbed approximately half of its initial content, indicating that significant desorption occurred before the experiment. This can be attributed to the fact that this sample was the first to have its cyclability measurement concluded and was stored for a

significantly longer period at atmospheric pressure and room temperature before the DSC measurements compared to the other alloys.

The DSC/TG/QMS results of the cycled $Ti_{0.8}Nb_{1.4}Cr_{1.0}$ alloy provide insights into the SR-XRD results for the cycled hydrogenated sample. Significant hydrogen desorption occurred, leading to the formation of the BCC phase with hydrogen content close to its solubility limit. Furthermore, considering that the hydrogenated $Ti_{0.8}Nb_{1.4}Cr_{1.0}$ alloy in the 1st cycle doesn't exhibit desorption as significant as the cycled state - presenting only 5 wt.% of BCC phase and DSC with desorbed amount close to the initial content (Figure 5.12) - and that this sample was stored for a significantly longer time than the cycled one, it can be inferred that the FCC phase (δ-phase) was destabilized during the cycling process, making it easier to desorb from the FCC to the BCC phase (β-phase).

The enthalpies of desorption (ΔH_{des}) for the cycled samples were calculated using the same procedure described in section 5.5. The amount of hydrogen desorbed, and the peak areas are shown in Table 5.8, while the calculated enthalpies of desorption are presented in Table 5.9, along with those of the non-cycled alloys for comparison. It was not possible to isolate the δ→β desorption for the $Ti_{0.8}Nb_{1.4}Cr_{1.0}$ alloy, given the low FCC fraction observed in the SR-XRD results for the cycled hydrogenated sample. Therefore, the ΔH_{des} value for the β→α desorption was assumed to be equivalent to that of the δ→α desorption. The destabilization of the δ-phase is indicated by the lower ΔH_{des} δ→β values obtained for the cycled alloys compared to the non-cycled. Conversely, the β-phase appears to be more stable after cycling, as evidenced by the higher ΔH_{des} β→α values.

Table 5.8: Amount of hydrogen desorbed (wt.% and H/M) and peak areas from DSC/TG/QMS measurements of cycled $Ti_{1.0}Nb_{1.0}Cr_{1.0}$, $Ti_{0.8}Nb_{1.4}Cr_{1.0}$, $Ti_{0.6}Nb_{1.8}Cr_{1.0}$, and $Ti_{0.4}Nb_{2.2}Cr_{1.0}$ alloys.

	Event *(Fit peaks)*	**Desorption (wt.%)**	**Desorption (H/M)**	**Peak area (J/g)**
$Ti_{1.0}Nb_{1.0}Cr_{1.0}$	**δ → β** *(1+2)*	1.57	1.02	385.2
	β → α *(3+4)*	0.80	0.52	260.3
	Total	2.37	1.56	645.5
$Ti_{0.8}Nb_{1.4}Cr_{1.0}$	**δ → β** *(1)*	0.43	0.30	62.1
	β → α *(2+3)*	0.75	0.53	335.7
	Total	1.18	0.92	397.8
$Ti_{0.6}Nb_{1.8}Cr_{1.0}$	**δ → β** *(1+2)*	1.29	0.93	311.2
	β → α *(3+4)*	0.61	0.44	216.8
	Total	1.90	1.37	528.0
$Ti_{0.4}Nb_{2.2}Cr_{1.0}$	**δ → β** *(1+2)*	1.16	0.89	265.9
	β → α *(3)*	0.63	0.48	201.8
	Total	1.79	1.38	467.4

Table 5.9: Values of ΔH_{des} δ→β, ΔH_{des} β→α and ΔH_{des} δ→α obtained from DSC for fully hydrogenated $Ti_{1.0}Nb_{1.0}Cr_{1.0}$, $Ti_{0.8}Nb_{1.4}Cr_{1.0}$, $Ti_{0.6}Nb_{1.8}Cr_{1.0}$, and $Ti_{0.4}Nb_{2.2}Cr_{1.0}$ alloys after 1 and 10 cycles of hydrogen absorption/desorption.

	ΔH_{des} δ→β (kJ/mol of H)		**ΔH_{des} β→α (kJ/mol of H)**		**ΔH_{des} δ→α (kJ/mol of H)**	
Alloy	**1st cycle**	**10th cycle**	**1st cycle**	**10th cycle**	**1st cycle**	**10th cycle**
$Ti_{1.0}Nb_{1.0}Cr_{1.0}$	27.0	24.5	31.5	32.5	29.7	27.2
$Ti_{0.8}Nb_{1.4}Cr_{1.0}$	29.2	-	28.9	33.7	29.0	33.7
$Ti_{0.6}Nb_{1.8}Cr_{1.0}$	24.8	24.1	27.6	35.5	26.3	27.8
$Ti_{0.4}Nb_{2.2}Cr_{1.0}$	24.5	22.9	28.2	32.0	25.6	26.1

The destabilization of the δ-phase can be linked to the decrease in hysteresis magnitude upon cycling, a phenomenon previously reported in BCC solid solution alloys [77,78]. Esayed and Northwood [78] reported that in V-Nb alloys, the desorption plateau increased and the absorption plateau decreased with the number of cycles, reducing the hysteresis magnitude. Therefore, it is

plausible that a similar phenomenon occured in the alloys analyzed in this study, where the FCC hydride (δ-phase) more easily transforms into the BCC hydride (β-phase) after 10 cycles due to the increase in the desorption plateau.

Conversely, the stabilization of the β-phase may be associated with the introduction of defects and microstrain during cycling. Wang et al. [79] and Norskov et al. [80] discussed that interstitial hydrogen atoms are trapped by lattice defects, particularly by voids and vacancies. This trapping would lead to more endothermic desorption from the β- to the α-, as indicated by higher ΔH_{des} β→α values after 10 cycles. However, to fully understand the mechanisms behind the β-phase stabilization and δ-phase destabilization upon cycling, more detailed analyses are required.

6 CONCLUSIONS

The Ti-Nb-Cr system was thoroughly investigated with a focus on four specific compositions: $Ti_{1.0}Nb_{1.0}Cr_{1.0,}$ $Ti_{0.8}Nb_{1.4}Cr_{1.0,}$ $Ti_{0.6}Nb_{1.8}Cr_{1.0,}$ and $Ti_{0.4}Nb_{2.2}Cr_{1.0.}$ These specific compositions were designed based on systematic variations in the content of the strong hydride-forming element (Ti) and a weaker hydride-forming element (Nb). The primary objective was to develop hydrides that are less stable and exhibit higher equilibrium pressures as the Nb/Ti ratio increases. For this, trends in equilibrium pressures in the PCI curves were predicted based on these compositional variations using a thermodynamic model, and the CALPHAD method was employed to predict the phases formed in the designed alloys. This study showed how these variations in composition affect phase formation, microstructure, and hydrogen storage properties. The main findings include:

- The alloys, synthesized through arc-melting, exhibited a predominant BCC structure with a minor fraction of the C15 Laves phase. These results suggest that the rapid cooling rate characteristic of the arc melting process effectively retains a significant amount of the high-temperature phase predicted by CALPHAD calculations. Furthermore, all alloys exhibited a clear dendritic microstructure, with chromium microsegregation occurring in the interdendritic regions, linked to the alloys' extensive solidification intervals.
- All alloys demonstrated rapid hydrogen absorption kinetics at room temperature without requiring activation treatment. The absorption capacities for the $Ti_{1.0}Nb_{1.0}Cr_{1.0,}$ $Ti_{0.8}Nb_{1.4}Cr_{1.0,}$ $Ti_{0.6}Nb_{1.8}Cr_{1.0,}$ and $Ti_{0.4}Nb_{2.2}Cr_{1.0}$ alloys were 2.81 wt.%, 2.34 wt.%, 2.20 wt.%, and 2.14 wt.%, respectively. Upon hydrogenation, the alloys formed an FCC hydride alongside the C15 Laves phase. The minor variations in the lattice parameters of the C15 Laves phase suggest that it does not significantly contribute to the hydrogen absorption capacity of the alloys.
- The PCT diagrams revealed that the equilibrium pressures consistently increased with a higher Nb/Ti ratio, ranging from 0.01 bar for the $Ti_{1.0}Nb_{1.0}Cr_{1.0}$ alloy to 1 bar for the $Ti_{0.4}Nb_{2.2}Cr_{1.0}$ alloy. All PCI curves showed significant hysteresis, which diminished as the temperature increased.

Additionally, a two-step hydrogen absorption was suggested, with the first plateau located below the detection limit of the pressure transducers. The thermodynamic model used to calculate the PCI curves was effective in predicting the trend of the equilibrium plateau pressure as the composition changed.

- DSC/TGA/QMS measurements conducted on fully hydrogenated alloys revealed a multi-step hydrogen desorption process. The $Ti_{1.0}Nb_{1.0}Cr_{1.0,}$ $Ti_{0.8}Nb_{1.4}Cr_{1.0,}$ and $Ti_{0.6}Nb_{1.8}Cr_{1.0}$ alloys exhibited two distinct endothermic peaks, while the $Ti_{0.4}Nb_{2.2}Cr_{1.0}$ displayed three endothermic peaks. The lower temperature peaks corresponded to the transition from the δ-phase to the β-phase, and the higher temperature peak was attributed to the desorption from the β-phase to the α-phase. Notably, the total desorption enthalpies became lower as the Nb/Ti ratio increased, ranging from 27.6 kJ/mol of H for the equiatomic alloy to 25.6 kJ/mol of H for the $Ti_{0.4}Nb_{2.2}Cr_{1.0}$ alloy, evidencing a trend toward hydride destabilization.
- The cyclability of the alloys was assessed through 10 cycles of absorption at room temperature and desorption at 350 °C under dynamic vacuum. After 10 cycles, the decrease in capacity was 0.20wt.%, 0.16%wt.%, 0.17 wt.%, and 0.26 wt.% for the $Ti_{1.0}Nb_{1.0}Cr_{1.0,}$ $Ti_{0.8}Nb_{1.4}Cr_{1.0,}$ $Ti_{0.6}Nb_{1.8}Cr_{1.0,}$ and $Ti_{0.4}Nb_{2.2}Cr_{1.0}$ alloys, respectively. SR-XRD analyses of different conditions of the $Ti_{0.8}Nb_{1.4}Cr_{1.0}$ alloy indicated destabilization of the FCC hydride during cycling. Significant peak broadening was observed, attributed to increased microstrain caused by the hydrogen absorption and desorption cycles. Additionally, DSC/TGA/QMS experiments on the cycled alloys revealed a shift of desorption peaks to higher temperatures due to cycling, The enthalpies of desorption indicated a destabilization of the FCC hydride (δ-phase) and stabilization of the BCC intermediate hydride (β-phase) over cycles.

In summary, this study advanced the understanding of the Ti-Nb-Cr system's key properties for hydrogen storage and provided a foundation for optimizing its thermodynamic characteristics. Through strategic adjustments in composition, this work successfully demonstrated hydride destabilization, designing alloys with increased desorption plateau pressures that better meet practical application requirements.

7 SUGGESTION FOR FUTURE WORKS

- Exploration of compositions within the Ti-Nb-Cr system with reversibility at room temperature, taking advantage of the observed destabilization trend by increasing the Nb/Ti ratio.
- Detailed examination of the influence of the C15 Laves Phase on the Ti-Nb-Cr system, understanding the implications of increasing its fraction upon compositional adjustments.
- Measurement of PCI curves upon cycling to track changes in the curves and elucidate the destabilization of the FCC hydride with increasing cycles.
- Investigation on cycled alloys aiming at understanding the reason behind the shift of endothermic desorption events to higher temperatures over cycling.

8 REFERENCES

[1] M.A. Rosen, S. Koohi-Fayegh, The prospects for hydrogen as an energy carrier: an overview of hydrogen energy and hydrogen energy systems, Energy Ecol Environ 1 (2016) 10–29. https://doi.org/10.1007/s40974-016-0005-z.

[2] Y. Vasconcelos, Na rota do hidrogênio sustentável, Revista Pesquisa FAPESP (2023).

[3] A. Züttel, A. Borgschulte, L. Schlapbach, Hydrogen as a Future Energy Carrier, Wiley-VCH, 2007.

[4] A. León, ed., Hydrogen Technology: Mobile and Portable Applications, 1st ed., Springer Berlin, Heidelberg, 2008. https://doi.org/https://doi.org/10.1007/978-3-540-69925-5.

[5] A. Züttel, Materials for hydrogen storage, 2003.

[6] U. Eberle, M. Felderhoff, F. Schüth, Chemical and Physical Solutions for Hydrogen Storage, Angewandte Chemie International Edition 48 (2009) 6608–6630. https://doi.org/10.1002/ANIE.200806293.

[7] D.P. Broom, Hydrogen Storage Materials The Characterisation of Their Storage Properties, Springer Verlag, 2011. https://doi.org/10.1007/978-0-85729-221-6.

[8] F. Marques, M. Balcerzak, F. Winkelmann, G. Zepon, M. Felderhoff, Review and outlook on high-entropy alloys for hydrogen storage, Energy Environ Sci 14 (2021) 5191–5227. https://doi.org/10.1039/d1ee01543e.

[9] X.B. Yu, Z. Wu, B.J. Xia, N.X. Xu, Enhancement of hydrogen storage capacity of Ti-V-Cr-Mn BCC phase alloys, J Alloys Compd 372 (2004) 272–277. https://doi.org/10.1016/j.jallcom.2003.09.153.

[10] B. Hessel Silva, W.J. Botta, G. Zepon, Design of a Ti–V–Nb–Cr alloy with room temperature hydrogen absorption/desorption reversibility, Int J Hydrogen Energy (2023). https://doi.org/10.1016/j.ijhydene.2023.05.032.

[11] B.H. Silva, C. Zlotea, Y. Champion, W.J. Botta, G. Zepon, Design of TiVNb-(Cr, Ni or Co) multicomponent alloys with the same valence electron concentration for hydrogen storage, J Alloys Compd 865 (2021). https://doi.org/10.1016/j.jallcom.2021.158767.

[12] B.H. Silva, C. Zlotea, G. Vaughan, Y. Champion, W.J. Botta, G. Zepon, Hydrogen absorption/desorption reactions of the (TiVNb)85Cr15 multicomponent alloy, J Alloys Compd 901 (2022). https://doi.org/10.1016/j.jallcom.2022.163620.

[13] R.B. Strozi, D.R. Leiva, G. Zepon, W.J. Botta, J. Huot, Effects of the chromium content in (Tivnb)100−xcrx body-centered cubic high entropy alloys designed for hydrogen storage applications, Energies (Basel) 14 (2021). https://doi.org/10.3390/en14113068.

[14] R.B. Strozi, B.H. Silva, D.R. Leiva, C. Zlotea, W.J. Botta, G. Zepon, Tuning the hydrogen storage properties of Ti-V-Nb-Cr alloys by controlling the Cr/(TiVNb) ratio, J Alloys Compd 932 (2023). https://doi.org/10.1016/j.jallcom.2022.167609.

[15] M.M. Nygård, G. Ek, D. Karlsson, M.H. Sørby, M. Sahlberg, B.C. Hauback, Counting electrons - A new approach to tailor the hydrogen sorption properties of high-entropy alloys, Acta Mater 175 (2019) 121–129. https://doi.org/10.1016/j.actamat.2019.06.002.

[16] M. Okada, T. Kuriiwa, T. Tamura, H. Takamura, A. Kamegawa, Ti-V-Cr b.c.c. alloys with high protium content, J Alloys Compd 330–332 (2002) 511–516. https://doi.org/10.1016/S0925-8388(01)01647-4.

[17] S.W. Cho, G. Shim, G.S. Choi, C.N. Park, J.H. Yoo, J. Choi, Hydrogen absorption–desorption properties of Ti0.32Cr0.43V0.25 alloy, J Alloys Compd 430 (2007) 136–141. https://doi.org/10.1016/J.JALLCOM.2006.04.068.

[18] A. Kumar, K. Shashikala, S. Banerjee, J. Nuwad, P. Das, C.G.S. Pillai, Effect of cycling on hydrogen storage properties of Ti 2CrV alloy, Int J Hydrogen Energy 37 (2012) 3677–3682. https://doi.org/10.1016/j.ijhydene.2011.04.135.

[19] H.C. Lin, K.M. Lin, K.C. Wu, H.H. Hsiung, H.K. Tsai, Cyclic hydrogen absorption-desorption characteristics of TiCrV and Ti0.8 Cr1.2 V alloys, Int J Hydrogen Energy 32 (2007) 4966–4972. https://doi.org/10.1016/j.ijhydene.2007.07.057.

[20] H. Kwon, J.H. Yoo, K.M. Roh, C.Y. Suh, W.B. Kim, S.W. Cho, Effect of particle size and microstructure on the hydrogen storage property in a V-Ti-Cr solid solution system, J Alloys Compd 535 (2012) 87–90. https://doi.org/10.1016/j.jallcom.2012.04.078.

[21] X.B. Yu, J.Z. Chen, Z. Wu, B.J. Xia, N.X. Xu, Effect of Cr content on hydrogen storage properties for Ti-V-based BCC-phase alloys, Int J Hydrogen Energy 29 (2004) 1377–1381. https://doi.org/10.1016/j.ijhydene.2004.01.015.

[22] S. Cho, C. Han, C. Park, E. Akiba, The hydrogen storage characteristics of Ti–Cr–V alloys, J Alloys Compd 288 (1999) 294–298. https://doi.org/https://doi.org/10.1016/S0925-8388(99)00096-1.

[23] M. Aoki, T. Noritake, A. Ito, M. Ishikiriyama, S.I. Towata, Improvement of cyclic durability of Ti-Cr-V alloy by Fe substitution, Int J Hydrogen Energy 36 (2011) 12329–12332. https://doi.org/10.1016/j.ijhydene.2011.07.019.

[24] S.I. Towata, T. Noritake, A. Itoh, M. Aoki, K. Miwa, Cycle durability of Ti-Cr-V alloys partially substituted by Nb or Fe, J Alloys Compd 580 (2013) S226–S228. https://doi.org/10.1016/j.jallcom.2013.03.163.

[25] T. Kabutomori, H. Takeda, Y. Wakisaka, K. Ohnishi, Hydrogen absorption properties of TiCrA (A ≡ V, Mo or other transition metal) B.C.C. solid solution alloys, J Alloys Compd 231 (1995) 528–532. https://doi.org/10.1016/0925-8388(95)01859-X.

[26] K. Sakaki, H. Kim, K. Asano, Y. Nakamura, Hydrogen storage properties of Nb-based solid solution alloys with a BCC structure, J Alloys Compd 820 (2020) 153399. https://doi.org/10.1016/j.jallcom.2019.153399.

[27] U.S. DRIVE Partnership, Target Explanation Document: Onboard Hydrogen Storage for Light-Duty Fuel Cell Vehicles, (2017). www.uscar.org (accessed January 25, 2024).

[28] R. Griessen, T. Riesterer, Heat of formation models, in: Hydrogen in Intermetallic Compounds I, Springer, Berlin, Heidelberg, 1988: pp. 219–284. https://doi.org/10.1007/3540183337_13.

[29] Y. Fukai, The Metal-Hydrogen System: Basic Bulk Properties, 2nd ed., Springer Berlin Heidelberg, Berlin, Heidelberg, 2005. https://doi.org/10.1007/3-540-28883-X.

[30] G. Zepon, B.H. Silva, C. Zlotea, W.J. Botta, Y. Champion, Thermodynamic modelling of hydrogen-multicomponent alloy systems: Calculating pressure-composition-temperature diagrams, Acta Mater 215 (2021). https://doi.org/10.1016/j.actamat.2021.117070.

[31] T.B. Flanagan, W.A. Oates, Some thermodynamic aspects of metal hydrogen systems, J Alloys Compd 404 (2005) 16–23. https://doi.org/10.1016/j.jallcom.2004.11.108.

[32] M.G. Shelyapina, Metal hydrides for energy storage, in: Handbook of Ecomaterials, Springer International Publishing, 2019: pp. 775–810. https://doi.org/10.1007/978-3-319-68255-6_119.

[33] T.B. Flanagan, J.D. Clewley, Hysteresis in metal hydrides, Journal of the Less-Common Metals 83 (1982) 127–141. https://doi.org/https://doi.org/10.1016/0022-5088(82)90176-X.

[34] S. Qian, D.O. Northwood, Hysteresis in metal-hydrogen systems: a critical review of the experimental observations and theoretical models, Int J Hydrogen Energy 13 (1988) 25–35. https://doi.org/https://doi.org/10.1016/0360-3199(88)90006-7.

[35] H.E. Flotow, H.R. Lohr, B.M. Abraham, D.W. Osborne, The Heat Capacity and Thermodynamic Functions of β-Uranium Hydride from 5 to 350°K.1, 2, J Am Chem Soc 81 (1959) 3529–3533. https://doi.org/10.1021/JA01523A011.

[36] H.K. Birnbaum, M.L. Grossbecr, M. Amano, Hydride precipitation in Nb and some properties of NbH, Journal of the Less-Common Metals 49 (1976) 357. https://doi.org/https://doi.org/10.1016/0022-5088(76)90048-5.

[37] Q. Lai, Y. Sun, T. Wang, P. Modi, C. Cazorla, U.B. Demirci, J.R. Ares Fernandez, F. Leardini, K.F. Aguey-Zinsou, How to Design Hydrogen Storage Materials? Fundamentals, Synthesis, and Storage Tanks, Adv Sustain Syst 3 (2019) 1–64. https://doi.org/10.1002/adsu.201900043.

[38] C.N. Park, S. Luo, T.B. Flanagan, Analysis of sloping plateaux in alloys and intermetallic hydrides I. Diagnostic features, J Alloys Compd 384 (2004) 203–207. https://doi.org/10.1016/j.jallcom.2004.04.101.

[39] C. Zhang, Y. Wu, L. You, X. Cao, Z. Lu, X. Song, Investigation on the activation mechanism of hydrogen absorption in TiZrNbTa high entropy alloy, J Alloys Compd 781 (2019) 613–620. https://doi.org/10.1016/j.jallcom.2018.12.120.

[40] T.B. Flanagan, I.S. Chung, THE THE~ODYN~ICS OF HYSTERESIS FOR HIGH PR~SS~RE METAL HYDRIDES, Journal of the Less-Common Metals 125 (1986) 241–260.

[41] H.K. Birnbaum, M.L. Grossbecr, M. Amano, Hydride precipitation in Nb and some properties of NbH, Journal of the Less Common Metals 49 (1976) 357–370. https://doi.org/10.1016/0022-5088(76)90048-5.

[42] M. Dornheim, M. Dornheim, Thermodynamics of Metal Hydrides: Tailoring Reaction Enthalpies of Hydrogen Storage Materials, Thermodynamics - Interaction Studies - Solids, Liquids and Gases (2011). https://doi.org/10.5772/21662.

[43] K. Young, M.A. Fetcenko, T. Ouchi, J. Im, S.R. Ovshinsky, F. Li, M. Reinhout, S. Township, Hydrogen Storage Materials Having Excellent Kinetics, Capacity. and Cycle Stability, 2 (2008).

[44] S. Selvaraj, A. Jain, S. Kumar, T. Zhang, S. Isobe, H. Miyaoka, Y. Kojima, T. Ichikawa, Study of cyclic performance of V-Ti-Cr alloys employed for hydrogen compressor, Int J Hydrogen Energy 43 (2018) 2881–2889. https://doi.org/10.1016/j.ijhydene.2017.12.159.

[45] P.D. Goodell, Stability of rechargeable hydriding alloys during extended cycling, Journal of The Less-Common Metals 99 (1984) 1–14. https://doi.org/10.1016/0022-5088(84)90330-8.

[46] P. Dantzer, Metal-Hydride technology: A critical review, Hydrogen in Metals III 73 (2007) 279–340. https://doi.org/10.1007/bfb0103405.

[47] C. Wu, Q. Wang, Y. Mao, L. Huang, ScienceDirect Relationship between lattice defects and phase transformation in hydrogenation / dehydrogenation process of the V 60 Ti 25 Cr 3 Fe 12 alloy, Int J Hydrogen

Energy 44 (2019) 9368–9377. https://doi.org/10.1016/j.ijhydene.2019.02.097.

[48] R.B. Strozi, M. Witman, V. Stavila, J. Cizek, K. Sakaki, H. Kim, O. Melikhova, L. Perrière, A. Machida, Y. Nakahira, G. Zepon, W.J. Botta, C. Zlotea, Elucidating Primary Degradation Mechanisms in High-Cycling-Capacity, Compositionally Tunable High-Entropy Hydrides, ACS Appl Mater Interfaces 15 (2023) 38412–38422. https://doi.org/10.1021/ACSAMI.3C05206/SUPPL_FILE/AM3C05206_SI_001.PDF.

[49] N.A.A. Rusman, M. Dahari, A review on the current progress of metal hydrides material for solid-state hydrogen storage applications, Int J Hydrogen Energy 41 (2016) 12108–12126. https://doi.org/10.1016/j.ijhydene.2016.05.244.

[50] E.M. Dematteis, N. Berti, F. Cuevas, M. Latroche, M. Baricco, Substitutional effects in TiFe for hydrogen storage: a comprehensive review, Mater Adv 2 (2021) 2524–2560. https://doi.org/10.1039/D1MA00101A.

[51] A. Lys, J.O. Fadonougbo, M. Faisal, J.Y. Suh, Y.S. Lee, J.H. Shim, J. Park, Y.W. Cho, Enhancing the Hydrogen Storage Properties of AxBy Intermetallic Compounds by Partial Substitution: A Short Review, Hydrogen 2020, Vol. 1, Pages 38-63 1 (2020) 38–63. https://doi.org/10.3390/HYDROGEN1010004.

[52] J.B. Ponsoni, V. Aranda, T. da S. Nascimento, R.B. Strozi, W.J. Botta, G. Zepon, Design of multicomponent alloys with C14 laves phase structure for hydrogen storage assisted by computational thermodynamic, Acta Mater 240 (2022). https://doi.org/10.1016/j.actamat.2022.118317.

[53] J.B. Ponsoni, M. Balcerzak, W.J. Botta, M. Felderhoff, G. Zepon, A comprehensive investigation of the (Ti0.5Zr0.5)1(Fe0.33Mn0.33Cr0.33)2 multicomponent alloy for room-temperature hydrogen storage designed by computational thermodynamic tools, J Mater Chem A Mater (2023). https://doi.org/10.1039/d3ta02197a.

[54] C. Zlotea, M.A. Sow, G. Ek, J.P. Couzinié, L. Perrière, I. Guillot, J. Bourgon, K.T. Møller, T.R. Jensen, E. Akiba, M. Sahlberg, Hydrogen sorption in TiZrNbHfTa high entropy alloy, J Alloys Compd 775 (2019) 667–674. https://doi.org/10.1016/j.jallcom.2018.10.108.

[55] K. Sapru, Z. Tan, M. Bazzi, S. Ramachandran, S. Ovshinksy, High capacity transition metal based hydrogen storage materials for the reversible storage of hydrogen, 2003.

[56] B. Huang, S.R. Ovshinsky, Hydrogen Storage Alloys Providing for the Reversible Storage of Hydrogen At Low Temperatures, 2 (2006).

[57] O.A. Pedroso, W.J. Botta, G. Zepon, An open-source code to calculate pressure-composition-temperature diagrams of multicomponent alloys for hydrogen storage, Int J Hydrogen Energy 47 (2022) 32582–32593. https://doi.org/10.1016/j.ijhydene.2022.07.179.

[58] J. Garcés, The configurational entropy of mixing of interstitials solid solutions, Appl Phys Lett 96 (2010). https://doi.org/10.1063/1.3400221/118971.

[59] E.P. George, D. Raabe, R.O. Ritchie, High-entropy alloys, Nature Reviews Materials 2019 4:8 4 (2019) 515–534. https://doi.org/10.1038/s41578-019-0121-4.

[60] B. Hessel Silva, W.J. Botta, G. Zepon, Design of a Ti–V–Nb–Cr alloy with room temperature hydrogen absorption/desorption reversibility, Int J Hydrogen Energy (2023). https://doi.org/10.1016/j.ijhydene.2023.05.032.

[61] A. Ghosh, Segregation in cast products, n.d.

[62] X. Yu, W. Zhu, F. Li, B. Xia, N. Xu, Body-centered-cubic phase hydrogen storage alloy with improved capacity and fast activation, Volume 84, Issue 16, Pages 3199 - 3201 84 (2004) 3199–3201. https://doi.org/10.1063/1.1712021.

[63] L. Liu, L. Chen, X. Xiao, C. Xu, J. Sun, S. Li, H. Ge, L. Jiang, Influence of annealing treatment on the microstructure and hydrogen storage performance of Ti1.02Cr1.1Mn0.3Fe0.6 alloy for hybrid hydrogen storage application, J Alloys Compd 636 (2015) 117–123. https://doi.org/10.1016/J.JALLCOM.2015.02.138.

[64] Z. Dehouche, M. Savard, F. Laurencelle, J. Goyette, Ti–V–Mn based alloys for hydrogen compression system, J Alloys Compd 400 (2005) 276–280. https://doi.org/10.1016/J.JALLCOM.2005.04.007.

[65] H. Arashima, F. Takahashi, T. Ebisawa, H. Itoh, T. Kabutomori, Correlation between hydrogen absorption properties and homogeneity of Ti–Cr–V alloys, J Alloys Compd 356–357 (2003) 405–408. https://doi.org/10.1016/S0925-8388(03)00363-3.

[66] C. Kittel, Introduction to Solid State Physics, 8th ed., John Wiley & Sons, 2004. https://doi.org/https://doi.org/10.1107/S0365110X54000448.

[67] H. Peisl, Lattice Strains due to Hydrogen in Metals, in: Hydrogen in Metals I, Springer, Berlin, Heidelberg, 2005. https://doi.org/https://doi.org/10.1007/3540087052_42.

[68] J.R. Johnson, J.J. Reilly, Reaction of Hydrogen with the Low-Temperature Form (C15) of TiCr2, Inorg. Chem 17 (1978) 3103. https://doi.org/https://doi.org/10.1021/ic50189a027.

[69] J.R. Johnson, J.J. Reilly, F. Reidinger, L.M. Corliss, J.M. Hastings, On the existence of FCC TiCr1.8H5.3, Journal of the Less-Common Metals, 88 (1982) 107–114. https://doi.org/https://doi.org/10.1016/0022-5088(82)90020-0.

[70] V. Charbonnier, H. Enoki, K. Asano, H. Kim, K. Sakaki, Tuning the hydrogenation properties of Ti1+yCr2-xMnx laves phase compounds for high pressure metal-hydride compressors, Int J Hydrogen Energy 46 (2021) 36369–36380. https://doi.org/10.1016/j.ijhydene.2021.08.143.

[71] S. Suda, Hydrogen–Metal Systems: Technological and Engineering Aspects, Encyclopedia of Materials: Science and Technology (2001) 3970–3976. https://doi.org/10.1016/B0-08-043152-6/00698-7.

[72] V. Shitikov, G. Hilscher, H. Stampfl, H. Kirchmayr, Thermodynamics and kinetics of Zr(Fe1−xMnx)2Hx and the storage compound Ti0.8Zr0.2MnCrH3, Journal of the Less-Common Metals 102 (1984) 29–40. https://doi.org/https://doi.org/10.1016/0022-5088(84)90386-2.

[73] C. Wu, X. Zheng, Y. Chen, M. Tao, G. Tong, J. Zhou, Hydrogen storage and cyclic properties of V60Ti (21.4+x)Cr(6.6-x)Fe12 (0 ≤ x ≤ 3) alloys, Int

J Hydrogen Energy 35 (2010) 8130–8135. https://doi.org/10.1016/j.ijhydene.2010.01.017.

[74] A. Bouzidi, E. Elkaim, V. Nassif, C. Zlotea, Effect of Cr/Mn Addition in TiVNb on Hydrogen Sorption Properties: Thermodynamics and Phase Transition Study, Hydrogen (Switzerland) 5 (2024) 123–136. https://doi.org/10.3390/HYDROGEN5010008/S1.

[75] J. Montero, G. Ek, L. Laversenne, V. Nassif, G. Zepon, M. Sahlberg, C. Zlotea, Hydrogen storage properties of the refractory Ti–V–Zr–Nb–Ta multi-principal element alloy, J Alloys Compd 835 (2020) 155376. https://doi.org/10.1016/J.JALLCOM.2020.155376.

[76] B.K. Singh, G. Shim, S.W. Cho, Effects of mechanical milling on hydrogen storage properties of Ti0.32Cr0.43V0.25 alloy, Int J Hydrogen Energy 32 (2007) 4961–4965. https://doi.org/10.1016/J.IJHYDENE.2007.07.010.

[77] T. Kazumi, T. Tamura, A. Kamegawa, H. Takamura, M. Okada, Effect of absorption-desorption cycles on structure and stability of protides in Ti-Cr-V alloys, Mater Trans 43 (2002) 2748–2752. https://doi.org/10.2320/matertrans.43.2748.

[78] A.Y. Esayed, D.O. Northwood, The effect of hydride formation and decomposition cycles on hysteresis in VxNb1−x-H systems, Int J Hydrogen Energy 17 (1992) 211–218. https://doi.org/10.1016/0360-3199(92)90129-K.

[79] Q. Wang, X. Dai, C. Wu, Y. Mao, Y. Chen, X. Cao, Y. Yan, Y. Wang, H. Zhang, Lattice defects and micro-strains in V 60 Ti 25 Cr 3 Fe 12 alloy and in fl uence on the ab / desorption of hydrogen, J Alloys Compd 830 (2020) 154675. https://doi.org/10.1016/j.jallcom.2020.154675.

[80] J.K. Nørskov, F. Besenbacher, Theory of hydrogen interaction with metals, Journal of the Less Common Metals 130 (1987) 475–490. https://doi.org/10.1016/0022-5088(87)90145-7.

APPENDIX A

Rietveld refinements of the XRD patterns

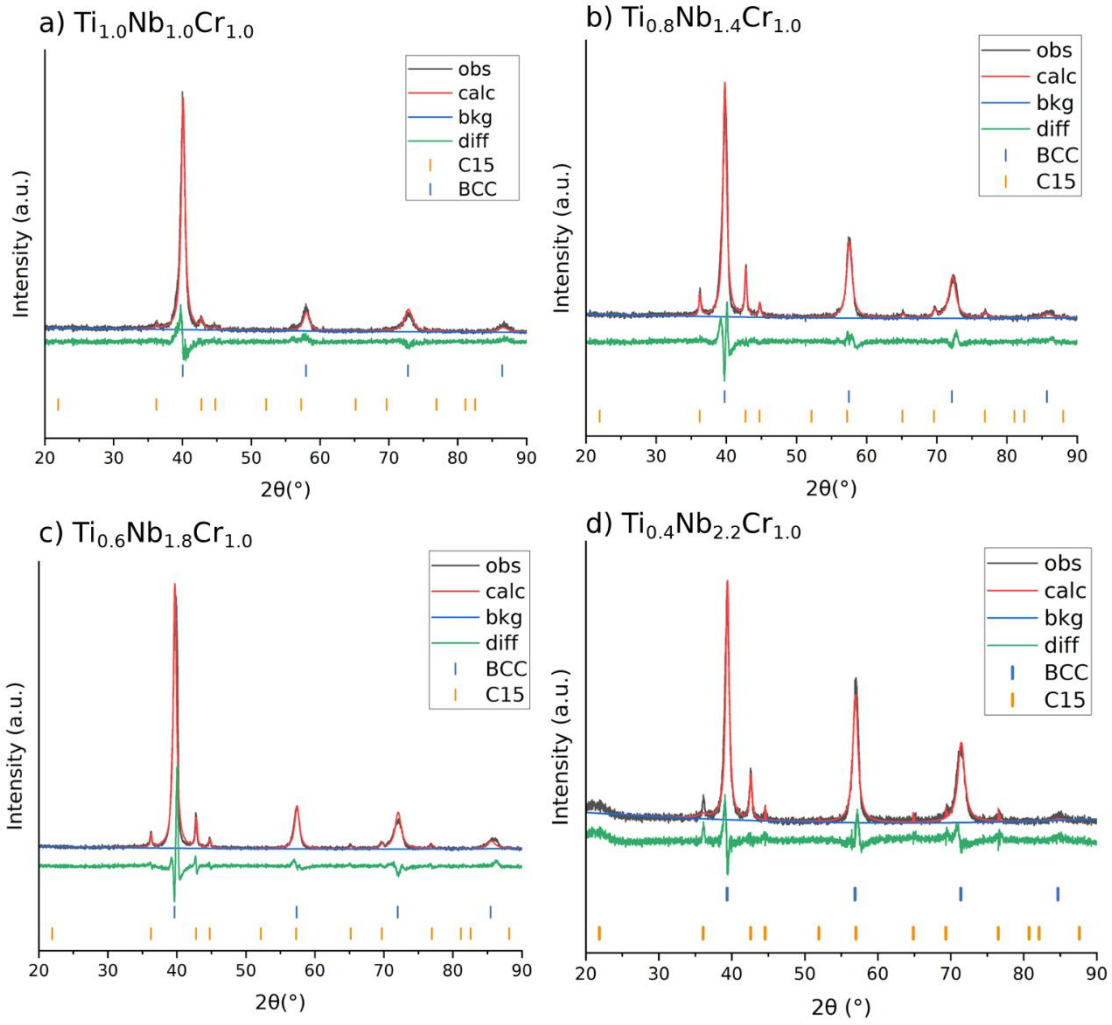

Figure A1: Rietveld refinements of the XRD patterns from the as-cast a) $Ti_{1.0}Nb_{1.0}Cr_{1.0}$, b) $Ti_{0.8}Nb_{1.4}Cr_{1.0}$, c) $Ti_{0.6}Nb_{1.8}Cr_{1.0}$, and d) $Ti_{0.4}Nb_{2.2}Cr_{1.0}$ alloys. The BCC phases were modeled with the compositions measured by EDX and the C15 Laves phase was modeled with a (Ti, Nb)Cr_2 composition.

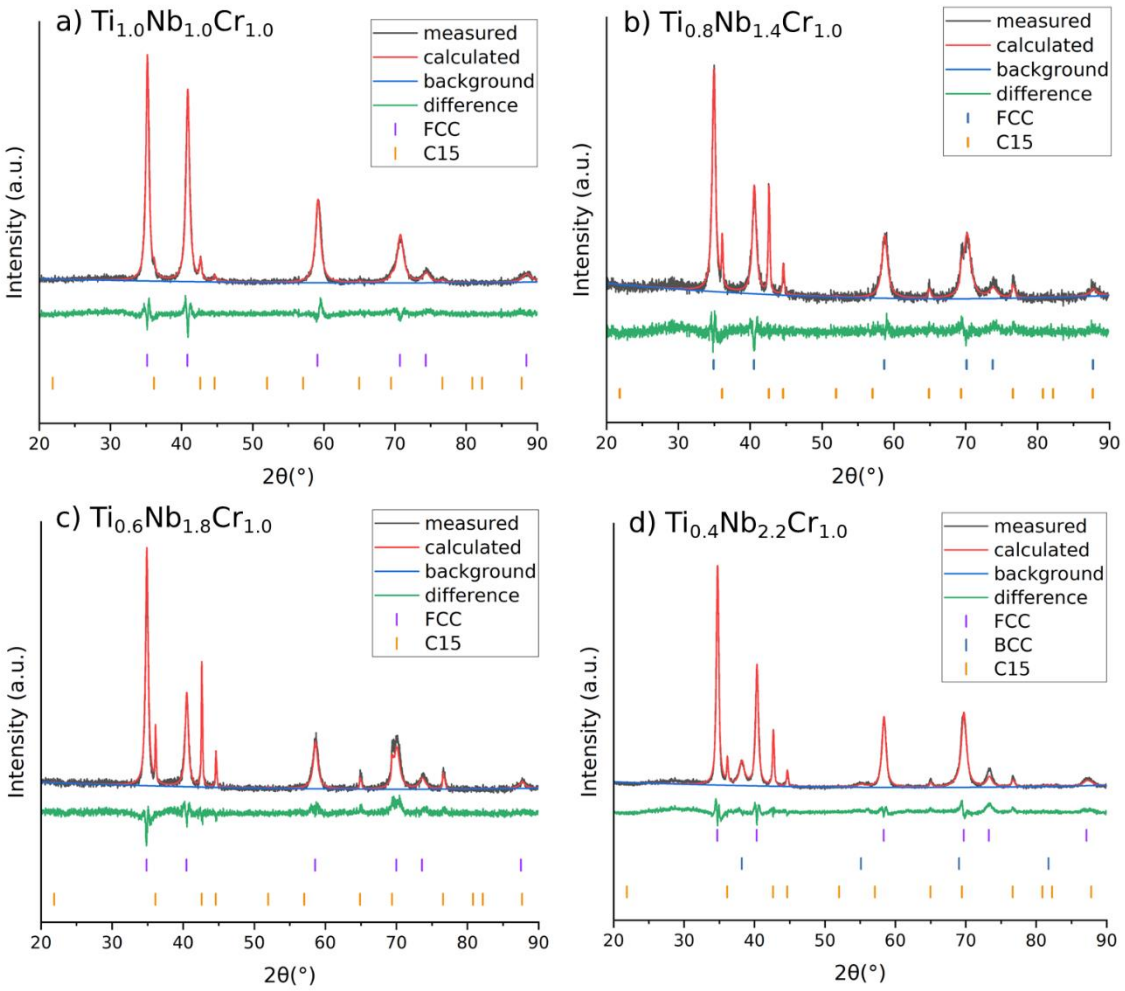

Figure A2: Rietveld refinements of the XRD patterns from the hydrogenated a) $Ti_{1.0}Nb_{1.0}Cr_{1.0}$, b) $Ti_{0.8}Nb_{1.4}Cr_{1.0}$, c) $Ti_{0.6}Nb_{1.8}Cr_{1.0}$, and d) $Ti_{0.4}Nb_{2.2}Cr_{1.0}$ alloys. The FCC and BCC phases were modeled with the compositions measured by EDX and the C15 Laves phase was modeled with a (Ti, Nb)Cr_2 composition.

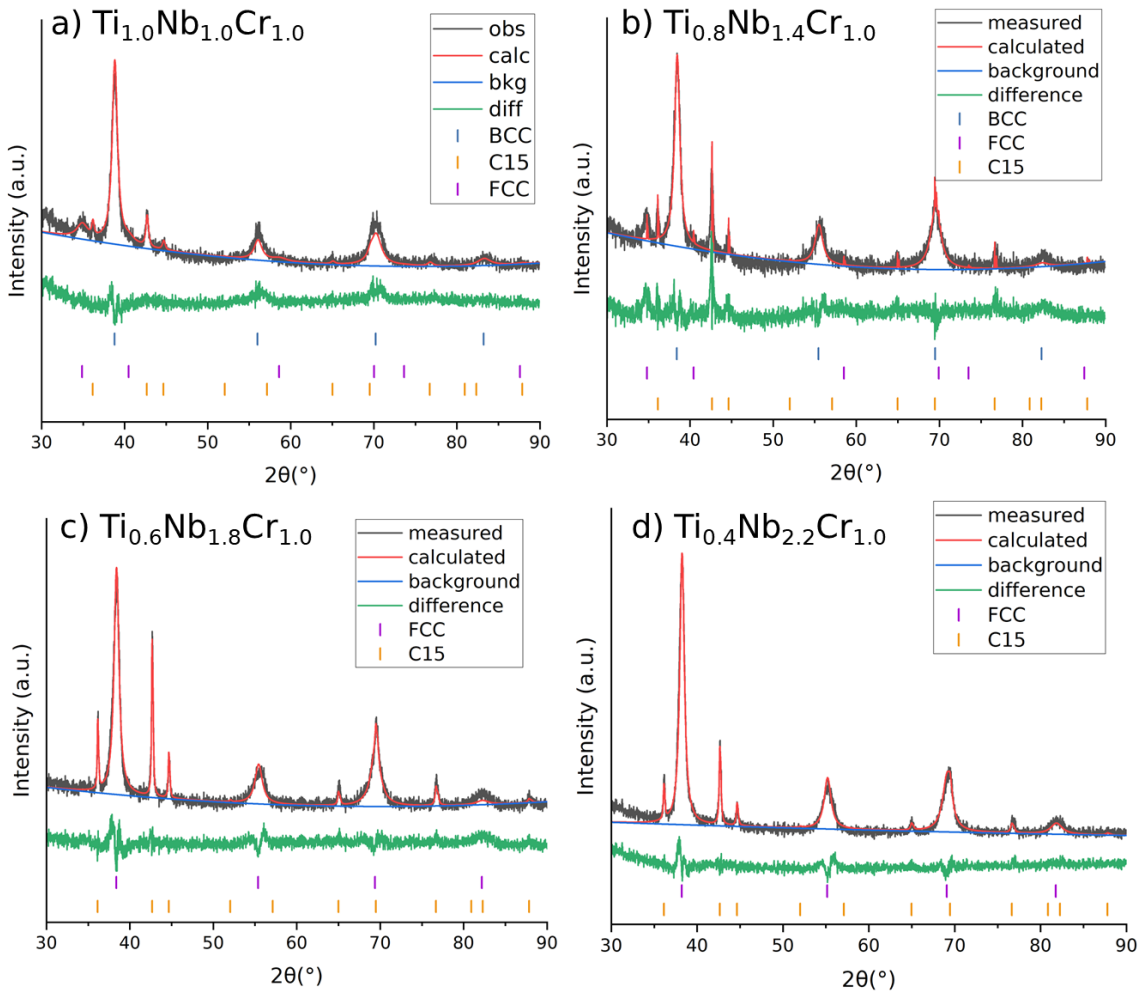

Figure A3: Rietveld refinements of the XRD patterns from the partially hydrogenated a) $Ti_{1.0}Nb_{1.0}Cr_{1.0}$, b) $Ti_{0.8}Nb_{1.4}Cr_{1.0}$, c) $Ti_{0.6}Nb_{1.8}Cr_{1.0}$, and d) $Ti_{0.4}Nb_{2.2}Cr_{1.0}$ alloys. The FCC and BCC phases were modeled with the compositions measured by EDX and the C15 Laves phase was modeled with a (Ti, Nb)Cr_2 composition.

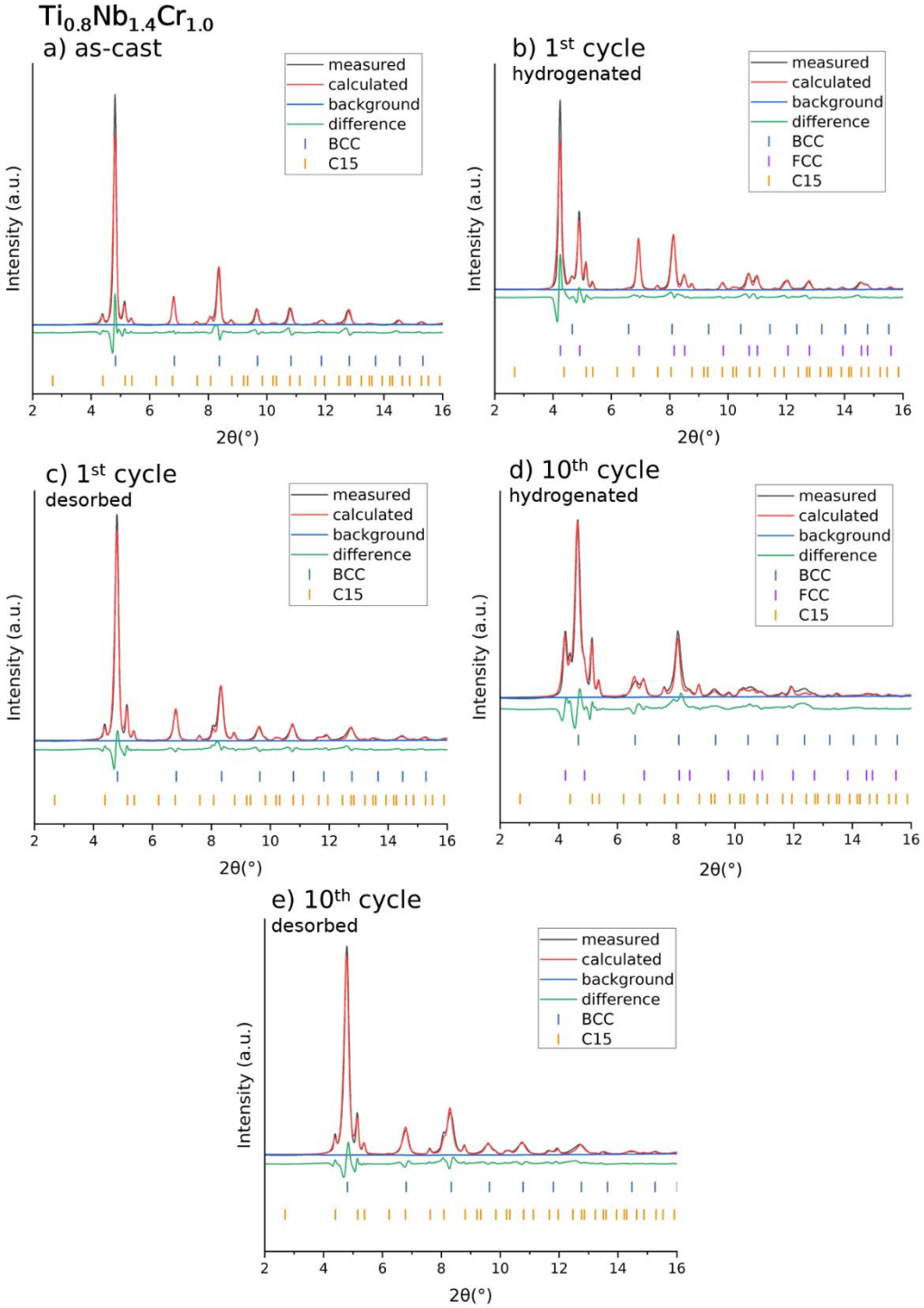

Figure A4: Rietveld refinements of the XRD patterns from the $Ti_{0.8}Nb_{1.4}Cr_{1.0}$ alloy a) as-cast, b) hydrogenated (1st cycle), c) desorbed (1st cycle), d) hydrogenated (12th cycle), and e) desorbed (12th cycle). The FCC and BCC phases were modeled with the compositions measured by EDX and the C15 Laves phase was modeled with a (Ti, Nb)Cr_2 composition.

APPENDIX B

EDX elemental maps

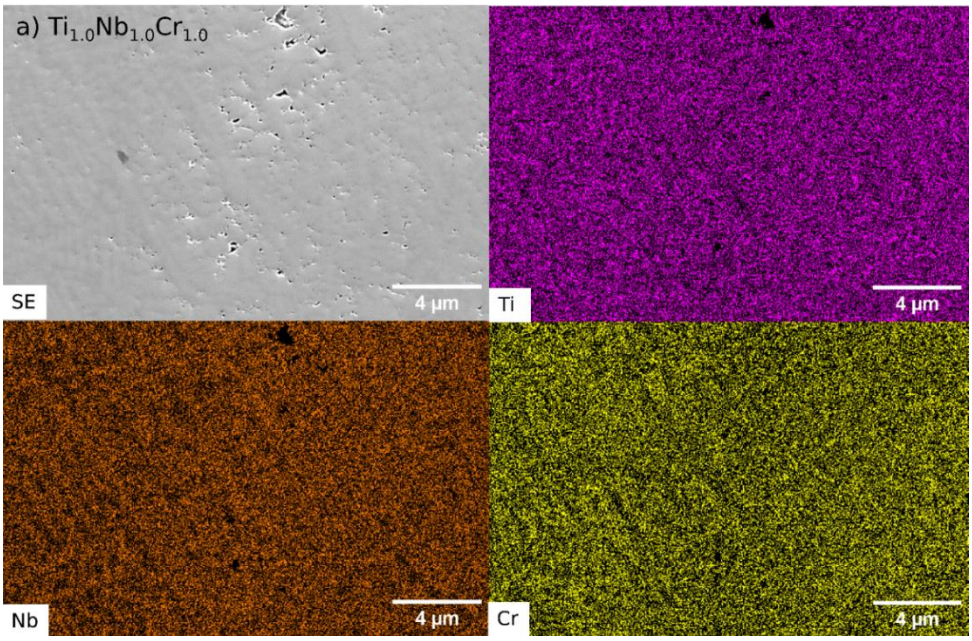

Figure B1: Secondary electrons (SE) image and corresponding EDX elemental maps of the as-cast $Ti_{1.0}Nb_{1.0}Cr_{1.0}$.

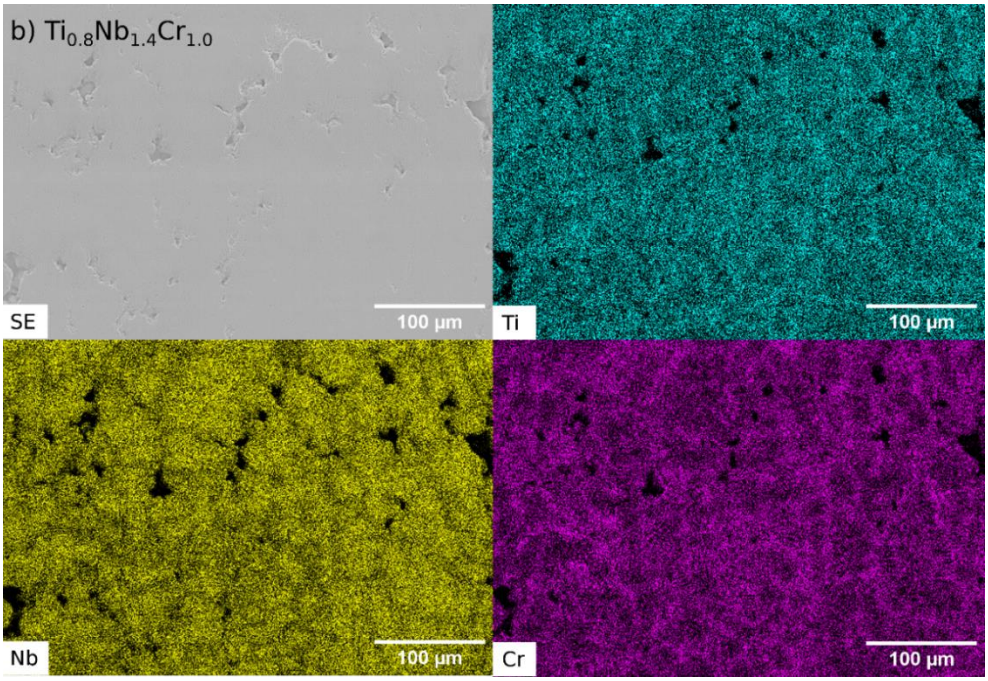

Figure B2: Secondary electrons (SE) image and corresponding EDX elemental maps of the as-cast $Ti_{0.8}Nb_{1.4}Cr_{1.0}$.

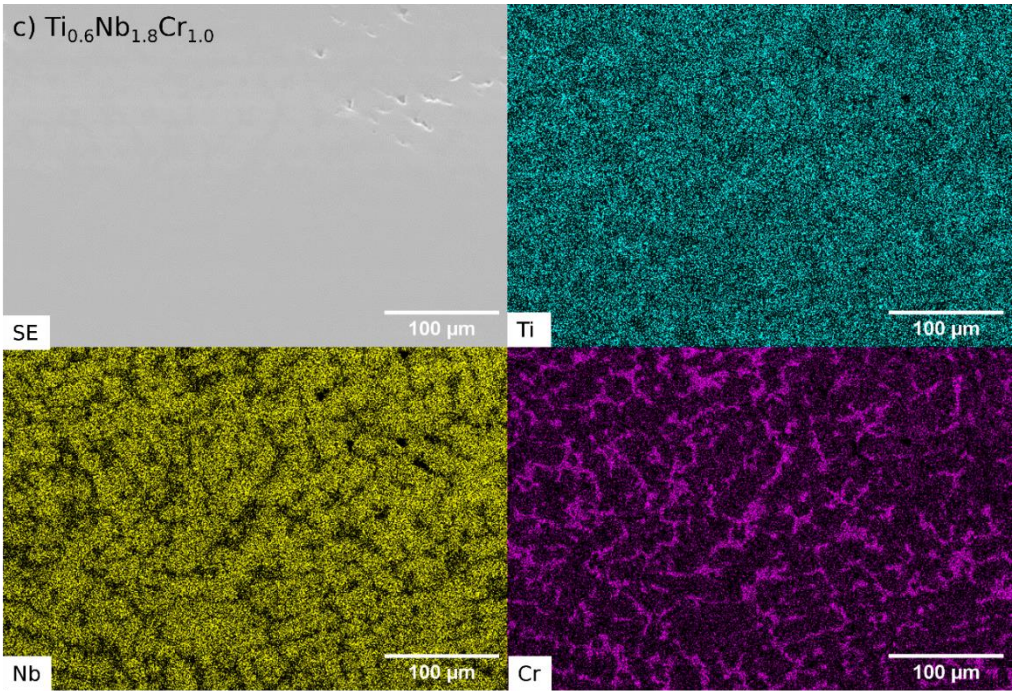

Figure B3: Secondary electrons (SE) image and corresponding EDX elemental maps of the as-cast $Ti_{0.6}Nb_{1.8}Cr_{1.0}$.